9-18-2023

Equilibrium and Active Self-Assembly and Collective Properties of Network-based Biomaterials

Lauren Melcher
lem3067@rit.edu

Recommended Citation

Melcher, Lauren, "Equilibrium and Active Self-Assembly and Collective Properties of Network-based Biomaterials" (2023). Thesis. Rochester Institute of Technology. Accessed from

Equilibrium and Active Self-Assembly and Collective Properties of Network-based Biomaterials

by

LAUREN MELCHER

A Dissertation Submitted in Partial Fulfillment of the Requirements
for the Degree of Doctor of Philosophy in Mathematical Modeling

School of Mathematical Sciences
College of Science

Rochester Institute of Technology
Rochester, NY

September 18, 2023

Abstract

Biological systems have the unique ability to self-organize, respond to environmental stimuli, and generate autonomous motion and work. The fields of biomaterials and synthetic biology seek to recapitulate these remarkable properties of biological systems in in-vitro reconstitutions of biological systems, and in abiotic or biotic-abiotic hybrid materials to better understand the underlying rules of life and to predict the design principles of biomimetic smart materials. Motivated by this, we create bottom-up mathematical models, rooted in experiments, of network-based synthetic and biological materials. These encompass two-dimensional colloidal networks connected by rhythmic crosslinkers, and three-dimensional biopolymer networks assembled via depletion interactions, physical crosslinking, and adhesive proteins. We use Langevin Dynamics simulations to investigate the spatiotemporal evolution of these systems, probing and characterizing their emergent collective dynamics and structural properties. We refine our models by comparing our results with experimental data when available and make predictions of mechanisms driving the observed collective behavior and possibilities for modulation. By providing insights on what kinds of behavior to expect in different areas of the phase space, we use results from our model studies to help inform the rational design of bio-inspired soft materials with desired properties.

Certificate of Approval

Ph.D Degree Dissertation

The Ph.D. Degree Dissertation of Lauren Melcher has been examined and approved by the Dissertation committee as satisfactory for the dissertation requirement for the Ph.D. degree in Mathematical Modeling

Dr. Moumita Das, Ph.D.
Dissertation Advisor, Committee Member

Dr. Poornima Padmanabhan, Ph.D.
Committee Member

Dr. Niels Otani, Ph.D.
Committee Member

Dr. Rae Robertson-Anderson, Ph.D.
Committee Member

Dr. Patricia Taboada-Serrano, Ph.D.
Dissertation Chair, Committee Member

Dr. Nathan Cahill, Ph.D.

Program Director

Acknowledgements

First, I want to thank Dr. Moumita Das, my PhD advisor, for her taking me on as a mentee, for her support and guidance, and for pushing me to develop as a scientist. I want to acknowledge the Das group members for their help and support—especially postdocs Mike Norton who helped mentor me on the chromatin project and Jonathan, who has been my research buddy on the cytoskeletal composite project. I especially want to thank Jonathan for his patience and help in the office this summer as I was writing this dissertation.

I'm grateful to my dissertation committee members, Poornima Padmanabhan, Rae Robertson-Anderson, Niels Otani, and Patricia Taboada-Serrano for their contributions, presence, and insightful feedback on my research. I want to thank my collaborators for their support and input. It has been an amazing experience getting to be a part of so many different projects. I want to thank Dr. David Ross from the RIT Math Department for always pushing me and for giving me guidance on my career.

Finally, I want to express my gratitude to my family for their encouragement and support. Especially, my mom for letting me vent to her endlessly about debugging my code and my dad for helping me move to Rochester. I want to recognize my cat, Aqua, who's been with me since 2019. She's has been the best companion a grad student could ask for and has given me the stability that I needed to get me through my qualifiers, my proposal and now dissertation defense. I want to thank my friend Kate Kiefer, one of the best friends that I've made in Rochester. She has cat-sat Aqua for so many of the week-long conferences and workshops I've had to travel for. Knowing that Aqua has always been well-cared for when I was out of town helped me keep a clear mind and kept me productive during my trips. I also want to thank all of my friends for their support and for cheering me on. They have made my time here wonderful, and I'm incredibly grateful for that.

Introduction

Biological systems have the unique ability to self-organize, respond to environmental stimuli, and generate autonomous motion and work. The fields of biomaterials and synthetic biology seek to recapitulate these remarkable properties of biological systems in in-vitro reconstitutions of biological systems, and in abiotic or biotic-abiotic hybrid materials to better understand the underlying rules of life and to predict the design principles of biomimetic smart materials. Motivated by this we construct and investigate a series of model systems of network-based soft synthetic and biological materials, with focus on their emergent collective structural and dynamic properties and how these properties can be tuned. A commonality among all the different systems is that they undergo self-assembly and phase transitions to non-equilibrium and equilibrium states. Combinations of active and passive components like protein crosslinkers, crowding depletants, and molecular motors help tune these mechanical and structural properties.

We first investigate a 2D in silico model colloidal system closely aligned with a collaboratively studied experimental system of colloids and bacterial proteins KaiABC that maintain circadian rhythms (oscillations) and can be engineered to crosslink the colloidal particles. We use Langevin dynamics to investigate the time-dependent changes in structure and collective properties of this system by tuning the valency of crosslinker binding and crosslinking kinetics. Our simulations show that when the crosslinker attachment and detachment probabilities are entrained to their circadian cycles, the valency of crosslinking between a pair of colloidal particles determines whether we achieve a rapid self-assembly of a colloidal network robustly connected to the circadian timescale, or a disordered colloidal system.

Next, we explore an in silico model where we decouple the detachment probability of the crosslinkers from their oscillation periods, and instead prescribe crosslinker lifetimes that are coupled to the period. As before, we use Langevin dynamics to examine the time-dependent changes in structure and collective properties of this system as a function of colloidal packing fractions and crosslinker oscillation periods and characterize the degree of order in the system by using network connectivity, bond length distributions, and collective motion. Our simulations suggest the conditions for producing distinct states of this colloidal system with pronounced differences in the degree of microstructural order and residence times. In particular, even for very dilute systems, we obtain sustained transitions between states of distinct degree of structural order by just varying the crosslinker oscillation period.

The next chapter in this thesis focuses on the organization of biopolymers in crowded environments into networks and compact assemblies. We study two model systems, one focused on biopolymers found in eukaryotic systems and one on biopolymers in prokaryotic systems. While direct physical crosslinking mechanisms can induce or manipulate self-assembly of biopolymers, they are not the only mechanisms that can achieve this. For example, when actin filaments, the biopolymers from the network-like scaffold (cytoskeleton) mainly responsible for eukaryotic cells' mechanical properties, are immersed in a solution of crowding agents such as polyethylene glycol (PEG), they can undergo transitions from an unconnected system to an entangled network of filaments or filament bundles due to depletion forces which cause the actin filaments to effectively be closer. To understand this behavior, we construct and investigate a 3D model of actin filaments modeled as chains made of connected beads, and PEG modeled as colloidal spheres, and explore how tuning the molecular weight and concentration of the depletant PEG leads to the emergence of different phases of networks of actin filaments or their bundles. We further show that when the total mass or total number density of the PEG is held fixed, the strength of the depletion interactions increases and this is reflected in the degree of bundling in our simulations. Our results align with our analytical scaling predictions in limiting cases, as well as with observations from experimental studies by our collaborators that the increase in molecular weight of PEG yields bundling of actin filaments. Next we study self-organization in models of biopolymers (DNA) in prokaryotic systems, namely starved E. Coli bacteria, via proteins called DPS, short for DNA protecting protein under starved conditions. The DNA in these bacteria cells is not contained within a membrane-bound organelle but are compacted by DPS proteins, which shields the DNA from damage. Here the self-assembly and phase separation of DNA is primarily driven by the DPS protein binding. We construct a 3D model of the DNA chains immersed in a solution of DPS proteins to understand and predict how tuning strength of the heterotypic interactions and DPS concentration affects the condensate formation of DNA.

Finally, we turn to self-assembly and collective properties of composite biopolymer systems in equilibrium, as well as driven out of equilibrium by molecular motors. Cytoskeletal networks are the motivation for our final study. The cytoskeleton plays a key role in cellular force generation, shape change, and movement. Characterizing the physics of this dynamic structure is challenging. More specifically, the interactions between the two main biopolymers that constitute the cytoskeleton, actin and microtubules, and the associated molecular motors myosin and kinesin, have been recently recognized as critical to cytoskeletal functions but the mechanisms of their interactions are not easily understood. With the 3D bead-chain model now extended to a model of actin and microtubules without and with motors, we study the actin-microtubule interplay and how various motor proteins and crosslinkers impact the spatial organization of these networks in and out of equilibrium. An area of interest in our theory-experiment collaboration on this project lies in developing a set of high-throughput in-house software to analyze metrics like mechanical stiffness and contractility, and propagation of mechanical stresses in experimental and simulated data. To address this, we take a toy-model approach where we implement nucleation sites to generate global and local contractions (asters) in separate actin and microtubule channels. Overall, our studies lay the foundation to study the emergent collective equilibrium and active mechanics arising in cytoskeletal composites in cells.

Contents

Chapter 1

Time-Dependent Colloidal Self-Assembly Controlled By Circadian Proteins

1.1 Background

Living organisms have active components that allow for generation of coherent motion and self-organized dynamics.[1] They are robust to time-varying environments [2] and often undergo dynamic changes in properties based on internal time-keeping machinery such as the cell cycle and the circadian clock [3]. Recent studies have also suggested the existence of "autonomous clocks" which can run independently to support living systems' functions [4]. A mechanistic understanding of such biological systems can advance the engineering of new smart materials that can self-organize, self-stimulate, and evolve independently according to the application environment. In the past decade, studies of active soft materials have sought to understand the layers of complexities and mechanistic structures in biological systems.[5–9] However, the rational design of active synthetic materials that can recapitulate the autonomous, persistent, and reversible dynamics of living materials without external intervention remains a challenge. We discover new insights on this research field by using bacterial circadian clock proteins KaiA, KaiB, and KaiC, to facilitate time-dependent self-assembly and dissolution of colloids, via crosslinking.

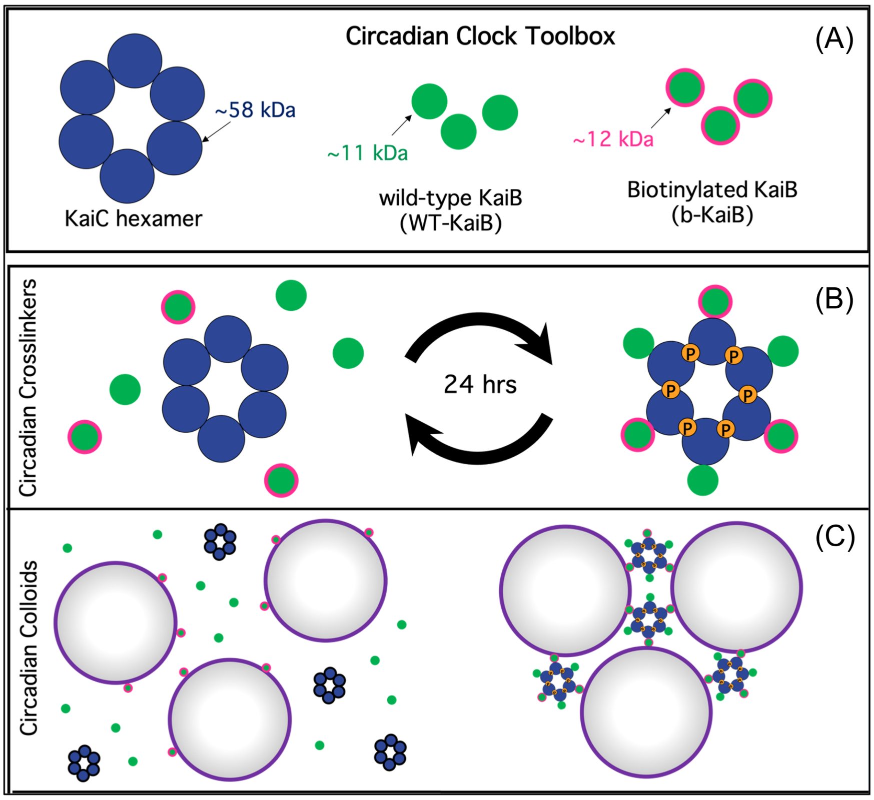

Figure 1.1: Schematic of circadian proteins KaiABC. These rhythmic proteins are engineered to serve as oscillatory crosslinkers for synthetic materials. (A), The blue hexamer represents KaiC, the green particles are KaiB proteins, and KaiA is not pictured. (B), Over a period of 24 hours, The Kai proteins are able to transition from being free and dissociated to forming a complex, based on the phosphorylation state of KaiC. (C), To utilize these proteins as crosslinkers, we biotinylate some of the KaiB proteins, which is visualized in magenta outlines in (A). The biotinylation allows the KaiB to serve as sticky connections that can attach to the colloids.

KaiA, KaiB, and KaiC are three proteins that make up the circadian oscillator in the cyanobacterium *Synechococcus elongatus* [10]. These set of bacterial proteins help regulate the circadian rhythms in cyanobacteria [10, 11]. KaiA binds to KaiC, which promotes phosphorylation of KaiC. Once there is a sufficient amount of phosphorylation, KaiB are then able to bind to KaiC, forming that complex structure in Figure 1.1(B). The complex formation of KaiB and KaiC then inactivates the KaiA protein.This inactivation means that KaiA no longer promotes phosphorylation of KaiC, and the dephosphorylation of KaiC causes the KaiB to unbind from the hexamer. These proteins have a robust 24-hr phosphorylation rhythm as it has been shown that these proteins can be removed from their original cyanobacteria medium and still retain their circadian cycle in in-vitro [11, 12].

To get the KaiABC complexes to crosslink with the colloids or other synthetic materials, a certain number of the KaiB connections have to be mutated. The experimentalists achieve this by biotinylating or coating some the KaiB with biotin so that they can attach to the streptavidin-coated colloids [11]. The KaiB proteins are not naturally biotinylated, and we track the oscillatory dynamics of the mutated proteins as they form complexes and then dissociate back to free protein molecules. Figure 1.2 shows the fluorescence polarization for the KaiBC complexes. High levels of polarization correspond to a large amount of protein complexes that crosslink colloids. Low levels of polarization indicate the majority of the complexes dissociate and cannot crosslink colloids.

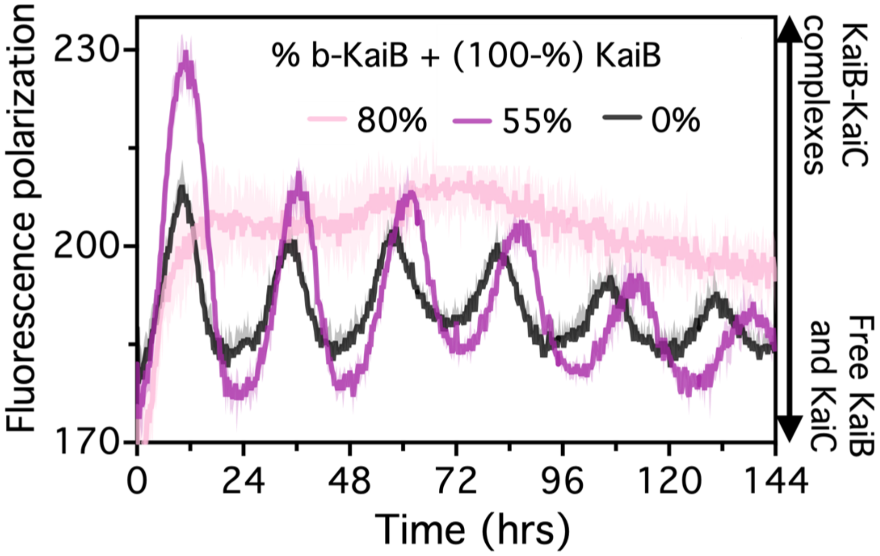

Figure 1.2: Fluorescence polarization of KaiABC complex formation characterizes the oscillatory behavior of proteins with 3 percentages of biotinylated KaiB.

We explore 3 different experimental cases: one where 80% of the KaiB's were biotinylated in that sticky coating, 55% were biotinylated, and a case where none of the KaiB's were biotinylated. From the pink curve here, we see that when they coat 80% of the proteins in biotin, there is an absence of any cyclic pattern and the proteins remain in the complex state. If 55% of the KaiB connections are sticky then we get these distinct oscillations with large amplitude within the first 24 hours in the purple curve. If there is no biotinylated KaiB (the 0% case/control), we still get this oscillatory pattern, but polarization levels are much lower with a decrease in amplitude. Furthermore the complexes cannot attach to the colloids since the KaiB proteins are not biotinylated.

1.2 Model and Method

1.2.1 Mathematical Model

Using Brownian Dynamics and C++ programming, we develop a 2D model of a colloidal system that corresponds to the experimental cases. Our system has 500 colloid particles that have a diameter $\sigma = 1\mu$m. The simulation box is 50μm by 50μm and periodic boundary conditions are applied. The packing fraction of the colloids is set to 16% to match the bead density in the imaging plane estimated from the binarized experimental images at $t = 0$. At the beginning of each simulation, all the colloids are separate, unlinked particles undergoing Brownian diffusion in 2D. When the surfaces of two colloids are within a distance $l = 10$nm of each other, they have a non-zero probability of linking together. If a pair of particles gets too close, they experience hard sphere repulsion. We simulate three cases that correspond to the experimental studies:

(1) Permanent crosslinking, where, once formed, bonds between colloidal particles are permanent.

(2) No crosslinking, where bonds never form between colloidal particles regardless of their proximity.

(3) Oscillatory crosslinking, where bond formation and dissolution follow the oscillatory activation and deactivation of the KaiBC complex.

For the cases (1) and (3), when a pair of particles are within a center-to-center distance of $r_0 = 1.01$, they can become crosslinked with a certain probability. This probability of attachment at simulation time t is $p_a = p_0 \cos^2(\pi t/T)$, where T represents the crosslinker oscillation period, and is set to 24 hours commensurate with the 24-hr rhythm of the Kai clock. The probability amplitude p_0 is a phenomenological parameter and we determine its value from the fluorescence polarization data for pS KaiC. We fit an exponential function $y(t) = y_{ss} + (y_0 - y_{ss})e^{-t/\tau_F}$ to this data, where y_0 and y_{ss} denote the fluorescence polarization value at the onset of the experiment and at the time when the system has reached a steady state, respectively (see Figure 1.3). We measure $\tau_F \approx 4 \times 10^4$s from this fit, which we obtain the corresponding probability $p_0 \approx 1 - e^{-\tau/\tau_F} \approx \tau/\tau_F$. Here, $\tau = 2.5$s is the timescale used to non-dimensionalize the simulation and is set to the time for a colloid to diffuse across its own diameter in water. In cases where the particles can rhythmically unlink, we implement a detachment probability, $p_d = p_0^n \sin^2(\pi t/T)$, where n is the number of bonds (KaiABC crosslinkers) connecting the particle pair under

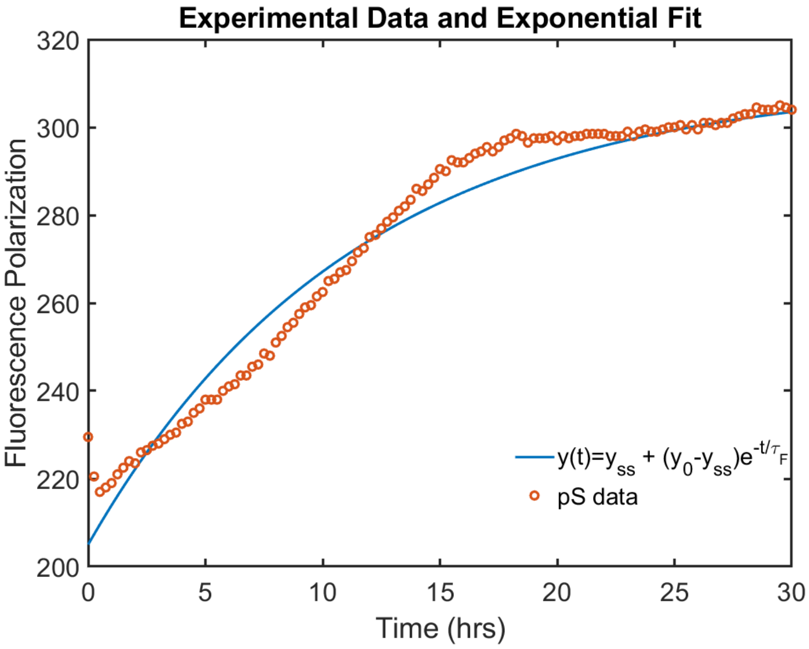

Figure 1.3: The plotted fluorescence polarization data for the experimental pS case, which corresponds to 80% of the KaiB proteins being biotinylated. An exponential function has been plotted alongside the pS data to determine an appropriate probability coefficient and timescale.

consideration. At the beginning of each simulation, the system has a maximum probability of attachment and a minimum probability of detachment to simulate the KaiABC reaction beginning in a phase corresponding to the KaiB-KaiC complex formation.

The translational motion of the i^{th} colloidal particle is governed by the overdamped Langevin equation:

$$\frac{d\mathbf{r_i}}{dt} = \frac{D}{K_b T}\sum_j (\mathbf{F}_{LJ,ij} + \mathbf{F}_{c,ij}) + \sqrt{2D}\eta, \tag{1.1}$$

where k_B is the Boltzmann constant, temperature T is set to room temperature, D is the colloid diffusion coefficient, and η represents Gaussian noise with a mean of zero and a unit variance. The interparticle interaction force consists of two contributions. The first contribution comes from the hard-sphere interaction between particles, modeled by the repulsive part of the 12-6 Lennard-Jones potential,

$$V_{LJ} = 4\epsilon\left[\left(\frac{\sigma}{r_{ij}}\right)^{12} - \left(\frac{\sigma}{r_{ij}}\right)^{6}\right], \tag{1.2}$$

where ϵ is the interaction strength. We non-dimensionalize equations by scaling distances by the particle diameter σ, times be the diffusion timescale $\tau = \sigma^2/D$, and energies by $k_B T$. We run the simulations for 69120τ, corresponding to 48 hrs of experimental time, and show averages over 5 runs in the results presented in this chapter.

1.2.2 Simulation Parameters

Simulation parameters and their values used in the model and simulations. Numerical estimates of all parameters are based on experimental values as described in the Source column.

Simulation Parameters	Value	Source
2D colloid packing fraction	16%	Area fraction of pixels above threshold in binarized images of pT colloids
Simulation unit lengthscale, σ	1 μm	Colloid particle diameter
Simulation unit timescale, τ	2.5 s	Time for colloid to diffuse its own diameter in water, $\tau = \sigma^2/D$
Crosslinker oscillation period, T	34560τ	~24hrs, set to match KaiABC period
Brownian dynamics timestep, dt	0.001τ	Ensures numerical stability
Characteristic timescale of KaiB-KaiC interaction, τ_F	4 x 10^4 s	Obtained by fitting experimental FP data for pS to an exponential
Probability of colloid crosslinking, p_0	$6e^{-5}$	$p_0 \approx 1 - e^{-\tau/\tau_F} \approx \tau/\tau_F$
Equilibrium distance between centers of crosslinked colloids, r_0	1.01σ	Sum of colloid diameter and ~10 nm size of KaiBC complex
Spring constant of crosslinks, K	$9k_BT/\sigma$	Phenomenological estimate

1.2.3 Measured Quantities

Spatial Image Autocorrelation

We perform the same SIA algorithms used to analyze experimental images on system configuration images from simulations generated using MATLAB at time points corresponding to experimental time points 1, 7, 14, 21, and 28 hrs. Prior to SIA analysis, the images are converted to binary images with colloids being filled with dark gray circles and the empty space being white, similar to experimental binarized images. To determine the average $g(r)$ and ξ for each time point, we analyze images for 5 consecutive time points centered on the time of interest, consistent with experiments. The $g(r)$ and ξ values shown are averages of the values determined from the 5 different images with error bars representing standard error.

Colloid Connectivity Number

We measure the Colloid Connectivity Number (CCN) as a way of determining how connected our colloidal system was over time. This was done by counting the number of connections each colloid had and then finding the sum of the number of connections. That sum is then averaged by the system size.

1.3 Results and Discussion

To qualitatively characterize the crosslinking kinetics of the KaiABC complex that produce the colloidal clustor formation, microscopic images of the systems are sampled at 9 different timepoints over the course of 28 hours. Then, the stack of images are overlayed temporally, with a colorscale indicating change in time as each color goes from dark to light, as seen in Figure 1.4. In Figure 1.4(C), colloid sedimentation and clustering is evident in the pS-system, with an emergent structure appearing with the lighter colors shown in Figure 1.4(A), which is emphasized in the zoomed-in inset on the upper right of the color-coded image. By comparison, the experimental pT case has little to no cluster formation in the system in Figure 1.4(B). The zoomed-in insets further demonstrate the lack of colloid clustering and connectivity for the KaiC complex with no biotinylated KaiB.

Next, we produce colorized temporal projections of simulation snapshots for colloids with permanent crosslinking in Figure 1.4)(C), which align the experimental pS-system and colloids with no crosslinking (shown in Figure 1.4)(D)), which relates to the experimental pT control case. There are qualitative similarities between each corresponding set of colorized images. The time frames of the simulations used in the projections are the same as the ones in experiments, with colorscales showing change in time from dark to

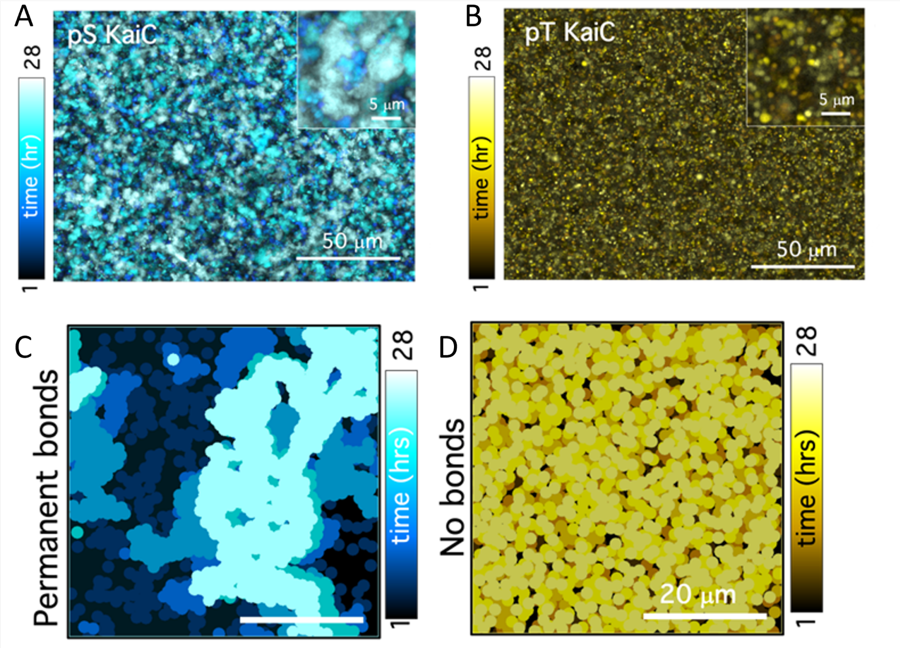

Figure 1.4: Colorized temporal projections of time-lapsed snapshots for the experiments and simulations. These snapshots were captured over a period of 28 hours, with corresponding colorscales showing change in time from dark to light. (A), The temporal overlay for the experimental pS case, where 80% of the KaiB are biotinylated. (B), Temporal projections of the pT experiments, the control case where no KaiB were biotinylated. (C), Temporal projections from the simulation case that corresponds to the experimental pS-colloidal system. (D), Temporal overlays of the simulation snapshots for a system with no crosslinking, which relates to the pT experimental system.

light. When comparing the temporal overlays of the simulation images vs their respective experimental overlays, we observe qualitative similarities between each set. The set of projections for the control case with no crosslinking in Figure 1.4(B,D), in both the simulations and experiment images, the colloids remain in a disordered state and there's minimal clustering occurring over the 28 hr period. For the permanent bonds case, we see an emergent structure forming over time in simulation temporal overlays, which matches what is seen in the corresponding pS-experimental projections.

The colloid clusters in Figure 1.4(C) from the model system are larger than the experimentally observed clusters. This is expected because the model colloidal network can only grow in the 2D plane since the model is in 2D. The experiments are in 3D and based on the pixel intensities and z-stacks the experimentalists looked at, the experimental clusters likely extend perpendicular to the 2D plane [11].

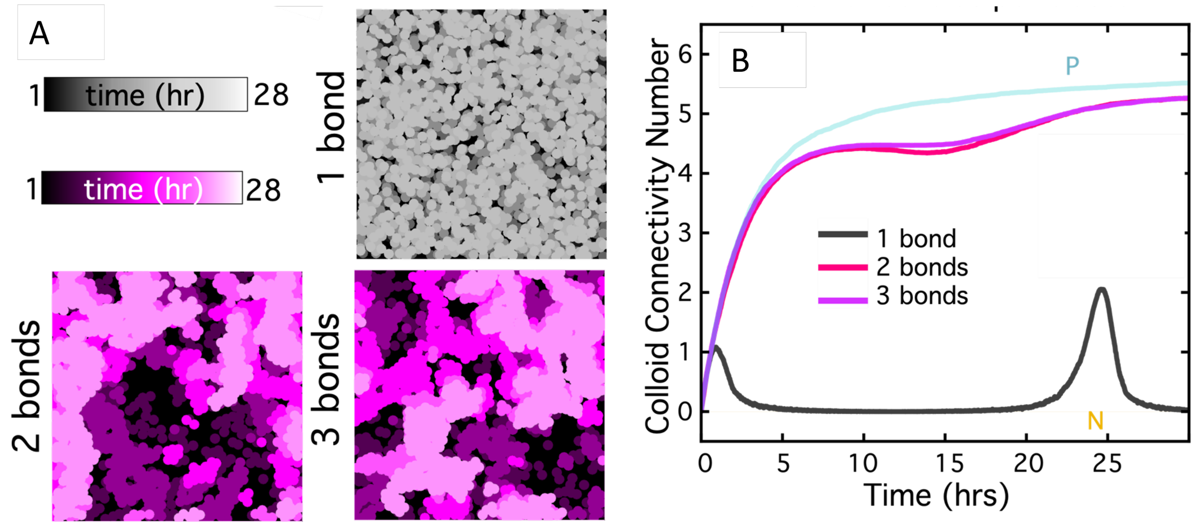

Figure 1.5: Simulated results that correspond to the experimental systems. (A), Colorized temporal projections of simulation configurations that represent the monovalent case and the 2- and 3- bond valency case with oscillatory crosslinking dynamics. (B), Colloid Connectivity Number (CCN) for all 3 valency cases plotted over time.

Next, we analyze the simulation case with cyclic crosslinking kinetics. In Figure 1.5(A), are the temporal overlay images of the colloid time-lapses for 3 subsets of simulations. The top image colored in gray, is a monovalent case where a colloid connection is equivalent to a single crosslink or protein complex. From this temporal projection in 1.5(A), we observe little to no cluster formation in the system. When measuring the CCN over time, we observe oscillatory behavior in the connectivity curve, with peaks occurring at time points that correspond to the peaks in the phosphorylation of KaiC, when the probability of attachment is at its highest. The heights of the peaks are at a CCN value of 1 and then 2 and these values are low, emphasizing that there's minimal clustering and a lack of a network formation in the colloid system present; this agrees with the qualitative observation from the temporal overlay.

In the experiments, there is a high concentration of KaiABC proteins and the size of the complexes are 2 orders of magnitude smaller than the surface area of a colloid [11]. Thus, it is highly likely that multiple KaiABC protein complexes constitute a single connection between 2 colloids. To incorporate this into our model, we explore cases where colloid connections consist of either 2 or 3 crosslinkers/complexes. When we measure the CCN for the 2- and 3-bond valency cases, the CCN increases sharply at at the beginning, which is similar to the permanent bond case (represented by the cyan curve in Figure 1.5(B)). The CCN does not experience a significant decrease during the dissembly phase, when KaiABC proteins start to dissociate and the probability of detachment is higher. Instead, only a small number of connections are lost during this phase and the system still maintains a well-connected structure and approaches saturating connectivity levels during the second phosphorylation period. The multi-valent cases of 2- and 3-bond are qualitatively comparable while the monovalent case indicates that dissolution of the colloidal network will not occur unless a majority of the crosslinker bonds detach.

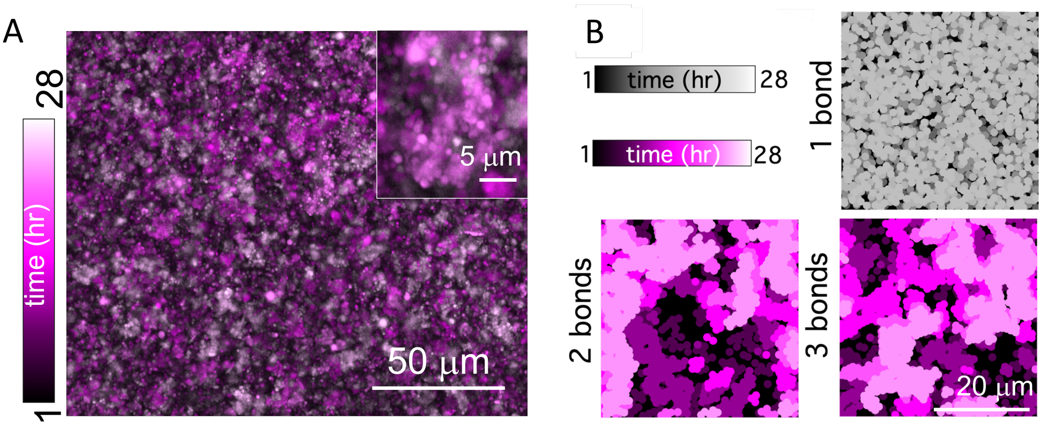

Figure 1.6: Simulations and experiments are in qualitative agreement for the 55% biotinylated KaiB system. (A), Colorized temporal overlay of colloid images over the course of a 28 hr period, showing that clusters are forming over time. (B), Colorized temporal overlays of simulation configurations for the monovalent case and the 2- and 3- bond valency case with oscillatory crosslinking dynamics.

When we compare the temporal overlays of the 2- or 3- bond valency cases against the corresponding 55% experimental KaiB case, we observe qualitative similarities between the simulations and experiments. Particularly in Figure 1.6(A), the zoomed-in inset for the experimental system shows an emergent structure forming over time as indicated by the lighter colors, which corresponds to the colloid cluster formation in the 2- or 3- bond valency overlay images in Figure 1.6(B).

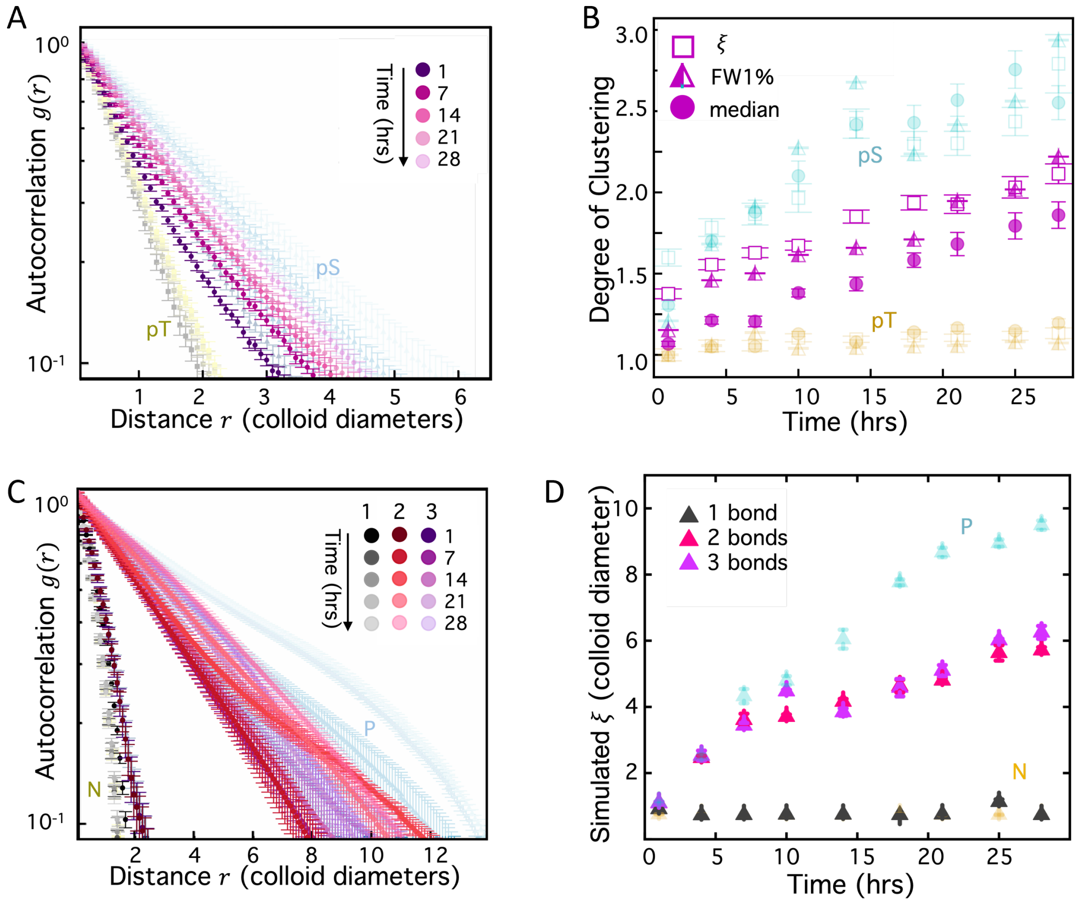

Figure 1.7: The time-course of colloid clustering is mediated by the KaiC phosphorylation state and the bonding valency of the KaiABC complex. (A), Spatial Image Autocorrelation $g(r)$ curves for the pS case (in light cyan), the 55% biotinylated KaiB experiment (in magenta shades), and the pT case (in grey/yellow). Five different times were sampled for the $g(r)$ curves within the 28 hour period. (B), The degree of relative clustering in the experiments was quantified by the correlation lengths (ξ, open squares), full width 1% (half-filled triangle), and the median cluster size (filled circle).

To further examine the structural properties of the systems, we utilize the spatial image autocorrelation (SIA), also known as $g(r)$. This metric is often used by the experimentalists on our team and provides clearer insight on the structural order or spatial arrangement of the colloids. The SIA measures the correlation between pixels in an image separated by a radial distance r, which we have set to be units of colloid diameters (1μm). We measure the SIA at a series of 5 different time-points in both experiments (Figure 1.7(A)) and simulations (Figure 1.7(C)) to understand the degree of spatial order of the colloids over time. From the $g(r)$ trajectories, we also extract a correlation length from each of the systems. The correlation length tells us the spread size of the colloids and this length is obtained by finding the point at where each $g(r)$ curve hits the x-axis in Figure 1.7(A) and (C)

The yellow/gray curves in Figure 1.7(A) correspond to the control/no bonds pT-experimental system and we see that the simulation cases with no bonds and monovalent bonds are qualitatively similar; both simulation cases and the pT-experimental case show no time-dependence or cluster formation as their $g(r)$ curves have a very fast decay rate. The correlation lengths for the pT-system and monovalent simulation case, in Figure 1.7(B) and (D), respectively, remain at values of 1-2r, which also indicates minimal cluster formation and that the systems remain in a disordered state over time.

For the permanent bonds case, in both the experiments and simulations, the $g(r)$ have the slowest rates of decay, which suggests a larger characteristic size of features in the images. In Figure 1.7(A), the pS-experimental autocorrelation curves hit the x-axis around 5r, which signifies a cluster size of 5 colloids. For the corresponding simulation curves (Figure 1.7(C)), the characteristic spread size of the colloids is closer to 12r. The characteristic correlation length from the simulations is comparatively larger than the corresponding pS-experimental correlation lengths. A reason for this difference is because the simulations are in 2D, which restricts the colloid clusters to grow only in the 2D plane. Because the images are only projections of the 2D plane for experiments, it is likely that the colloid structures in experiments are growing perpendicular to the 2D plane [11]. The correlation length trends in Figures 1.7(B) and (D) show that the cluster size of the colloids steadily grows over time which further suggests emergent structure formation occurring over time.

For the multivalent cases, the $g(r)$ lie in between the two extreme cases of no bonds and permanent bonds. The $g(r)$ curves show similar qualitative trends to the oscillatory, 55% biotinylated KaiB case. The autocorrelation curves show that the decay rate is faster than that for the permanent bonds case but are still significantly slower than the no bonds/monovalent cases. We examine the correlation lengths of the multivalent cases and the simulation trajectories of the increasing correlation length over time aligns with the degree of clustering observed in the experiments.

1.4 Conclusion

Engineering classes of smart active materials that can autonomously regulate their morphology and wield user-defined dynamic properties remains a challenge in soft active matter research. Our contribution to this research question was to engineer KaiABC circadian oscillators as functional crosslinkers and couple them to a system of colloid beads. We demonstrate that we can develop a material system that can undergo timed self-assembly and that the KaiABC oscillations are governed by the phosphorylation cycles of KaiC. Using modeling to inform the mechanisms, we find that the valency of the KaiABC crosslinkers tunes the structural properties of the system-sustained self-assembly can be achieved with multivalent bonds while monovalent bonds leads to a disordered colloidal system. Our work establishes the strategy of pairing biological clock proteins to synthetic materials like colloids and suggests that these proteins can be utilized in a variety of other materials like hydrogels, cytoskeletal composites, and granular materials [11]. From this, our foundational system platform can aid in the development of technologies like nanofiber sutures that dynamically respond to wound healing and soft robotics that can be applied in applications like camouflage, drug delivery, biomimetic electronics [11, 13–15].

1.5 Future Works

We are currently exploring other strategies to engineer a system that can undergo distinct phase transitions of network-like states, where colloids have high levels of connectivity, to disordered states, where things are less connected. From the experimental side, this involves exploring different crosslinker concentrations and different sizes of colloids. And with the simulations, we are able to test out different systems that align well with the new experiments. Next steps also include having two types of crosslinking valencies in the system: a fraction of the crosslinkers will have monovalent bond kinetics and the rest will have multivalent bonds to see if this will generate colloidal systems that can oscillate between the different states.

Chapter 2

Sustained Order-Disorder Transitions of a Colloidal Network Crosslinked via Rhythmic Crosslinkers

2.1 Background

Colloidal systems offer an attractive platform for constructing bottom-up minimal models that can offer insights into the rational design of such materials, given colloidal suspension and self-assembly have been studied extensively and are well understood[16, 17]. Most studies of colloidal systems, however, investigate phase separations and transitions caused by changes in colloidal density or by external actuation via changes in temperature, light, and pressure [18–22], and the role of crosslinker-driven phenomena is less well studied [23, 24]. Furthermore, although oscillatory dynamics have been studied in the context of polymerization in soft and biomaterials [25–27], most active material prototypes and models are unable to attain autonomous, reversible transitions between states at a level consistent with living systems. For example, while some experiments and models of colloids do incorporate polymer attachments, the exceedingly small lifetimes ($\sim$ milliseconds to seconds) of these polymeric attachments do not allow for enough time to form large, well-connected, crosslinked networks, that can completely dissolve into an unconnected, disordered state upon unlinking of the crosslinkers. As a result, these attachments do not induce reversible transitions between distinct ordered and disordered states [28, 29] which are a hallmark of living systems.

What are the principles underlying the rational design of a system that can repeatedly transition between states with distinct structural and material properties at reliable user-defined periods, without the need of external actuators? To obtain insights into this question, we construct and investigate a model system consisting of colloids that can be connected via crosslinkers with oscillatory dynamics such that they can autonomously cycle between states with distinct degree of order and material properties. The crosslinkers regulating these oscillatory dynamics in our computational model are inspired by the bacterial clock proteins, KaiABC. These circadian oscillator proteins are found in cyanobacteria *S. elongatus* and have demonstrated a steady, regular 24-hr rhythm in vitro.[30] Here, we demonstrate the potential for effectively harnessing such rhythms to drive transitions in material properties of model colloidal systems. Through our predictive mathematical modeling of persistent order-disorder transitions in such systems of colloids and rhythmic crosslinkers, we hope to inform experiments by predicting the time-evolving collective properties as a function of crosslinker oscillation periods and colloidal packing fractions. Our results will also provide insights into the mechanisms that lead to emergent properties in these systems.

2.2 Model and Method

2.2.1 Mathematical Model

We simulate a model two-dimensional system consisting of colloidal particles and crosslinkers with oscillatory kinetics. The main ingredients and assumptions are as follows:

(1) The colloidal particles interact with each other via Lennard Jones (LJ) interaction

potential V_{LJ} [31], given by

$$V_{LJ} = 4\epsilon \left[\left(\frac{\sigma}{r_{ij}} \right)^{12} - \left(\frac{\sigma}{r_{ij}} \right)^{6} \right], \tag{2.1}$$

where r_{ij} is the interparticle distance, which is the measured distance between the centers of the two particles, σ is the particle diameter, and ϵ is the depth of the potential well. To reduce the computational expense, for our model, the interparticle distance r_{ij} is cut off at $2^{\frac{1}{6}}\sigma$, which encodes the resulting force as a repulsive-only force.

(2) When two particles are within a center-to-center distance r_0 equal to the sum of the particle diameter and the length of the crosslinker when it is neither stretched nor compressed, they can become connected via this crosslinker with an attachment probability P_a. The probability is dependent on the fraction of free crosslinkers p_k available to connect the particles and the time-period T of the crosslinkers as $P_a = p_k p_0 \sin^2(\pi t/T)$, where p_0 is a phenomenological parameter corresponding to the initial crosslinker concentration. We assume the crosslinker is dilute on the particle surface; while there are multiple crosslinking attachment sites on each colloid, we limit the number of crosslinks between any two particles to one.

(3) Once two particles are crosslinked, they stay attached for a given lifetime, unless the bonds are stretched beyond a length of 3σ, leading to particles unlinking prematurely. For simplicity, we associate the timescale of oscillations to also govern the lifetime of the crosslinkers. This lifetime is drawn from a Gaussian Distribution with a mean of $T/2$ and a standard deviation of $T/8$, where T is the crosslinker oscillation period mentioned earlier. This ensures the particles remain attached for a significant amount of time and avoids too many particles simultaneously attaching or detaching.

(4) The particle motion follows the overdamped Langevin equation:

$$\frac{d\mathbf{r}}{dt} = \frac{D}{k_B T_R}(\mathbf{F}_{LJ} + \mathbf{F}_c) + \sqrt{2D}\eta, \tag{2.2}$$

where the interparticle interaction force consists of two components: a force $\mathbf{F}_{LJ}$ obtained from the Lennard Jones potential defined earlier, and an elastic force $\mathbf{F}_c$ due to the stretching or compression of the crosslinker connecting the particles which is modeled as a Hookean spring[32]. The latter is defined as $\mathbf{F}_c = -K(r_{ij} - r_0)$, where r_0 is the crosslinker rest length and K is the spring coefficient. The constants k_B and T_R represent the Boltzmann constant and room temperature, respectively. The diffusive motion of the particles is described by the third term $\sqrt{2D}\eta$, where D is the diffusion coefficient and η represents Gaussian noise with zero mean and unit variance.

We initialize the system with five hundred unlinked colloid particles randomly distributed in the simulation box. When two colloidal particles are crosslinked, the length of the bond connecting them is the sum of the radii of the colloids and the length of the biomimetic crosslinker between them; for colloids of radius 0.5μm, r_0 is approximately 1.01μm, assuming a crosslinker length of 10nm which is the size of typical proteins. We set the value of the spring constant of this bond to be 0.036pN/μm such that the forces arising from the LJ interactions and spring forces are of comparable magnitude. We solve equation 2.2 for the particle positions, using first-order Euler integration. Periodic boundary conditions are used to avoid the computational expense of a large number of particles or a large simulation box size.[33]. The ratio of the number of colloids to crosslinkers is set to $1:4$ to allow for a considerable amount of crosslinking of the colloids while also ensuring the system is not over-saturated with crosslinkers and can revert back to an unlinked, disordered state. The attachment probability P_a is calculated at every time step across all the particles within r_0 of each other, and the phenomenological parameter p_0 is set to 0.005 to yield clear transitions between crosslinked and unlinked states, as illustrated in

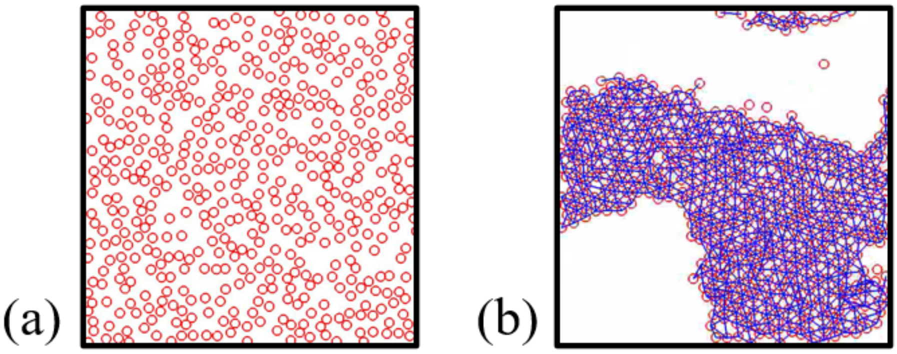

Figure 2.1: A model schematic of the colloidal system with a packing fraction of 30% and $T = 18000$. (a) The colloids are initially unlinked and diffusing in the simulation box. (b) When the system reaches an ordered state, the colloids are crosslinked via the oscillating crosslinkers

Fig. 2.1. The diffusion constant is set to $0.483\mu\text{m}^2/\text{s}$ to be within experimentally meaningful range. All of the lengths are scaled by the diameter of a colloid, which is $\sigma = 1\mu\text{m}$, all times by the time τ_D taken by a colloid to freely diffuse across its diameter, which is 2.07 seconds in our simulations, and energies by $K_B T_R \sim 4\text{pNnm}$, which is the energy associated with thermal fluctuations at room temperature. Coming to the period of oscillation T of the crosslinkers, while the duration of a 24-hr circadian rhythm of KaiABC oscillators is equivalent to $43200\tau_D$, biological oscillators in nature have a wide range of oscillation periods, including values much smaller than that of the KaiABC proteins [34]. To decrease the computational expense, we explore shorter crosslinker oscillation periods, ranging from T=18 to T=18000. The main variables and parameters in this model are presented in the following tables below and chosen to mimic a system of 1μm beads suspended in water with 2D area fractions of $10 - 30\%$.

2.2.2 Varied Quantities

The two parameters varied in our simulations are the crosslinker oscillation period, and the colloidal packing fraction i.e., the fraction of area occupied by the particles in the simulation box.

- Crosslinker oscillation period: We investigate a model system with a colloid packing fraction fixed at 30% and 4 crosslinker oscillation periods $T = 18$, 180, 1800, and 18000, which are equivalent to 0.01, 0.1, 1, and 10 hours, respectively. The colloid concentration is kept intentionally dilute to allow the crosslinker proteins to induce system-wide oscillations between ordered and disordered states; too high of a packing fraction would automatically lead to an ordered state being formed, regardless of crosslinker dynamics.

- Packing fraction of colloidal particles: We keep the crosslinker oscillation period fixed at 1800 while varying the colloid packing fraction from $10 - 30\%$.

2.2.3 Measured Quantities

To determine transitions between liquid-like, disordered states and gel-like, ordered states, we investigate and quantitatively characterize the degree of order of our model system by calculating the connectivity, the ensemble average squared displacement, the mean squared displacement, the radial distribution function, and the bond length distribution as described below.

- The connectivity is calculated by finding the number of neighbors each colloidal particle is crosslinked to and averaging over all the particles. This average is calculated at every time step and plotted over time. The connectivity informs us of how network-like or connected our colloidal system is throughout the simulation. The difference in the values of the connectivity at its largest and smallest provides a measure of the amplitude of oscillations in connectivity where the amplitude equals one-half of this difference. Large, pronounced amplitudes demonstrate that the system is transitioning between states with significantly different degree of order.
- The ensemble average squared displacement (EASD) measures the network movement as a function of time. The equation for the ensemble average squared displacement is $\left\langle \, [r(t_0 + t) - r(t_0)]^2 \, \right\rangle$ where r represents the particle position and t

represents the time-period of interest. In our model, t_0 is set to $t = 0$ to demonstrate how the system changes over real time, starting from the beginning of the simulation. At each time t, we sum the square of the displacements of each particle and then average over the total number of particles.

- The mean squared displacement (MSD) is a sliding average given by $\left\langle \, [r(t+\tau) - r(t)]^2 \, \right\rangle$ and describes the motion of particles over certain lag times. The particle position at time t is denoted by $r(t)$ and the lag time is given by τ. From this measurement, we measure particle motion over small and large time intervals. Note that there are two main differences between the MSD and the EASD. The first is that the MSD tells us about the nature of the mobility of the systems as a function of lag time, while the EASD tells us this as a function of time. So the change in mobility as a result of the order disorder transitions will be more clearly seen in the EASD than the MSD. The second difference is that the MSD is averaged over both particles and time-origins, while the EASD is only averaged over particles.
- The radial distribution function (RDF) describes the probability of finding a particle within a shell of width dr at a distance r_n from a reference particle n. It is obtained by calculating the distance between all particle pairs and binning them into a histogram. The histogram is normalized with respect to a system with no correlations between particle positions, i.e., where the particles do not interact with each other. From this metric, we gain a better understanding of how ordered our system is. Sharp regular peaks in the plotted results indicate a ordered, network-like state, while fewer, less distinct peaks mean the system is less-ordered.
- The distribution of the lengths of the bonds between particles in the ordered states provides insights into network and cluster properties. A sharply peaked distribution suggests a well-connected network with a high degree of order, while a broad distribution indicates the presence of smaller clusters.

We also examine the general particle positions and movement and generate system

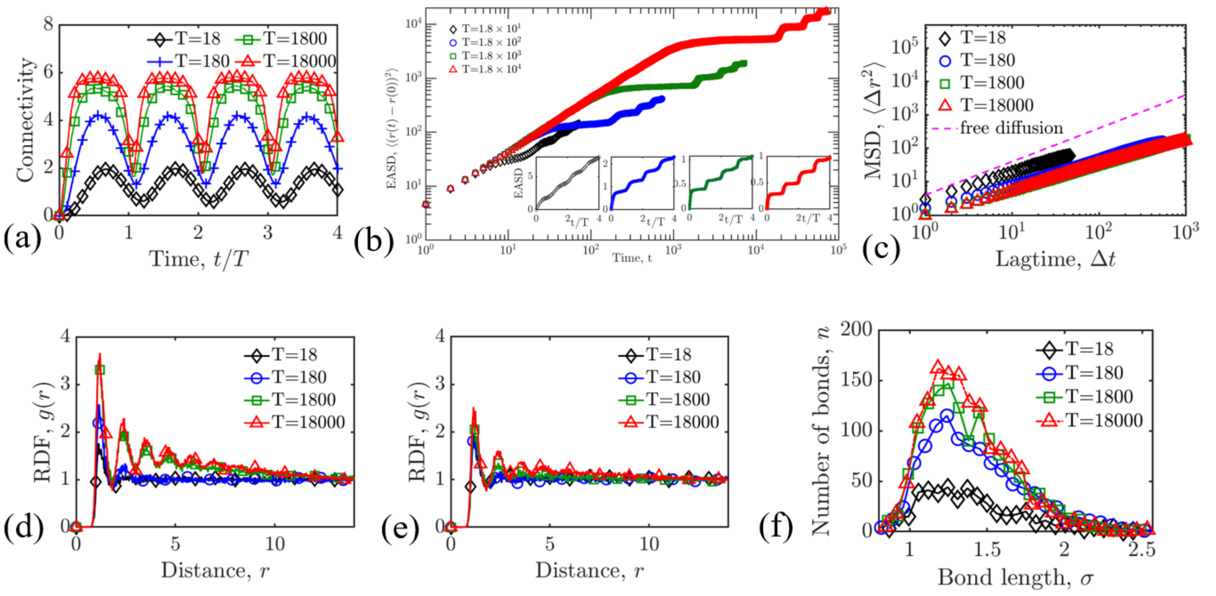

Figure 2.2: Four systems with different crosslinker oscillation periods ranging from $T = 18$ to 18000 with a packing fraction of 30% are simulated. (a) The levels of connectivity are plotted over time for each of the oscillation periods, measuring the average number of bonds each colloid is connected to over 4 cycles. (b) The EASD curves are plotted, measuring the network movement beginning at $t = 0$. (c) The MSD for the systems, with the free diffusion slope. (d) and (e) The RDF curves are sampled at the ordered and disordered states, respectively. (f) The bond length distributions are sampled at the ordered state.

configurations that illustrate the behavior of the network and provide insight into the structure of the network and clustering for different parameters.

2.3 Results and Discussion

2.3.1 Impact of varying crosslinker oscillation period

First, we discuss the time evolution of the structure and dynamics of the system as we vary the crosslinker oscillation period for a fixed colloid packing fraction of 30%. Our measurements of system-wide connectivity, ensemble average squared displacement, mean squared displacement, radial distribution function, and bond length distribution, shown in Fig. 2.2, demonstrate that the system repeatedly transitions between a highly crosslinked, ordered state, and an unlinked, disordered state.

We observe clear oscillations in the average connectivity of the colloidal system, and these oscillations between states of high connectivity and low connectivity are more striking as the oscillation period T is increased as shown in Fig. 2.2(a). For example, when $T = 18$, the connectivity oscillates between 0.5 to 2 indicating that the system stays in a disordered, fluid-like state, and the colloids do not form any noticeable spanning networks. Because the smaller oscillation periods yield shorter bond lifetimes, they effectively reduce the time the system takes to attain peak connectivity. Increasing the crosslinker period to $T = 18000$ yields a peak connectivity of ~ 6, which corresponds to the largest coordination number for a two-dimensional network in equilibrium, indicating a very ordered state, and a trough of ~ 2 indicating a disordered state. Intermediate values of T lead to intermediate values of the peak connectivity and the amplitude of oscillation. We also see that for $T = 180$ the system spends comparable times in the ordered and ordered states, and as we increase T, the residence time in the ordered state increases while that in the disordered state decreases. These observations can be attributed to the direct dependence of the lifetime of individual crosslinkers on the crosslinker oscillation period T, and to the separation between T and the diffusion time of the colloids. As T increases, both these quantities increase allowing the system to form states with larger and larger connectivities until a maximum value of 6 is reached, and these connected, ordered states also stay intact for longer times before the crosslinkers come apart and the colloids are unlinked. Since the residence times in an ordered and a disordered state for a given T should add up to give half the oscillation period, as the former increases, the latter decreases. We also observe that the residual order at the disordered states increases in proportion to the oscillation period. This is a consequence of the residence time imbalance. Larger oscillation periods produce well-ordered states with high levels of connectivity, and since those systems spend severely reduced times in the disordered state, they do not have enough time to dissolve back to a completely unconnected state before the next oscillation cycle starts and the crosslinkers begin to connect particles together.

When $T = 1800$, the fixed lifetime lasts long enough for a spanning cluster formation

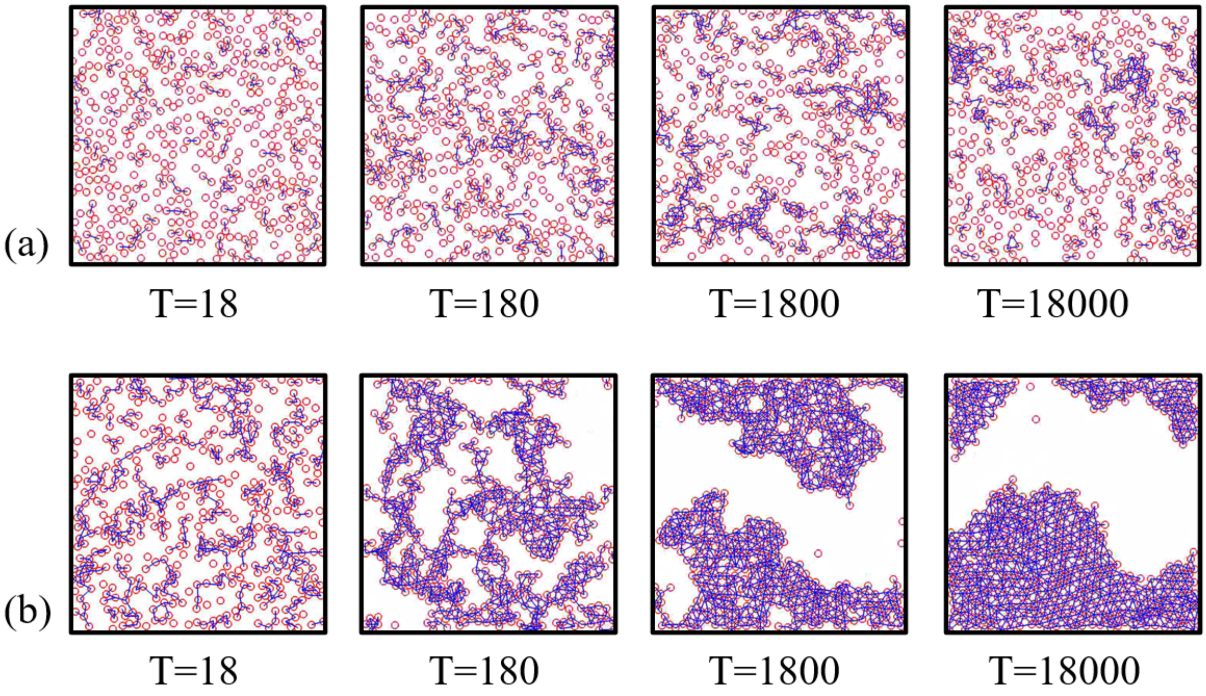

Figure 2.3: System configurations sampled over (a) the disordered states and (b) the ordered states.

to occur and although the relaxation time for the colloids is still reduced, the system connectivity drops from nearly 5.5 to 1.75 bonds per particle. For the $T = 18000$ case, the fixed lifetime of the ordered state is much longer, as demonstrated by the flatter peaks in Fig. 2.2(a). While the difference in ordered-disordered state is about 4 bonds per particle, the relaxation intervals become even shorter, implying that the growing separation between the relaxation timescale and oscillation timescale leads to a greater imbalance of residence times in the ordered and disordered states.

We show the ensemble average squared displacement(EASD) as a function of time in Fig. 2.2(b). For a given time interval, the slope of the EASD curves indicates the mobility of the system. For the system with the shortest period of $T = 18$, the connectivity remains small even in the ordered state, and the difference in the slopes during the “ordered” and “disordered” intervals is small. The EASD curves for the systems with the three larger T values, however, show distinct oscillations in mobility, with the plateaus indicating network formation. For $T = 1800$ and 18000, the slopes of the EASD curves stay ~ 0

for longer times than that of $T = 180$, which is expected since the smaller period of 180 corresponds to shorter bond lifetimes, leading to particles having the opportunity to unlink and move about more frequently. The insets in Fig. 2.2(b) show the same data but are plotted in linear scale and with the time scaled by the crosslinker oscillation period. This illustrates the patterns of mobility in the system as each oscillation period occurs; here, a stair-stepping pattern can be clearly seen for all the above cases. When the slopes become approximately zero, this signifies the systems' movement slowing down as they cycle up to an ordered state. Then, as the slopes begin to increase, the systems dissolve back to a disordered state.

The MSD curves in Fig. 2.2(c) show that the smallest oscillation period $T = 18$ yields the highest rate of diffusive motion. This is expected as shorter crosslinker periods produce correspondingly shorter bond lifetimes, so the system is weakly connected throughout the simulation. As T increases, the data shows that the particles are diffusing significantly slower. Because the bond lifetimes are related to the oscillation period, more particles remain connected for longer time intervals and cannot diffuse as freely, consequently resulting in lower rates of diffusive motion. Across all four systems, the particle motion, while still largely diffusive, has a noticeable departure from free diffusion, particularly as the crosslinker time-period increases.

To gain more insight into the translational order in the system in the ordered and disordered states, we calculate the RDF for each of the systems. In both Fig. 2.2(d) and (e), as the oscillation period increases, the number of peaks increases, signifying the longer oscillation periods yield systems that achieve distinctly well-ordered states, confirming the observations made from the connectivity curves. In the RDF curves, there is a pronounced difference between the ordered and disordered states for $T = 1800$ and 18000. The number of peaks in the curves and the heights and sharpness of those peaks increase in comparison to those in Fig. 2.2(e). For the two shorter oscillation periods $T = 18$ and 180, the RDF curves are nearly identical in terms of the peak heights and noise, which implies that the degree of order in the system does not change much between the ordered and disordered

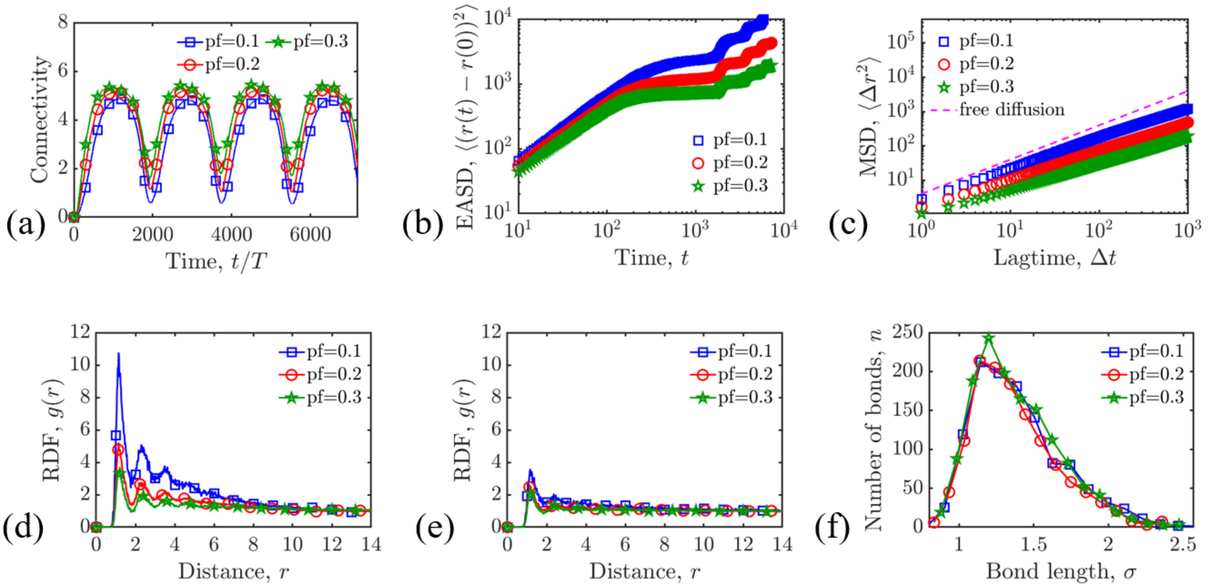

Figure 2.4: Three systems with different packing fractions ranging from 10% to 30% and a fixed oscillation period of 1800 are simulated. (a) Connectivity is plotted over time for 3 packing fractions with the oscillation period $T = 1800$. (b) The EASD curves, starting from the beginning of the simulation. (c) The MSD curves, with the free diffusion curve plotted alongside. The RDF is sampled at (d) the ordered state, located at the peaks of the connectivity curve, and (e) the disordered state, occurring at the troughs of the connectivity results. (f) The bond length distribution corresponds to the particle bonds that are formed in the ordered state.

states. The colloids do not have the chance to form a large, well-connected network, and stay in a weakly connected state, leading to a subtler distinction between the two states.

Next, we study the bond length distributions in the ordered states to understand the connectivity properties of the clusters (see Fig. 2.2(f)). For larger T, the bond length distributions are narrower. The systems with longer oscillation periods form large single spanning networks in the ordered states, subsequently leading to most particles with $\sim 5-6$ nearest neighbors. Because a majority of the particles have a similar high nearest neighbor count, the minimum energy configuration of the system will correspond to a narrow distribution of bonds lengths which is peaked very close to the crosslinker rest length. As the oscillation periods decrease, the bond length distribution becomes wider. This is due to the formation of smaller and less connected clusters at smaller T. Since the colloids do not form one large single spanning cluster, some of the particles may have close to 6 nearest neighbors or connections, while particles belonging to other clusters may have significantly fewer nearest neighbors.

In Fig. 2.3, we show particle configurations at the disordered and ordered states of each of the systems. For the shortest oscillation period $T = 18$, the system only transitions between disordered to slightly connected states. In the ordered state, the system has slightly larger connectivity, but the particles do not form distinct clusters. However, as we increase T to 180 and 1800, the system begins to oscillate between disordered states with minimal connectivity to ordered states with larger cluster formations. At the longest period $T = 18000$, the system can repeatedly form a large, strongly connected network and transition back to a disordered, weakly connected network.

2.3.2 Impact of varying colloidal packing fraction

We next examine the effect of varying the packing fraction. We explore systems with an oscillation period of $T = 1800$ and simulate 3 cases with a packing fraction range of $10-30\%$. We keep the oscillation period constant at 1800 so as to allow clearer transitions between ordered and disordered states compared to $T = 18$ and 180 and to reduce the gap between residence times in these states compared to that obtained with $T = 18000$. The system is again kept dilute to allow oscillations based on the rhythm of the crosslinkers rather than spontaneous formation of a large connected network, which happens in a dense system.

Higher packing fractions generate systems with more particles within a given distance corresponding to the crosslinker rest length, thereby leading to a larger level of connectivity on average. All three systems in Fig. 2.4(a) can transition between states with ~ 5.5 to 1 bonds per particle, which confirms the colloidal networks are able to oscillate between well-connected to very weakly connected states. Across the packing fractions, the systems still produce reduced residence times in the disordered states and comparatively larger durations in the ordered states. The packing fraction does not affect this imbalance of residence times. The results from the ensemble averaging in Fig. 2.4(b) show that the

EASD steadily increases with time at the beginning of the simulation but after $t = 180$, there is decreased mobility in the network as the slopes of the EASD curves become nearly zero, suggesting that particles become locked into a network or cluster relatively early in the first cycle. A stair-stepping phenomenon is present in all 3 cases, emphasizing the network movement increasing and decreasing over each of the oscillation cycles as the system transitions between ordered to disordered states. The MSD curves show that all three systems are diffusive, but the diffusivity decreases as the packing fraction increases, which is seen clearly when compared against free diffusion in Fig. 2.4(c). Systems with the two higher packing fractions have smaller diffusivities; with larger packing fractions, the systems will be able to form larger networks that can eventually span the system (see system with pf=0.3), which leads to more particles having restricted mobility.

We next examine the RDF for the systems at low and high periods of connectivity. There is a considerable difference in the degree of order between the states. As a general trend, as the packing fraction increases, the height of peaks in the RDF curves decreases as a result of a larger normalization factor in the denominator. This effect is seen in both the ordered and disordered states (Fig. 2.4(d) and (e)). For the higher packing fractions, large spanning clusters are formed while for lower packing fractions, we observe several smaller clusters, which is why the RDF curve for the 10% packing fraction case has the highest peak at an interparticle distance of 1. In the disordered state (Fig. 2.4(e)), the RDF curves for all three systems have about two discernible peaks and a similar amount of noise, indicating the systems have a low degree of system order during this state. However, in the ordered state, the RDF curves demonstrate the systems achieve a significant increase in the level of order as the number of peaks increases for each of the cases and the sharpness of those peaks is more apparent. The bond length distribution for the ordered states of the system is shown in Fig. 2.2(f). The highest packing fraction of 30% yields a well-connected state with a narrow bond length distribution, and the two systems with the smaller packing fractions produce several smaller clusters that are less connected and lead to a wider distribution of bond lengths.

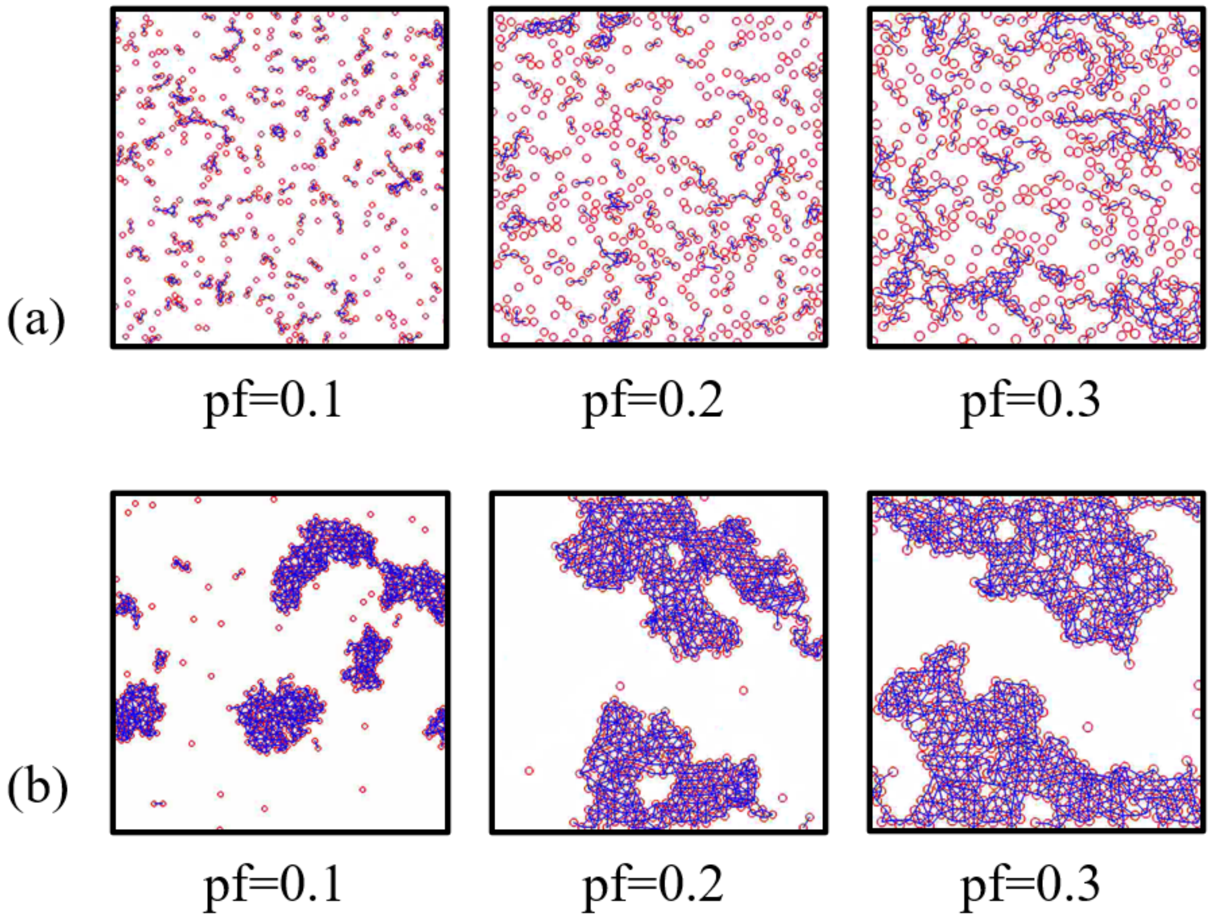

Figure 2.5: System configurations sampled over (a) the disordered states and (b) the ordered states.

Sample configurations of each system at low and high network connectivity are generated for all 3 systems in Fig. 2.5. The configurations illustrate that the systems tend to oscillate between weakly connected structures with minimal cluster formation and tightly connected networks with bigger clusters. As the packing fraction is increased, the clusters become larger and the particles experience more instances of crosslinking.

2.3.3 Phase Diagrams

Next we show the results for the residence times in the ordered and disordered states as a function of the oscillation time-period (T) and colloid packing fraction. In Fig. 2.6, the ratio of peak-to-trough durations (t/T) are plotted on a bar chart. From this, the results suggest there is a significant imbalance in residence times for systems with larger crosslinker periods. We see that across all three packing fractions, the systems with $T = 18000$ spend disproportionately long times in the ordered states and markedly brief times in the disordered states. The system with a packing fraction of 10% and a period of 18000 has the highest ratio; that is because the system is capable of cycling down to an acutely disordered state that is only maintained for a very brief amount of time. As we decrease T, the residence times between the two intervals become smaller as the gap between the separation of the relaxation timescale and crosslinker oscillation timescale is reduced. The smallest period of 18 leads to systems having comparable times in the peak and trough intervals, but the system did not reach a distinctly well-ordered state and only achieves a disordered state that is weakly connected, with no cluster formation.

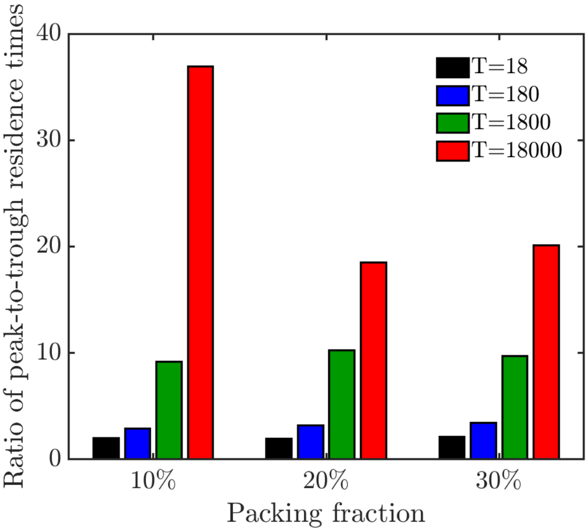

Figure 2.6: Bar chart describing the ratio of peak-to-trough residence times.

To systematically illustrate how the colloidal packing fraction and crosslinker oscillation period T influence the degree of connectivity in the ordered and disordered states, we show how twice the amplitude of the oscillations in the measured connectivity varies with these quantities in Fig. 2.7(a)-(c). Figure 2.7(a) shows that T controls the amplitudes. Larger values of T produce systems with pronounced differences in the connectivity of the ordered and disordered states, with the packing fractions having very little effect. The phase diagram shows that the oscillation period of $T = 18$ produces the smallest amplitude while the largest oscillation period $T = 18000$ yields the largest amplitude of about 2.75 bonds per particle.

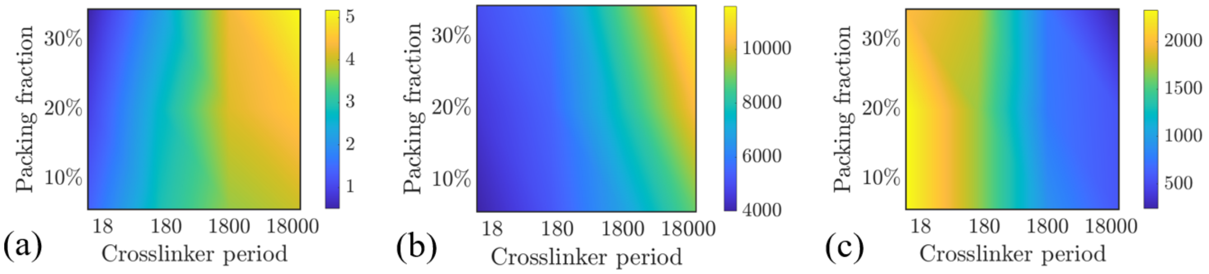

Figure 2.7: Phase diagrams demonstrating the impact of the packing fraction and crosslinker oscillation period. (a) Phase diagram illustrating twice the amplitude of connectivity oscillations between disordered and ordered states. (b) Phase diagram characterizing the duration of the ordered states. (c) Phase diagram emphasizing the residence times of the relaxed states at the trough.

We next show how the residence times in the ordered states are influenced by the packing fraction and T (see Fig. 2.7(b)). This is done by measuring the widths of the peaks from the connectivity results, where time is further scaled by T. For the smaller crosslinker periods $T = 18$ and 180, all three systems have similar durations spent in the ordered state and the packing fraction has no impact on the lengths of those intervals. As T is increased to 1800 and 18000, the systems with the larger packing fractions have longer residence times in the ordered states, with the packing fraction of 30% and $T = 18000$ producing the largest residence time. For the smallest packing fraction of 10%, the residence times in the ordered states are shortest across all four periods, due to particles being farther apart and having to diffuse more to interact and form bonds. Similar to the patterns of amplitude heights in Fig. 2.7(c), the driving factor behind the residence times of the disordered states is the crosslinker period length rather than the packing fraction; we observe that the time spent in the disordered state decreases as the crosslinker time-period is increased and vice-versa.

2.4 Conclusion

We constructed and investigated a colloidal system that can repeatedly undergo order-disorder transitions when rhythmically crosslinked. We explored systems with colloidal packing fractions ranging from 10% to 30% and crosslinker oscillation periods of 18 to 18000. We observed sustained oscillations between distinct states with substantially different degrees of connectivity. Larger oscillation periods lead to ordered states with larger connectivity and residence times, but also greater imbalances in residence times between the ordered and disordered states. This is presumably due to several orders of magnitude of separation between the diffusion time of the colloids and the oscillation time-period of the crosslinkers. When these timescales are comparable in magnitude (for example, when $T = 18$), the system spends comparable times in the ordered and disordered states but the difference in the degree of order between these two states is very small.

Our results demonstrate that we can achieve distinct states of this colloidal system with pronounced differences in order and material properties when the crosslinker kinetics are governed by the oscillation period. Furthermore, large residence times in the ordered state can be obtained when the crosslinker lifetime depends directly on the oscillation period and this oscillation period is much larger than the colloidal diffusion time. These findings provide insights into the rational design of soft materials that can rhythmically transition between states with different material properties on a pre-determined schedule. Bottom-up construction of such materials, both in experiments as well as *in-silico*, will provide an understanding of the general principles and mechanisms underlying how time-varying environments and time-keeping machineries shape the dynamic collective properties of living systems [2–4] with potential for application in soft robotics [35]. We published our results from this model in the Soft Matter journal in March 2022 [36].

Chapter 3

Self-organization of Eukaryotic and Prokaryotic Biopolymers in-vitro Driven by Depletants and Attractive Intermediaries: I. Actin and PEG, and II. DNA and DPS.

3.1 Actin and PEG

3.1.1 Background

Biological systems have the unique ability to self-assemble and respond to external mechanical stimuli. The mechanical integrity and mechanical response of cells is largely due to the cytoskeleton, a polymeric scaffolding which gives structure and shape to living cells [37]. The cytoskeletal network is made up biopolymers, crosslinkers, and motor proteins [38]. The biopolymer actin is a major component of the cytoskeleton. These filaments are semi-flexible, i.e. it costs energy to both stretch and bend these filaments. They can form

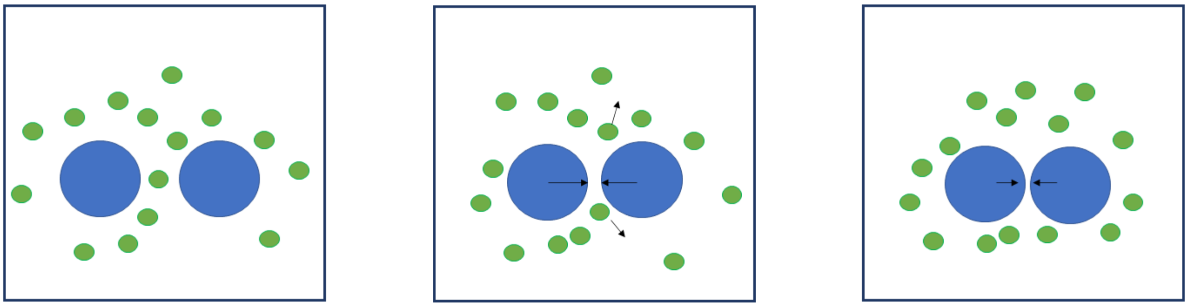

Figure 3.1: Schematic of depletion interactions of larger colloid particles immersed in a solute of smaller, non-adsorbing particles.

large spanning networks or bundles. Previous studies have shown formation of networks and bundles of actin filaments when connected via crosslinking proteins [39–42]. This involves the direct, physical binding of proteins such as myosin, fascin, α-actinin, and filamin to actin filaments to be the driving mechanism for complex networks to form [43–46]. However, protein-binding mechanisms are not the only way to induce or manipulate self-assembly of networks and bundles.

Depletion forces are a recent focus for self-assembly of smart active materials [47–49]. Depletion interactions occur when larger-sized particles, such as colloids, are in a solution surrounded by a greater ratio of smaller particles called depletants. The free energy of the larger colloids reaches a minimized energy state, when they are in relatively close proximity of one another. There is a region around each colloid that the smaller particles are excluded from occupying due to steric repulsion. When the colloids get sufficiently close these excluded volume regions can overlap, leading to a decrease in the net volume that the smaller particles are excluded from accessing. The result is an effective attractive interaction between the colloids, while the excluded smaller particles end up surrounding the colloids but cannot break through the depletion zone due to excluded volume, keeping the colloids close together, as visualized in Fig. 3.1. So the smaller particles act as the depletant, keeping the large colloids in a cluster. The concentration and size of the smaller particles can effectively tune the effects of the depletion interactions. Similar depletion interactions can be recapitulated in actin systems with appropriate crowding agents or depletants as shown in Fig. 3.2. In the first panel of Fig. 3.2, the actin filaments and smaller particles are in a random, disordered state, with no visible bundling and the solution of smaller particles is also assumed to be evenly well-mixed in the box. Due to the depletion interactions described above, the actin filaments experience effective attractive interactions with one another and transition from a phase made of individual filaments to one that is more network-like (see the third panel of Fig. 3.2) and eventually, if the depletion interaction forces are large enough, they lead to a network of actin bundles. In our simulations, we do not explicitly introduce depletion interactions. We use a modified Lennard Jones potential to model interactions which is discussed further in section 3.1.3. The impact of depletion interactions is an emergent behavior of our model.

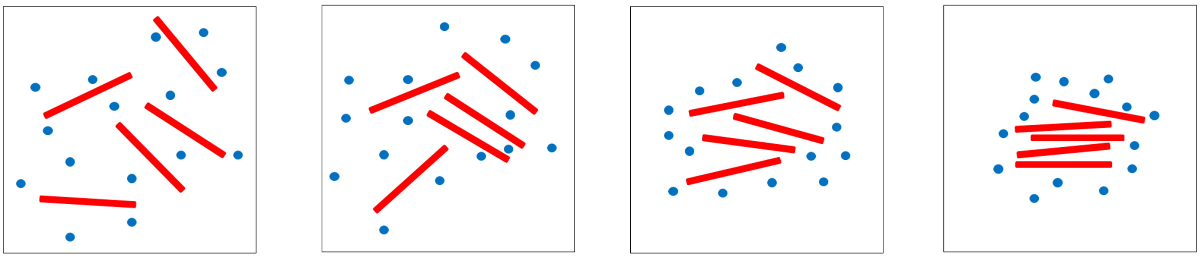

Figure 3.2: Model schematic of actin and PEG polymers. Actin filaments experience depletion interactions in a crowding environment with PEG proteins as the depletant. Initially, the actin filaments are individual and in random positions. Then as the actin begin to cluster together, due to the repulsive actin-PEG interactions and attractive PEG-PEG interactions, they gradually reach a more bundled state.

Polyethylene glycol (PEG) is a well-known polymer with a sufficiently small radius of gyration that it can replicate a crowding environment and cause depletion interactions in solutions with colloids or filamentous proteins, like actin and microtubules [47, 50, 51]. Rather than the PEG polymers directly binding to actin, the natural crowding behavior of the PEG can help an actin system transition from individual filaments to a strongly bundled system [47]. Previous studies have shown that varying the concentration ratio of actin to PEG and simply increasing the PEG concentration by itself will yield systems of actin with corresponding degrees of bundling [47, 50–52]. However, understanding how to tune the actin system transitions based on the molecular characteristics of the PEG polymers is still unclear [47]. Experimentalists are exploring how varying the concentration and molecular weight drives the depletion-induced bundling of actin filaments [47]. In tandem, we construct and simulate a theoretical model of actin filaments immersed in a PEG solution to make predictions and help guide the experimental study design.

3.1.2 Scaling Arguments: Fixed Number Density vs. Fixed Mass Density

Over the past decades, studies have been done to explore how increasing the concentration of depletants and depletant size leads to increased depletion interaction strength [48, 53–55]. However its been observed that cells tend to keep a fixed total protein density throughout their internal cycle [56]. Thus, examining systems with a fixed mass density and number density is important to understanding the dynamic properties of living systems. We want to understand how fixing the mass density or number density tunes depletion interaction strength. In particular, the research question of fixed mass density has not been thoroughly explored as most experimental in-vitro studies of depletion interactions keep volume fractions fixed instead.

Colloid Depletion

To determine how the fixed number density of PEG affects the depletion interaction strengths, we explore the Asakura-Oosawa (AO) model [57] for the fixed number density case. We consider a system where we have 2 colloid particles, with a fixed diameter σ, in a system with smaller spherical particles acting as the depletants, with a diameter τ and density n (this system is depicted earlier in Figure 3.1). We then describe the interaction potential between the 2 colloids by the following equation:

$$U(d) = -nk_BTV_{overlap}(d),\ d \leq 1 \tag{3.1}$$

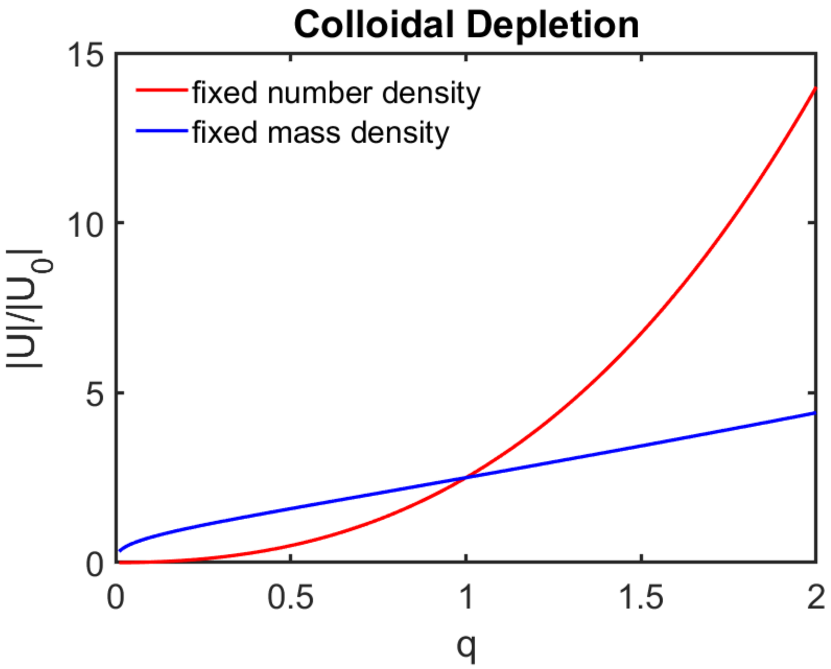

Figure 3.3: Plot of q-dependent part of the depletion interaction potential $\frac{U^*}{k_BT}$ to emphasize how q tunes the depletion interaction strength for 2 colloid spheres.

The Boltzmann constant is given by k_B, temperature is represented by T, and $V_{overlap} = \frac{\pi}{6}\sigma^3(1+q)^3\left(1-\frac{3}{2}d+\frac{1}{2}d^3\right)$ represents the overlap volume. The distance normalized by the maximal extent of the depletion interaction is given by $d = \frac{D}{\sigma(1+q)}$, where $D = \sigma$, representing the center-to-center distance between 2 colloids, and $q = \frac{\tau}{\sigma}$ is the size ratio. To find the maximum value U^* of the depletion interaction potential and explore how the number density n affects U^*, which is when two colloids are in contact, we can first set $d = \frac{1}{1+q}$. For the fixed number density case, we have the following expression for U^*:

$$\frac{U^*}{k_BT} = -n\frac{\pi}{6}\sigma^3(1+q)^3\left(1-\frac{3}{2}d+\frac{1}{2}d^3\right) \tag{3.2}$$

For the Asakura-Oosawa model, this interaction potential holds for q values less than 1 [57]. In this expression for fixed number density (Equation 3.2), we can Taylor expand the expression which gives us a dependence of maximal depletion force going as q^2. Note that this pertains only to the smaller PEG sizes in simulations. These simulations allow us to examine what happens beyond this limit when q is equal to or greater than 1.

For the fixed mass density case, we let ρ represent the fixed mass density of the depletants. Using the Flory scaling relation for polymers [58], we set $\rho = M_W n \sim R_g^{5/3} n$, where M_W stands for molecular weight and R_g is the radius of gyration. We then substitute our expression for ρ into Equation 3.1 and get the following:

$$\frac{U^*}{k_BT} \sim -\frac{\pi}{6}\rho\sigma^{4/3}\frac{(1+q)^3}{q^{5/3}}\left(1-\frac{3}{2}\frac{1}{1+q}+\frac{1}{2}\frac{1}{(1+q)^3}\right) \tag{3.3}$$

This results in the interaction potential U^* scaling with $q^{1/3}$, which indicates that the depletion interaction strength increases as the size of the depletant increases for a case with fixed mass density. This leads us to theorize that as the PEG radius increases, the strength of the depletion interactions also increases for systems with a fixed mass density.

In Figure 3.3, the q-dependent part of the depletion interaction potential, $|U|/|U_0|$ is plotted against q to show how the strength of depletion interactions scale for cases with fixed number density and mass density, where $|U_0|$ is the $q-$ independent prefactor in the expression for U^*. For fixed number density, $|U|/|U_0|$ increases approximately exponentially, while for fixed mass density, it increases more slowly, approximately as a power law curve; this scaling is exact below the limit $q = 0.1547$ where the AO pair depletion potential is the only interaction contributing to the exact effective interaction between the colloids [59].

Cylindrical Rod Depletion

Our system involves actin filaments as the components experiencing depletion. So, we also explore a case where we approximate the actin filaments as cylindrical rods with a cross-sectional diameter σ. We explore two cases for U^*: non-parallel rods and then parallel rods. For the non-parallel case, the maximum depletion interaction potential is described by $\frac{U^*}{k_BT} = -\frac{\pi}{2}n\sigma\tau^2 = -\frac{\pi}{2}nq^2\sigma^3$ [60], where $q = \frac{\tau}{\sigma}$. For a system with fixed number density, n, $U^* \propto q^2$. For the parallel cylinders, $\frac{U^*}{k_BT} = -\frac{2\sqrt{2}}{3}Ln\tau^{\frac{3}{2}}\sigma^{\frac{1}{2}}$, where L is the length of an actin filament. For fixed number density, $\frac{U^*}{k_BT} = -\frac{2\sqrt{2}}{3}Ln\sigma q^{\frac{3}{2}}$.

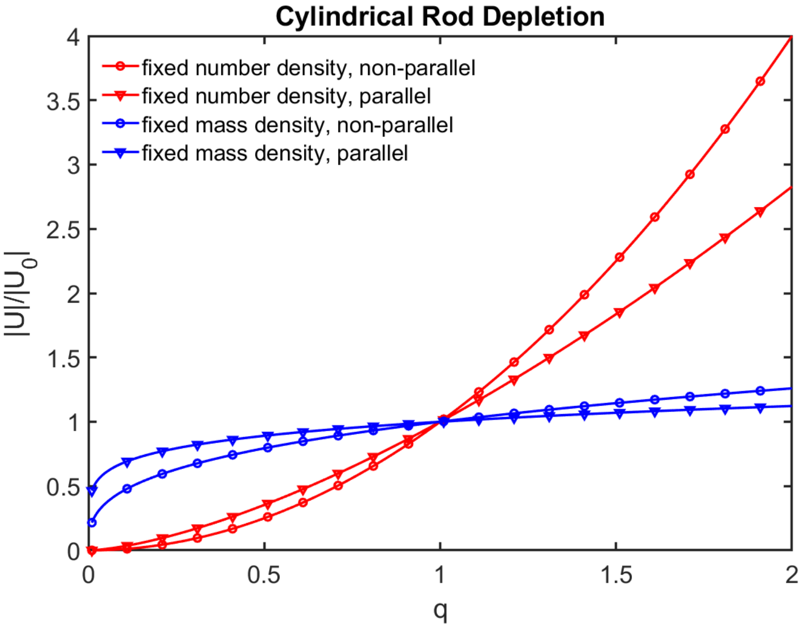

Figure 3.4: Plot of q-dependent part of the depletion interaction potential $\frac{U^*}{k_BT}$ to emphasize how q tunes the depletion interaction strength for a case of cylindrical rods.

For a system with fixed mass density, $\rho = M_W n \sim \tau^{\frac{5}{3}} n$, we get $\frac{U^*}{k_BT} = -\frac{\pi}{2}\sigma^{\frac{4}{3}}\rho q^{\frac{1}{3}}$, giving $U^* \propto q^2$. For a case with parallel rods, $\frac{U^*}{k_BT} = -\frac{2\sqrt{2}}{3} L n \tau^{\frac{3}{2}} \sigma^{\frac{1}{2}}$. This expression simplifies to $\frac{U^*}{k_BT} = -\frac{2\sqrt{2}}{\pi} L \sigma^{\frac{2}{3}} q^{\frac{1}{6}}$.

These expressions only hold in the dilute and semi-dilute limit where $\frac{\pi n \tau^3}{6} << 1$. For dense systems, where this condition is violated, the PEG number density n in the expression for $\frac{U^*}{k_BT}$ should be replaced by nZ, where $Z = \frac{1+\eta+\eta^2-\eta^3}{(1-\eta)^2}$ and $\eta = \frac{\pi n \tau^3}{6}$.

We plot $|U|/|U_0|$, the q-dependent part of the depletion interaction potential, against q for both the parallel and non-parallel cases for fixed number and mass density in Figure 3.4. The fixed number density trajectories show a positive exponential rate for both the non-parallel and parallel case. For the curves corresponding to fixed mass density, the scaling resembles a log-curve with the magnitude of the interaction potential being slightly higher for the parallel case. With the analytical scaling arguments, the depletion strength increases as the depletant size increases with a fixed mass. Note that these scaling arguments are only valid for small size ratios q as described earlier. We use simulations to explore the size ratios q beyond the small $q-$ limit of AO theory.

3.1.3 Model and Method

Mathematical Model

In order to understand the underlying depletion mechanisms, our **approach** is to compare the experimental results to our 3D phenomenological model, which consists of actin filaments interacting with PEG particles in three dimensions. Each actin filament is modeled as a chain made of beads, and the relative cost of stretching and bending the chain is informed by known mechanical properties of actin filaments. We model the pairwise interactions between any two particles, whether belonging to actin bead-chains, or PEG, or between actin and PEG using a Lennard Jones potential,

$$V_{LJ} = 4\epsilon \left[\left(\frac{\sigma_{ab}}{r_{ij}} \right)^{12} - \left(\frac{\sigma_{ab}}{r_{ij}} \right)^{6} \right], \tag{3.4}$$

where $\sigma_{ab} = (\sigma_a + \sigma_b)/2$, where σ_a and σ_b represent the diameters of two reference beads. The interparticle distance between two reference particles with indices i and j is denoted by r_{ij} and the strength of the interaction's potential is defined by ϵ. The interaction potential is truncated to incorporate only repulsive interactions representing a hard core for actin-PEG interactions, while for PEG-PEG and actin-actin interactions we additionally allow attractive interactions to mimic the Van-der Waals interactions.

The motion of the PEG particles follows the overdamped Langevin equation,

$$\frac{d\mathbf{r}}{dt} = \frac{D}{k_B T} \mathbf{F}_{LJ} + \sqrt{2D}\eta \tag{3.5}$$

where the interparticle interaction force F_{LJ} is derived from the Lennard Jones potential defined above, and the thermal diffusion is represented by the noise term $\sqrt{2D}\eta$, where D is the diffusion constant and η is a vector drawn from a Gaussian distribution with a mean of 0 and variance of 1; k_B and T are the Boltzmann constant and room temperature. The motion of an actin bead in strand i is also given by an overdamped Langevin equation,

$$\frac{d\mathbf{r}}{dt} = \frac{D}{k_BT}\left(\sum \mathbf{F}_{LJ_{ij}} + \sum \mathbf{F}_{LJ_{jk}} + \sum \mathbf{F}_{LJ_{il}}\right) + \frac{D}{k_BT}\left(\sum \mathbf{F}_{s_{ij}} + \sum \mathbf{F}_{b_{ij}}\right) + \sqrt{2D}\eta \quad (3.6)$$

where $\mathbf{F}_{LJ_{ij}}$, $\mathbf{F}_{LJ_{ik}}$, and $\mathbf{F}_{LJ_{il}}$ are the Lennard Jones interparticle forces, and indices i and j describe intra-strand pairwise interactions, i and k describe inter-strand interactions, and i and l describe interactions between actin and PEG particles. The actin filaments resist stretching (or compression) and bending with forces $\mathbf{F}_{s_{ij}}$ and $\mathbf{F}_{b_{ij}}$, respectively, obtained from the corresponding stretching and bending deformation energies, $U_s = \frac{\alpha_S}{2}(l - l_0)^2$ and $U_b = \frac{\alpha_B}{2}(\theta - \theta_0)^2$. In the equations above, l represents the distance between two nearest-neighbor actin beads in a strand, and l_0 describes the equilibrium rest length for actin beads which is given by the actin bead diameter. The stretching stiffness is $\alpha_S = 100$, the bending rigidity is $\alpha_B = 100$ and θ is the angle between three sequential actin beads and the equilibrium value of this angle, θ_0, is set to π.

We solve both Langevin equations using the Forward Euler-Maruyama approach. The timestep dt is set to 10^{-3} and each simulation was run up to 500τ, so the system had enough time to equilibrate and reach a steady state.

Simulation parameters

The actin bead-chains and have a uniform length of 160nm and bead diameter (σ) of 8nm, and the diameter of the PEG spheres is varied from 0.25σ to 0.75σ . All distances in the simulations are scaled by σ, and all times by the time (τ) it takes for a bead in an actin bead-chain to diffuse across a distance σ. The diffusion coefficient for a freely diffusing actin monomer is estimated to be $10^1\mu\text{m}^2\text{s}^{-1}$, which gives $\tau = 0.1$s [61]. All energies in the model system are scaled by k_BT. The simulation box size is set to 75σ by 75σ by 10σ across all simulations, and periodic boundary conditions are enforced.

To understand how the (1) concentration and (2) molecular weight of the PEG particles influenced the actin bundling, we vary (1) the number of PEG particles from 4000 to 10000 while keeping the simulation box volume unchanged and (2) PEG particle radius from 2nm to 6nm, respectively. To convert from PEG radius of gyration (R_g) to molecular weight (M), we assumed the classic result from Flory theory, $R_g \propto M^{\frac{3}{5}}$. This gives molecular weights of 6k, 20k, and 37.4k for radii of 0.25σ, 0.5σ, and 0.75σ respectively. The PEG concentration is varied from $4000\frac{V_\rho}{V_{box}}$, $5000\frac{V_\rho}{V_{box}}$, $6000\frac{V_\rho}{V_{box}}$, and $10000\frac{V_\rho}{V_{box}}$, where $V_\rho = \frac{4}{3}\pi r^3$, r representing the effective radius of and V_{box} is the volume of the simulation box which is 56250 σ^3. We explore 12 different systems to determine the effects of PEG concentration and effective molecular weight. The number of actin filaments is held constant at 200 for all 12 systems.

For the Lennard Jones pairwise interactions, $\epsilon_{PEG-PEG}$ is set to 1.25 for attractive interactions and 1.0 for repulsive interactions; $\epsilon_{actin-actin}$ is set to 0.3 for attractive interactions and 1.0 for repulsive interactions. We encode only repulsive interactions between the PEG beads and the actin strands, and $\epsilon_{PEG-actin}$ is equal to 2.0. We use a modified Lennard Jones potential in which we independently tune the strengths of the attractive and repulsive interactions to mimic the interactions between the PEG and actin in a way that is experimentally meaningful. The depletion effect of PEG is an emergent phenomenon in our simulations. Furthermore, by tuning the PEG-PEG attractive interactions from the Lennard Jones potential, this allows us to include the PEG-based chemistry observed in experiments [47].

3.1.4 Results and Discussion

Fixed Number Density

The 12 systems simulated qualitatively agree with the experimental results measuring the degree of bundling. Fig. 3.5(a) shows the configurations of the equilibrated actin-PEG model systems juxtaposed with the phase diagram describing the degree of bundling in the experiments. With the PEG molecular weight set to 6k, the configurations show a disordered actin system with minimal bundling present across all four concentrations of

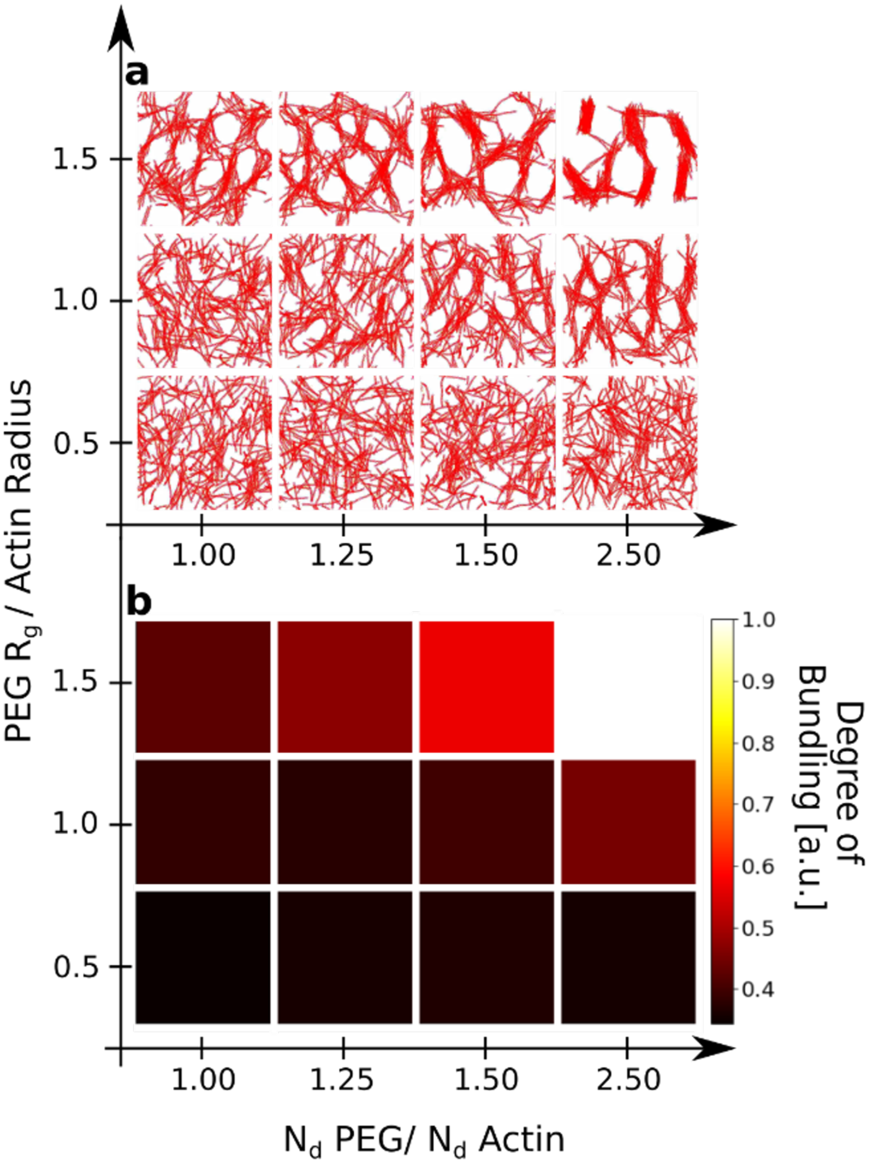

Figure 3.5: (a), The figures shows the simulated equilibrium morphologies of the networks and bundles of actin filaments in the presence of PEG, and demonstrates the role of PEG molecular weight and concentration on the actin filament bundling. As the molecular weight increases (y-axis), significant bundling of actin filaments is observed. Similarly, increasing the concentration of PEG (x-axis) also leads to appreciably more pronounced bundles of actin once the molecular PEG weight is greater than 6k. (b), Degree of bundling results show that the model system moves toward more bundled structures when the molecular weight and concentration of PEG molecules are increased. The term N_d represents the number density of each component. As the PEG molecular weight and concentration is increased, the actin solutions have stronger formation of bundling.

PEG. These model images are directly comparable to the phase diagram of the experimental results measuring the degree of bundling in Fig. 3.5(b). To quantify the degree of bundling in simulations, we sampled simulation snapshots at the final time-frame $t = 500$. Then we use in-house Python code for skeletonizing the images and quantifying the identifiable nodes in the actin network was used to establish the degree of actin bundling [47]. A larger number of nodes in an actin image indicates a higher degree of bundling for that system. The results in Fig. 3.5(b) show that all four simulated cases yield similar low degrees of bundling for the smaller PEG radii.

As the PEG molecular weight is increased to 20k, a noticeable amount of bundling is present as the PEG concentration is increased from $6{,}000\frac{V_\rho}{V_{box}}$ to $10{,}000\frac{V_\rho}{V_{box}}$. Between these two systems, we begin to see distinct bundling formation, but the system configurations still show the system forming a network-like structure instead of distinct stacks of parallel filaments forming bundles. This increase in degree of bundling is also observed in systems for a molecular weight of 20k and concentration of $10{,}000\frac{V_\rho}{V_{box}}$.

For the largest PEG molecular weight, 37.4k, the amount of bundling increases significantly along with the concentration of PEG. In particular, the first 3 PEG concentrations show a defined, mesh-like actin network formed by defined filament bundles. The sharpness of these bundles grows as the PEG concentration is increased. The largest concentration of $10{,}000\frac{V_\rho}{V_{box}}$ yields a very distinct system of strongly bundled actin filaments with decreased network formation. The model configurations illustrate a smooth gradual transition from a random individual filaments to distinct spanning networks to a system with appreciable bundled filaments with the largest PEG molecular weight of 37.4k [47].

Fixed Mass Density

We also analyze in-vitro systems of actin and PEG undergoing bundling. The experimental systems are then imaged with a confocal microscope and from those images, the degree of bundling can be extracted with the same algorithm used in Figure 3.6. By varying the PEG molecular weight and PEG concentrations, we observe that the systems

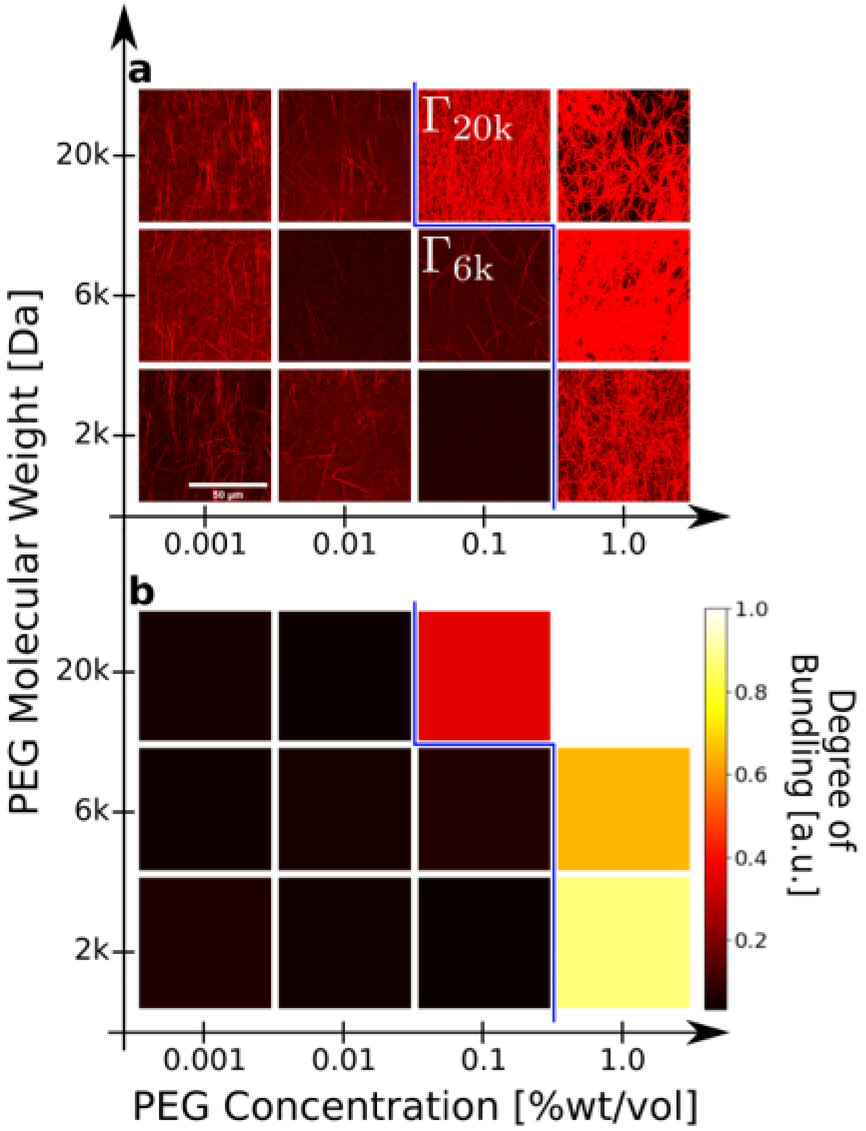

Figure 3.6: (a), Phase diagram of the experimental actin (12 μM) systems with various concentrations of PEG on the x-axis and the PEG molecular weight on the y-axis. The experimental systems are imaged with a confocal microscope. The blue line signifies the critical regions of bundling for PEG molecular weights 6k and 2k. (b), To represent the degree of bundling in each of the experimental systems, heat maps were generated from an in-house skeletonizing algorithm.

separate into 2 clear morphologies–below the blue line in Figure 3.6(a) and (b), the systems remain weakly bundled. For the lower concentrations and smaller PEG molecular weight, the actin do not form bundled structures and are in a disordered state. The area of the diagram above the blue line highlights a region of the phase space where the actin systems reach a strongly bundled regime in Figure 3.6(a).This indicates that once the PEG molecular weight is sufficently high and the a critical PEG concentration is reached, the actin filaments start to form bundled network structures. These qualitative results are reinforced by heatmap depicting the degree of bundling in Figure 3.6(b).

The PEG have a fixed mass density in experimental systems depicted in Figure 3.6. For the simulations, the PEG particles vary in mass density but have a fixed number density. To provide a better clearer insight on the effects of increasing PEG molecular weight with a fixed mass, we simulate cases where the PEG concentration has a fixed mass density, instead. We choose a reference system size of 6,000 PEG particles and a PEG radius of 0.5σ, which corresponds on the phase diagram in Figure 3.5(a) to a PEG-to-actin radius ratio of 1.0 and a PEG-to-actin number density of 1.50. We then increase the PEG radius and adjust the PEG concentration to keep the mass density fixed, according to Flory theory proportion of the radius of gyration and molecular weight.

We then explore 3 systems with a fixed PEG density: $r_1 = 0.5\sigma$ and 6,000 PEG particles, $r_2 = 1.0\sigma$ and 1,890 PEG particles, and $r_3 = 2.5\sigma$ and 410 PEG particles. We generate system configurations over early time at $t = 100$ and $t = 1000$ to examine the phase transitions of the actin filaments.

In Figure 3.7, at $t = 100$, each of the systems has a high degree of actin bundling, with thicker bundles as the PEG radius of gyration increases. However at the later time frame $t = 1000$, the actin transitions to a regime where there is little to no bundling. This transition from bundled to un-bundled is not observed in experiments as the experimental systems stay bundled over time as the actin filaments experience electrostatic and van der Waals interactions [47, 51]. In simulations, the actin-actin attractive interaction strength being scaled by 0.3, which means that once the bundles form, there is only a weak attractive interaction that is not sufficiently high enough to preserve the bundled actin structures which leads to those disordered states in Figure 3.7. The PEG are likely acting as a crowding agent for early times in the simulation, as the PEG have a stronger

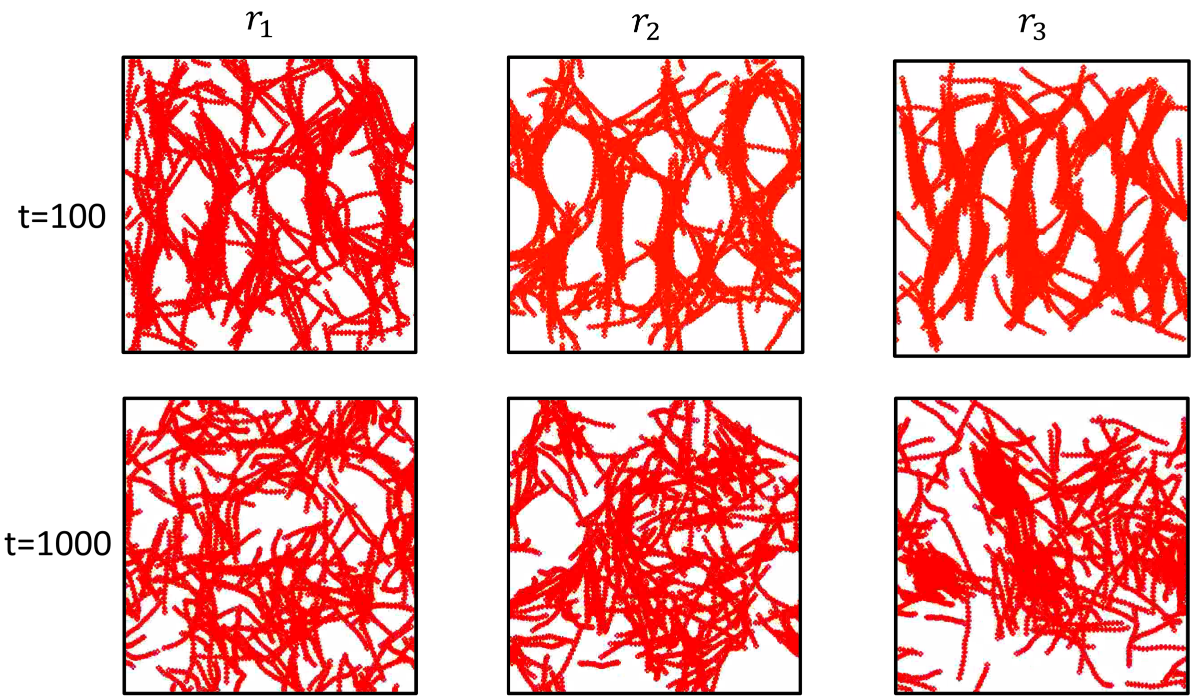

Figure 3.7: System configurations of each of the 3 radii ranging from 0.5σ to 2.5σ at $t = 100$ and $t = 1000$

homotypic attractive interaction. Once the PEG tightly clump and form clusters, the actin begin to transition out of their bundles and start to crowd the PEG, instead. Because of this discrepancy between simulations and experiments, we decide to focus on the system during the intervals when the depletion interactions are the strongest.

A way to characterize the strength of depletion interactions is by calculating the mesh size of the actin structures. The experimentalists have an in-house Python algorithm for measuring the mesh size; they track the mesh size over time for each of the 3 cases to determine which time frames yielded the maximum mesh size. The smallest PEG radius r_1, yields a maximum mesh size around $t = 30$, the PEG radius r_2 leads to a peak mesh size at $t = 50$, and the system with the largest PEG radius r_3 reaches its maximum mesh size at $t = 150$. We measure the mesh size of each of the 3 cases at their corresponding specific time-points explore how the increase in PEG radius impacts the maximum mesh size of the actin network.

We plot the mesh size results in Figure 3.8 and include system configuration insets

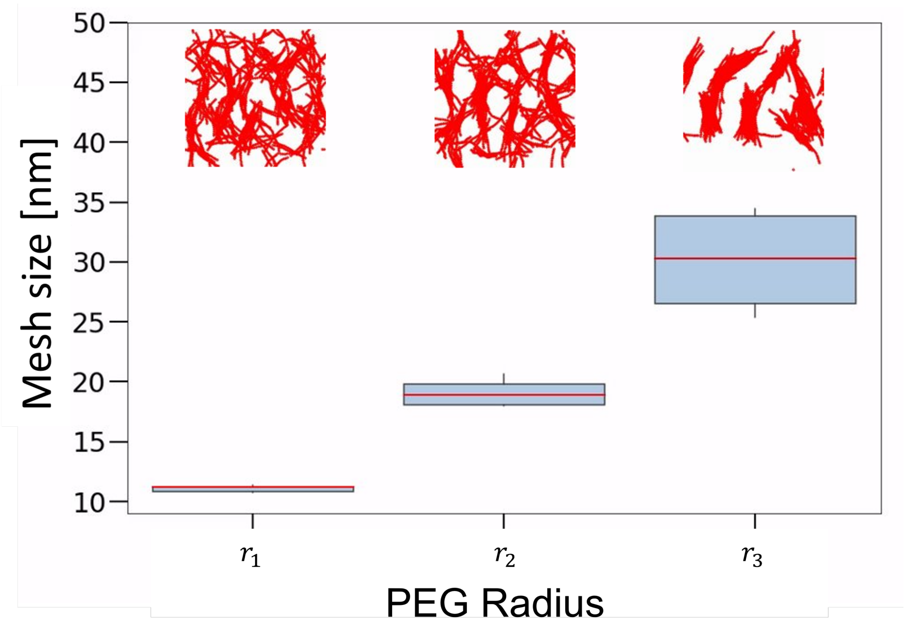

Figure 3.8: Mesh size of the actin system for $r_1 = 0.5\sigma$ at $t = 30$, $r_2 = 1.0\sigma$ at $t = 50$, and $r_3 = 2.5\sigma$ at $t = 150$. The mesh size values were averaged over 5 replicates.

along the upper half to show what the systems look like at their respective time-frames. The mesh size of the actin network increases along with the PEG radius. This suggests that even though the mass density of the PEG concentrations are fixed, the molecular weight is an effective way to tune the size of the actin bundles. For the smallest radius $r_1 = 0.5\sigma$, the mesh size average is around 11nm. This is expected since there is evident bundling occurring in the system, but the actin bundles are not as tightly bundled compared to the system cases with larger PEG radii. Instead, small gaps are present in the bundling structures, which leads to smaller mesh size values, bringing down the overall average mesh size. When the PEG radius is increased from 0.5 to 1.0σ, the average mesh size is around 19nm, nearly double that of the mesh size for r_1. We see that in the corresponding system configuration, the bundles are tighter with fewer gaps within each stack of actin filaments, which contributes to the higher mesh size value. For the largest radius r_3, the actin filaments are tightly bundled, with large stacks being formed, rather than a network-like morphology that is present in the systems for the lower radii values r_1 and r_2. The average mesh size value is around 30nm and the respective system configuration reinforces this mesh size as there are minimal gaps visible within the actin bundles. By varying the PEG radius while keeping the mass density fixed, we produce systems of actin morphologies with larger bundles as the PEG radius increases. The simulation trends for fixed mass show qualitative agreement with the scaling arguments for fixed mass density for the Asakura-Oosawa (Figure 3.3 and 3.4). The simulations suggest that maximal depletion force increasing with PEG size persists even when $q = 1$ or slightly larger than 1 in systems where the total mass is held fixed. This qualitative trend is also reflected in the experimental systems (Figure 3.6), where the degree of bundling increases along with the PEG molecular weight.

Contrastingly, the respective experimental results in Figure 3.6 indicate more abrupt transitions between the different structural phases than in the simulation configurations [47]. This is presumably a consequence of finite size effects; while the simulation study consists of 200 actin filaments, the experimental study systems have 10000 actin filaments. Furthermore, for computational simplicity, the actin filaments in the simulations are assumed to be about an order of magnitude shorter than in experiments. The shorter actin filament length effectively reduces the separation between the actin and peg length-scales in the simulations compared to the experiments, potentially making the transition in simulations less sharp compared to the experiments. However, we found one difference between simulation and experiment, namely the nature of the transition between single filament, weakly bundled, and strongly bundled regimes. In the model, we observe a smooth gradient in the degree of bundling (see Figure3.5(a)), whereas in experiment the transition is much sharper.

3.1.5 Conclusion

We develop a mathematical 3D model of actin filaments immersed in a PEG-concentrated solute. Two model cases are explored: systems where the PEG number density is fixed and a systems with a fixed mass PEG density. The system configurations in both cases demonstrate that varying the molecular weight of the PEG polymers can effectively modulate actin bundling. Our results show that we can tune the actin morphology just by changing the molecular weight of PEG, while keeping the total mass of in the system constant. The trend of increased PEG molecular weight yielding strongly bundled actin is also reflected in experimental results [47]. This research enhances the current understanding of depletion interaction in crowded biomolecular environments. This is a new insight for this research field as previous studies have had to increase or decrease the mass of the solvent to tune the degree of phase separation or bundling in in-vivo biopolymer assemblies [62, 63]. Our exploration of depletion interactions where the total mass of the depletant is held fixed contributes to the application of fueled biomimetic materials that are motivated by biological living systems that can respond to stress and regulate their structural properties [64–66]. With the total mass of the depletants held fixed, our modeling efforts can provide a potential platform for engineered materials that can yield dynamic properties without the need to add additional materials or components to the system [47].

3.1.6 Future Work

The next step for this collaboration is to refine the model by increasing system size and the length of the actin filaments so the configurations from the model can be more easily compared against the images from experiments. Once the model system is more aligned with the coexisting experimental system, inputting the model configurations in the Python package for measuring the degree of bundling would help us refine the model parameters and reinforce this proof-by-concept of depletion interactions influencing the phase transitions of actin from single-filament to bundled states.

Further direction in both experiment and model studies involves incorporating external actuation, such as light, to mediate PEG activity so the actin system can smoothly and predictably cycle between strongly bundled and weakly bundled regimes. Our research will aid the design and engineering photo-responsive biotic-abiotic materials that can rearrange their structural properties, which would have **real-world** application in self-healing technologies, solar devices, and adaptive optics.

3.2 DPS and DNA

3.2.1 Background

Spatial organization and compartmentalization of various organelles and biomolecules is essential for cellular functions like mitosis, division, and motility. Many common eukaryotic organelles like mitochondria and the cell nucleus are membrane-bound, meaning that their molecular components are bound by a biological membrane. However, even in eukaryotic cells, some organelles such as the nucleolus are not membrane bound. Moreover, prokaryotic cells like bacteria do not have membrane-bound organelles and are still successfully able to compartmentalize their content. In the past decade, liquid-liquid phase separation (LLPS), an equilibrium phase separation or de-mixing of thermodynamically interacting components of a mixture of two or more liquids, has emerged as the leading paradigm to describe the containment and organization of membrane-less organelles [67–69].

A significant difference between bacteria and eukaryotic cells is that the structure, known as the nucleoid, which contains bacterial DNA, is a membrane-less organelle as opposed to the membrane-bound nucleus in eukaryotic cells [70, 71]. The nucleoid contains DNA, RNA, and various proteins but lacks the biological membrane to physically contain the various molecules [71]. The collective localization and containment of the bacterial chromosome requires continuous phase separation and dynamic self assembly. However, the established **research context** regarding LLPS as the main form of organization in DNA condensates is being re-examined and broadened as these condensates sometimes show structure and properties that are more characteristic of liquid-crystals rather than liquids. For example, recent studies have shown the nucleoid compartmentalizing and organizing DNA strands through proteins binding the molecules together, forming a liquid-crystalline structure [72]. There is increasing interest in exploring the various interactions and mechanisms that mediate protein-driven phase separation in the nucleoid, whether LLPS or involving liquid-crystalline or even crystalline phases, and how these assemblies of membrane-less organelles affect cell division and transport [70, 73–75]. My work explores these questions in starved bacterial cells.

DNA-binding proteins from starved bacterial cells (DPS) are an abundant protein naturally found in the nucleoid of the bacteria E. Coli [76, 77]. A unique characteristic of DPS is that it is one of the few bacterial proteins in the nucleoid that can bind to DNA, compacting it in a way that doesn't affect the transcription function but also minimizes damage from oxidative stress [73, 78–80]. The DPS-DNA interactions are of particular interest due to the DPS being a major protein that is induced when cells are triggered by external stress [78, 80].

Problem Statement: Characterizing the biophysical mechanisms that lead to the formation and disassociation of DPS-DNA complexes has not yet been achieved and our main **objective** is to use experimentally informed predictive modeling to advance current understanding of the DPS-DNA phase separation dynamics. Beyond the formation of the condensates, a comprehension of the underlying mechanical and structural properties of the complexes is also needed to understand just how these properties enhance the phase separation process. We seek to obtain answers and insights into these questions by developing a computational model of the DPS-DNA system that can be directly compared against concurrent experimental studies and provide a broader understanding of the biophysics of such protein-induced phase separation and organization of membrane-less organelles. With the combination of phenomenological modeling and experimental studies, we expect to build on the existing knowledge of these DPS-DNA condensates, which will help build a foundation for engineering antibiotics that target bacterial synthesis induced by DPS proteins or similar enzymatic activity [81, 82].

3.2.2 Model

We **approach** this research question by developing a 3D model of the DPS-DNA system to understand the phase separation and organization of the DNA chains when interacting with the DPS proteins. The system has 6 DNA chains and varied concentrations of DPS particles. The DNA chains are modeled as beads on a string to help simplify the model; we estimate the diameter of the DNA beads to be 3nm, which is roughly equivalent to the distance between 6 base pairs of DNA[83]. To reduce computational expense and time, we limit the strands to be 500 beads long, translating to a length of 1.5 μm, which is considerably shorter than the in-vitro DNA lengths of 15 μm, but still long enough to provide qualitative predictions for the DPS-DNA solutions. We implement a hard-wall repulsive interaction to prevent the DNA strands from winding around the simulation box. The DPS proteins are active components in the system and are modeled as colloid particles, with a diameter of 9 nm, which is 3 times larger than the diameter of the DNA beads, a ratio reflected in experiments [83, 84].

An overdamped Langevin equation describes the translational motion of a single bead a in a strand:

$$\frac{d\mathbf{r_a}}{dt} = \frac{D}{k_B T}\left(\mathbf{F}_{LJ_i} + \mathbf{F}_{LJ_j} + \mathbf{F}_{LJ_k}\right) + \frac{D}{k_B T}\left(\mathbf{F}_{s,i} + \mathbf{F}_{b,i}\right) + \sqrt{2D}\eta \tag{3.7}$$

The diffusion constant, Boltzmann constant and temperature are described by D, k_b, and T, respectively. We scale our simulation length in units of DNA bead diameter $\sigma = 3$nm. Our timescale is scaled by $\tau = 0.3\mu$s, which is the time it takes for a single DNA bead to diffuse its diameter; the estimated diffusion coefficient is based on previous literature and theory [85, 86]. The forces $\mathbf{F}_{LJ_i}$ and $\mathbf{F}_{LJ_j}$ describe the Lennard Jones pairwise interaction forces between the beads. Index i represents intra-strand pairwise interactions,index j represents bead-to-bead interactions between two separate DNA strands, and index k denotes the interaction force between a DNA bead and a DPS particle. The Lennard

Jones potential is given below,

$$V_{LJ} = 4\epsilon \left[\left(\frac{\sigma_{ij}}{r_{ij}} \right)^{12} - \left(\frac{\sigma_{ij}}{r_{ij}} \right)^{6} \right], \tag{3.8}$$

where r_{ij} denotes the inter-bead distance between beads i and j, ϵ represents the strength of the potential, and σ_{ij} is the average diameter of bead i and bead j.

Stretching and bending can occur within strands and $U_s = \frac{K_s}{2}(l - l_0)^2$ and $U_\theta = \frac{\alpha_B}{2}(\theta - \theta_0)^2$ represent the respective stretching and bending potentials. In the following above equations, α_S is the extensional stiffness coefficient and is set to 544, l denotes the distance between the two sequential beads in a strand, and l_0 is the equilibrium rest-length between two beads on the strand and is set to the bead diameter. The bending rigidity is $\alpha_B = 25$ and the angle between two beads is represented by θ and we set the equilibrium angle θ_0 to π. The last term $\sqrt{2D}\eta$ introduces thermal noise into the system. We also use a similar overdamped Langevin equation to describe the translational motion of a DPS bead b:

$$\frac{d\mathbf{r_b}}{dt} = \frac{D}{k_B T} \left(\mathbf{F}_{LJ_l} + \mathbf{F}_{LJ_m} \right) + \sqrt{2D}\eta \tag{3.9}$$

The index l denotes interparticle interactions between DPS beads and m represents interparticle interactions between DPS and DNA beads; similar to the DNA dynamics, we implement a Lennard-Jones 12-6 potential from which the interparticle interaction forces are derived.

For the Lennard-Jones pairwise homogeneous (specifically DNA-DNA or DPS-DPS) interactions, we set the range to be repulsive only, effectively making it a Weeks-Chandler-Anderson interaction potential. For heterogeneous interactions, DNA beads interacting with DPS beads, we allow both short-range repulsive and long-range attractive interactions. Because the experiments have various concentrations of NaCl and crowding agents–such as PEG–we tune ϵ for attractive interactions to phenomenologically represent the effects of NaCl and PEG in the system. We vary ϵ from a range of 0 to 2.0, to explore systems where DPS and DNA do not bind or interact and when the two components experience a large attractive strength of interactions. Another quantity we explore is the concentration of DPS particles. We do so by varying the number of DPS beads to 100 to 3000.

At the beginning of the simulation, we initialize DNA strands in the box and allow them to equilibrate for $t = 1000$. Then, we populate the simulation box with DPS particles and run the simulations for up to $4000t$.

3.2.3 Results and Discussion

To qualitatively examine how the concentration of DPS and attractive interaction strength tune the spatial organization of the system, we generate a phase diagram of 2D-projected simulation configurations in Figure 3.9. The DNA strands are colored in red and the DPS particles are in green. The number of DPS, represented by N_d ranges from 100 to 3000 and the heterotypic attractive strength is tuned by the parameter ϵ_{hetero}. For the system with 100 DPS, the smallest DPS concentration, the DNA strands do not become condensed into a cluster and remain in a disordered state. Even as the ϵ_{hetero} parameter is increased, the DPS do form into very small clusters and clump near the DNA strands, the DPS concentration is still too small to lead to DNA compaction. For $\epsilon_{hetero} = 0$ and 0.1, across all 4 concentrations of DPS, the DNA strands remain in a disordered randomized state with no condensate formation. This demonstrates that even for systems with higher concentrations of DPS, the heterotypic interactions are still too weak to mimic the DPS binding interactions observed in experiments.

However, we do see a qualitative shift in the phase diagram in the DPS as N_d ranges from 1000 to 3000 and ϵ_{hetero} ranges from 1.0 to 2.0. DNA strands begin to experience compaction as DPS begin to form clusters within the DNA regions as the DPS concentration and ϵ_{hetero} are increased. Each of the systems appears to reach a non-equilibrium steady state. Regions of the box have uneven concentrations of DPS; the local DNA regions tend to have fewer isolated DPS particles while areas without DNA have a higher local concentration of DPS. Once all the DPS within close proximity of the DNA get pulled

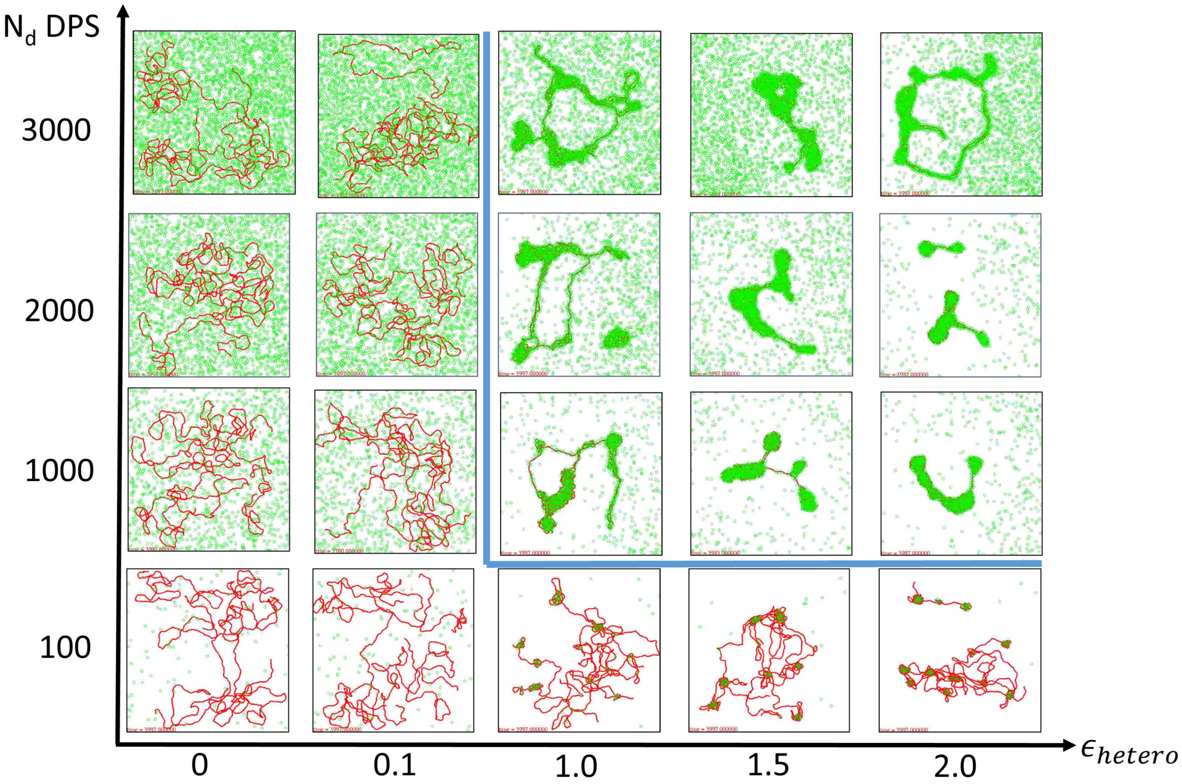

Figure 3.9: Phase diagram of the simulation configurations sampled at $t = 4000$. The number of DPS (N_d) is represented on the y-axis and ϵ_{heter} represents the strength of heterotypic attractive interactions is on the x-axis. The DNA strands are visualized first (in red) and the DPS particles are drawn in next (in green). Within the phase diagram, we see a qualitative separation (blue line) occur when N_d is 1000 or more and ϵ_{hetero} ranges from 1.0 to 2.0.

into a cluster, the remaining DPS that are further away from the DNA regions tend to stay in their local regions there as the attractive interactions are not strong enough to overcome the longer distances.

To explore the degree of translational order in the systems, we sampled the radial distribution function (RDF) at $t = 4000$ for the systems where condensate formation was present (blue line in Figure 3.9). As the attractive strength of heterotypic interactions increases, more peaks in the RDF curves for each DPS concentration and the heights and sharpness of those peaks increase as well. These trends are indicative of systems with higher degrees of translation order, which agree with the corresponding phase diagram snapshots showing the systems reaching those condensate structures. For each of the

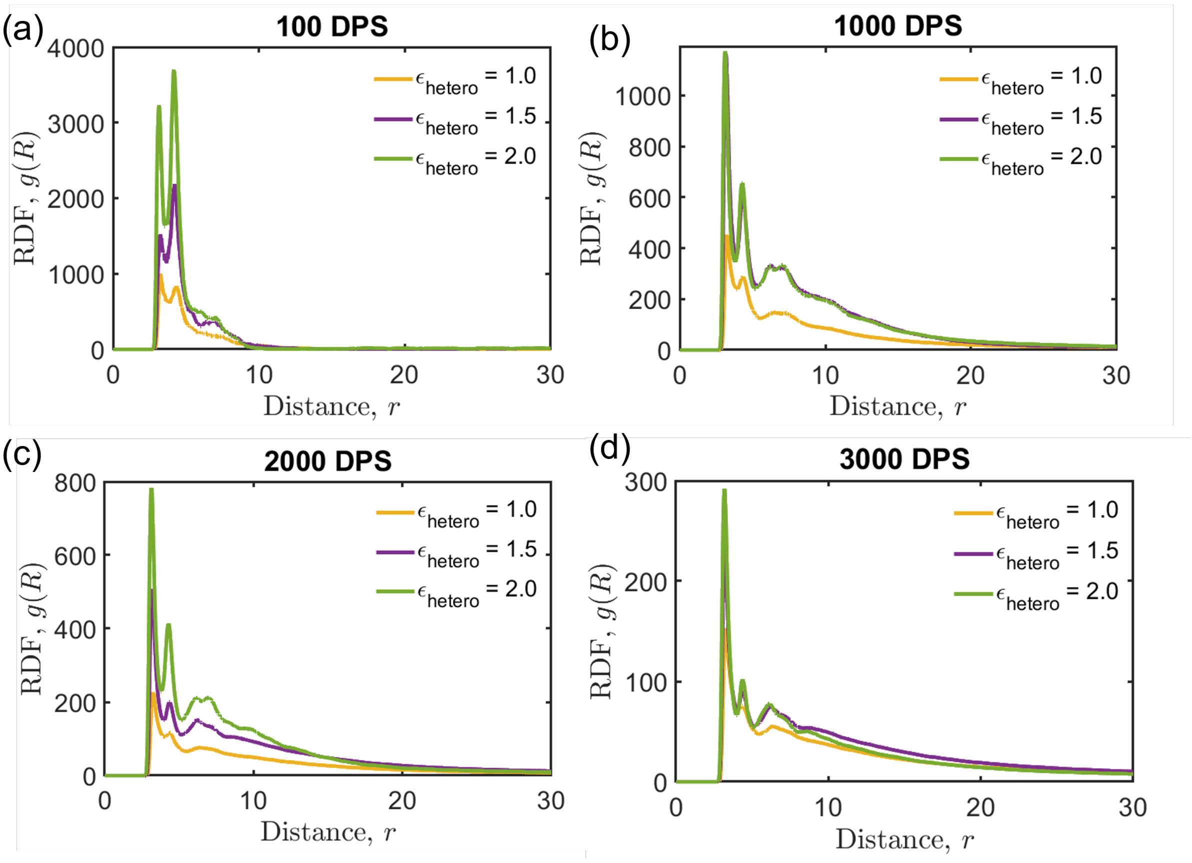

Figure 3.10: The RDF is sampled for all 20 cases at the final time-frame $t = 4000$. The radial distance r is scaled in units of the DNA bead diameter. For each case, we run 5 replicates and then average the RDF data for systems with (a) 100, (b) 1000, (c) 2000, and (d) 3000 DPS

ϵ_{hetero} values, the peak values for $g(R)$ decrease as the DPS concentration increases. This is because the systems with lower DPS concentrations produce systems with a large majority of DPS particles forming small clusters as they interact with the DNA strands over time. Because a large fraction of the DPS particles become locked into clusters within the DNA-occupied regions, this leads to higher $g(R)$ peak values for short distances r. The heights of the peaks in the RDF curves for the higher DPS concentrations decrease due to a larger normalization factor in the denominator. The system snapshots in Figure 3.9 show that while a considerable fraction of the DPS form compacted condensates with the DNA, there is still a large proportion of DPS that remain in a disordered state with no cluster formation due to sufficient distance between them and the DNA-occupied regions.

To gain insight on the compacted-ness and spread size of the condensates, we extract from the RDF data the full width tenth maximum (FWTM). This is obtained by finding the value of the maximum peak in each RDF curve and then For our simulations, the FWTM is the width of the RDF at a level that is 1/10 the value of the maximum peak. We measured the FWTM for the systems that experienced condensate formation (the regions sectioned off by blue line in Figure 3.9).

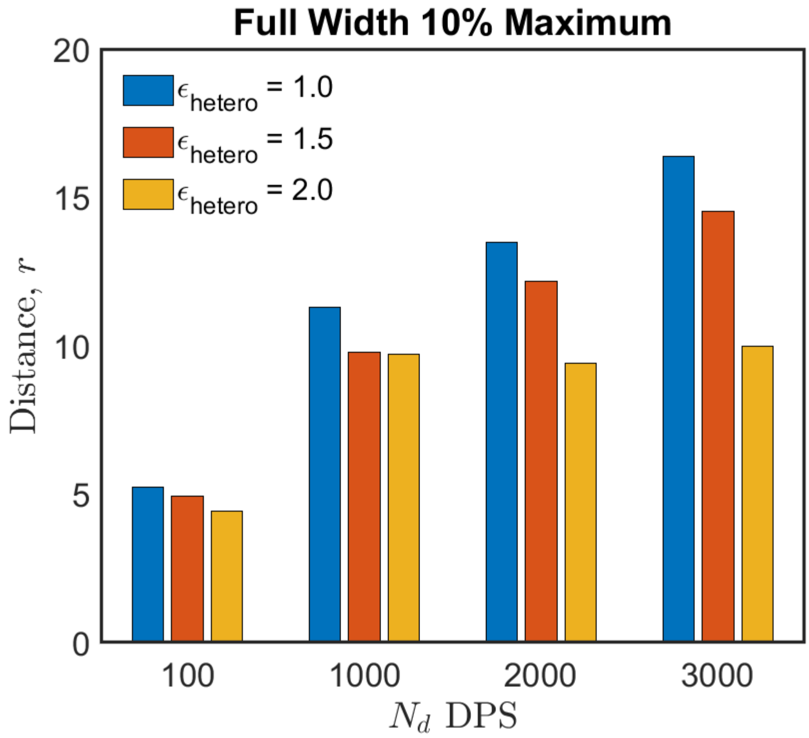

Figure 3.11: The full width tenth maximum (FWTM) values for the simulation cases with condensate formation. The x-axis represents each DPS concentration and the radial distance is given be r, which is units of the diameter of a DNA bead.

From Figure 3.11, the FWTM values suggest the cluster size increases as the DPS concentration increases, which is expected as there are more DPS particles available to interact with the DNA and form condensates. For the smallest concentration of DPS, the FWTM demonstrates that the spread size of the DPS clusters decreases slightly as the attractive interaction strength increases. This indicates that the clusters aren't necessarily smaller in numbers (as evidenced by the configurations in Figure 3.9 but are more tightly compacted because of the higher attractive interaction strength. The decrease in the FWTM is more distinct for higher DPS concentrations; the difference between the FWTM for ϵ_{hetero}=1.0 and 2.0 increases. Higher DPS concentrations lead to more DPS particles interacting with the DNA strands. This greater interaction leads to more compact clusters, and this is more clearly seen for larger system sizes ranging from 1000-3000 DPS particles.

3.2.4 Conclusion

We develop a 3D microscopic model of DNA in a solution of DPS proteins. We show that the condensate formation of DPS-DNA structures can be tuned by the concentration of DPS and the strength of interactions between DNA and DPS. This is particularly insightful as the attractive interaction parameter can be used to phenemenologically represent the various concentrations of salt and PEG that are implemented in experiments to mimic the crowded environment of bacterial cells. When the attractive interactions are scaled down by factors of 0.1 and below, we observe little to no condensate formation regardless of the concentration levels of DPS. For higher DPS concentrations and moderate to high attractive interaction strengths, we produce systems that can undergo condensate formation. And within the systems with higher attractive interactions, those lead to more tightly compacted clusters of DPS-DNA, which lead to higher structural and translational order in those localized regions of condensation.

3.2.5 Future Work

The next steps include comparing the conditions and parameters to ensure it is aligning well with the current experiments. With this 3D model, we will be able to understand the mechanisms of this unique condensate by determining the degree of orientational order of the DNA chains. We may use measurements like the nematic order parameter to measure the alignment of the system at different time points. These results from our agent-based model may be comparable against nematic ordering results from a continuum model of the DPS-DNA environment and will allow us to evaluate whether the system reaches a liquid-crystalline structure or remains in a disordered liquid state.

To understand how the collective transport properties are affected by the DPS-DNA interactions, tracer particles can be added in experiments, placing them within, between, and outside of condensate regions to measure the mean square displacement (MSD). We can also extract MSD trajectories since the particle coordinates for both DPS and DNA can be recorded for simulations. The MSD trajectories of the DPS regions and DPS-DNA complexes can then be compared directly against single-particle tracking results from experiments. The rates of diffusion derived from the MSD curves will indicate when the system has reached a compacted, ordered state (if the rate is sub-diffusive) and the curves will also allow us to quantify the varying levels of collective movement of the DPS proteins and DNA strands at different lagtimes.

Chapter 4

Collective Mechanics and Dynamics of Engineered Cytoskeletal Composites of Two Different Types of Biopolymers and Motor Protein

4.1 Background

The cytoskeleton is an extremely dynamic network. It is responsible for generating mechanical forces within the cell, determining cell shape, and mediating cell mobility. Cytoskeletal networks themselves are quite complex. The main components of the cytoskeleton are the biopolymers actin filaments and microtubules, and their associated motor proteins and crosslinkers. Actin filaments are semiflexible and microtubules are more like rigid fibers on the scale of a cell and are approximately three orders of magnitude stiffer than actin filaments. The actin filaments play a critical role in cell mechanical response and their lower bending rigidity allows the cytoskeleton to remodel and respond to external mechanical forces and facilitate variability in cell shape to avoid deformation of the composite network [87–89]. The microtubule network facilitates long-range force transmission, and allows the cell to maintain mechanical memory of its structural integrity and stiffen under small amounts of mechanical stress [88, 90]. The structure, shape, and collective motion of the filamentous network can be modulated by molecular motors and crosslinking proteins. Myosin and kinesin are two main types of motor proteins found in eukaryotic cells that are essential to cytoskeletal functions, such as cell division, motility, and internal organization within the cytoplasm [91]. The myosin motors are mainly associated with actin filaments and aid cell contraction and movement [39, 92, 93]. Kinesin interacts with the microtubules, aiding intracellular transport and formation of microtubule networks [94–96].

Previous experimental and simulation studies have characterized how actin filaments and microtubules aid the cytoskeleton [97, 98]. The current **research context** in cytoskeletal networks indicates an established preference to treat the actin- and microtubule-based systems as individual, separated networks. Many in-vitro experimental and theory studies have focused on actomyosin networks to make predictions about their active mechanics and contraction and shown how the sliding mechanism of the myosin leads to actin network contractility [99–102]. Active cytoskeletal materials made of microtubule and kinesin have also been well studied [103–105] and provided a platform for new discoveries in the area of active nematics (See papers by Dogic + Baskaran + Marchetti et al). Most studies have not looked at composite systems of actomyosin and microtubule-kinesin networks, and without the understanding the impact of their interplay, a full picture of the cytoskeletal networks and their mechanical structure-function properties remains incomplete.

In cells these two biopolymer networks usually do not act independent of each other, they interact to regulate various cell functions [106–110]. **Problem Statement:** While there is emerging interest in studying the actin-microtubule interactions, modeling the complex physical interactions between actin and microtubules and their associated motor proteins is still not as well characterized and their collective properties are not well understood [90, 111]. Working alongside experimentalists studying these dynamic actin-microtubule composite networks, we aim to develop a robust, agent-based model that can provide insights into the dynamic relationship between motor proteins and actin and microtubule composites. Our main **objective** is understanding the mechanisms that underlie the emergent structure patterns, mechanics, and dynamics the actin-microtubule-motors model network. This will allow us to directly compare results with experimental observations and improve and fine-tune the models to provide accurate predictions on the what kinds of mechanisms arise in certain areas of the parameter space and what factors drive these unique biological processes. The modeling and experimental of these autonomous biotic-abiotic systems will serve as a foundation for **real-world** application in self-regulated soft robotics, artificial muscle tissue, and self-assembled micro-electronic devices [112–115].

4.1.1 Model

Our **approach** is to construct a 3D model network consisting of actin and microtubule filaments. Both the actin and microtubule are modeled as beaded chains. The diameter for both sets of filaments is set to 200nm. The actin filaments have a uniform length of 8μm, which is equivalent to 40 beads per chain and the microtubule composites have a shorter length of 4μm, which is 20 beads per chain in the simulations. To mimic the dense cytoskeletal network composites from experimental studies, we simulate 450 actin strands and 300 microtubule strands. We incorporate 3 types of proteins: myosin, kinesin, and passive crosslinkers to drive the various network formations.

An overdamped Langevin equation is used to model the translational motion of a single bead in strand i of an actin or microtubule:

$$\begin{aligned}\frac{d\mathbf{r}}{dt} = \frac{D}{k_BT}\left(\sum \mathbf{F}_{LJ_{ij}} + \sum \mathbf{F}_{LJ_{ik}}\right) \\ + \frac{D}{k_BT}\left(\sum \mathbf{F}_{p_{ik}} + \sum \mathbf{F}_{c_{ik}} + \sum \mathbf{F}_{s_{ij}} + \sum \mathbf{F}_{b_{ij}}\right) + \sqrt{2D}\eta \quad (4.1)\end{aligned}$$

The interparticle interaction forces are represented by $\mathbf{F}_{LJ_{ij}}$ and $\mathbf{F}_{LJ_{jk}}$, where indice pair ij denotes inter-bead interactions within the same strand and ik describes inter-bead interactions between different strands. These pairwise interactions are governed by a truncated 12-6 Lennard Jones potential given by,

$$V_{LJ} = 4\epsilon \left[\left(\frac{\sigma}{r_{ab}} \right)^{12} - \left(\frac{\sigma}{r_{ab}} \right)^{6} \right], \tag{4.2}$$

where the distance between beads a and b is denoted by r_{ab}, σ represents the bead diameter, and ϵ is the well depth of the potential.

When a motor binds two filaments together, we model this interaction with the motor protein as a spring force $F_{p_{ik}} = -K_p(r_{ij} - r_0)$ between the two filament beads, where K_p denotes the spring coefficient of the motor protein, the interparticle distance is denoted by r_{ij}, and the rest length is given by r_0. The two filament beads must be within the rest length r_0 in order to trigger the probability of a molecular motor binding the two filaments together. When myosin binds two actin filaments together, only a contractile force is exerted from the spring. However, for kinesin-microtubule interactions, the kinesin can exert a contractile and extensile forces between the two beads. To mirror the experimental conditions, the concentration ratios of myosin to actin is 4 to 1 and the kinesin to microtubule concentration ratio is 50 to 1 in the simulations.

Currently, the probabilities of attachment and detachment of the motor proteins are set to be equivalent to simplify the model. The motor proteins can bind filaments together based on an exponential probability rate,

$$P_a = c_m \left(1 - e^{-k_{On} t} \right) \tag{4.3}$$

where c_m describes the concentration of free motor proteins in the system and k_{On} denotes the experimental binding rate of myosin [38]. For motor proteins to detach, we implement a similar exponential probability function,

$$P_d = \left(1 - e^{-k_{Off}t}\right) \tag{4.4}$$

where this time the unbinding rate k_{Off} is derived from a dynamic formula,

$$k_{Off} = 10\left(\gamma_c e^{F * x_C / k_B T} + \gamma_s e^{F x_S / k_B T}\right) \tag{4.5}$$

where γ_c and γ_s represent the prefactors determining the catch and slip dynamics of the motor proteins, $F = -k_{bridge}(r_{ij} - r_0)$ represents the spring force from the connected motor protein with k_{bridge} denoting the cross-bridge stiffness of the motors, and x_C and x_S are the experimental bond lengths of the motors [38, 116].

We also consider the addition of passive crosslinkers in the actin-microtubule network and model these crosslinks as Hookean springs, too; $\mathbf{F}_{c_{ik}} = -K(r_{ij} - r_0)$ represents the crosslinker spring force, where K describes the crosslinker spring constant and r_0 is the rest length that the two filament beads must be from each other in order for a crosslink to occur. For every simulation, the crosslinkers will link to only one set of the filaments-actin or microtubules; the ratio of crosslinkers to filaments is 80 to 1. They have a constant probability of attachment $p_0 = 0.005$ and once they are crosslinked between two filament beads, they stay attached unless overstretched. The last term $\sqrt{2D}\eta$ represents the thermal noise in the system.

The actin and microtubule filaments can also experience stretching and bending; the corresponding potentials for the forces $\mathbf{F}_{s_{ij}}$ and $\mathbf{F}_{b_{ij}}$ are $U_s = \frac{\alpha_S}{2}(l - l_0)^2$ and $U_\theta = \frac{\alpha_B}{2}(\theta - \theta_0)^2$, the stretching and bending deformation energies. The extensional stiffness coefficient and bending stiffness coefficient are given by α_S and α_B, respectively. For actin, $\alpha_S = 10$ and $\alpha_B = 4$ and for microtubules, $\alpha_S = 100$ and $\alpha_B = 100$. The length and angle between the two consecutive beads is denoted by l and θ and the equilibrium length and angle are denoted by l_0 and θ_0. To closely align with experimental conditions and observations, the bending and extensional stiffness of actin is set to be two orders of magnitude lower than that of the microtubules.

4.1.2 Actin-Microtubule Composites Configurations

We simulate an actin-microtubule model network and sampled system configurations at 6 time points to analyze the transitions in the structure. In this system, crosslinking proteins and myosin are able to bind to the actin. For the microtubule channel, kinesin is present in the system. When we initialize the system with actin and microtubules, nothing is connected. At the first timeframe t=10, you can see that the myosin begin to attach to actin and the actin also become crosslinked to form a network via the crosslinkers. The actin filaments form a network of actin bundles. Contrastingly, in the microtubule channel, the filaments start to get connected by the kinesin motors but they do not form networks over time. The microtubules are being bound by kinesin but form clumps of filaments rather than a mesh-like network as seen in Fig. 4.1. Another observation for this framework is that global contraction or extensile behavior isn't observed in this system.

The current steps for this model include identifying separate parameter values related to the kinesin attachment dynamics and types of forces the proteins exert on the microtubules; rather than model the kinesin as Hookean springs, another avenue of interest is encoding these motor-filament interaction forces as force dipoles, to effectively model the extensile and contractile behavior seen in kinesin-microtubule structures.

4.1.3 Characterizing simulation videos

An overarching goal of this research collaboration is to characterize different properties like stress propagation and stiffness. These collective properties are of interest because the cytoskeletal networks can have contractile network dynamics. Due to the low rigidity of actin, when the myosin motors bind actin filaments together and begin to assemble into bundles, these bundled structures undergo contraction [117]. Because of the muscle-

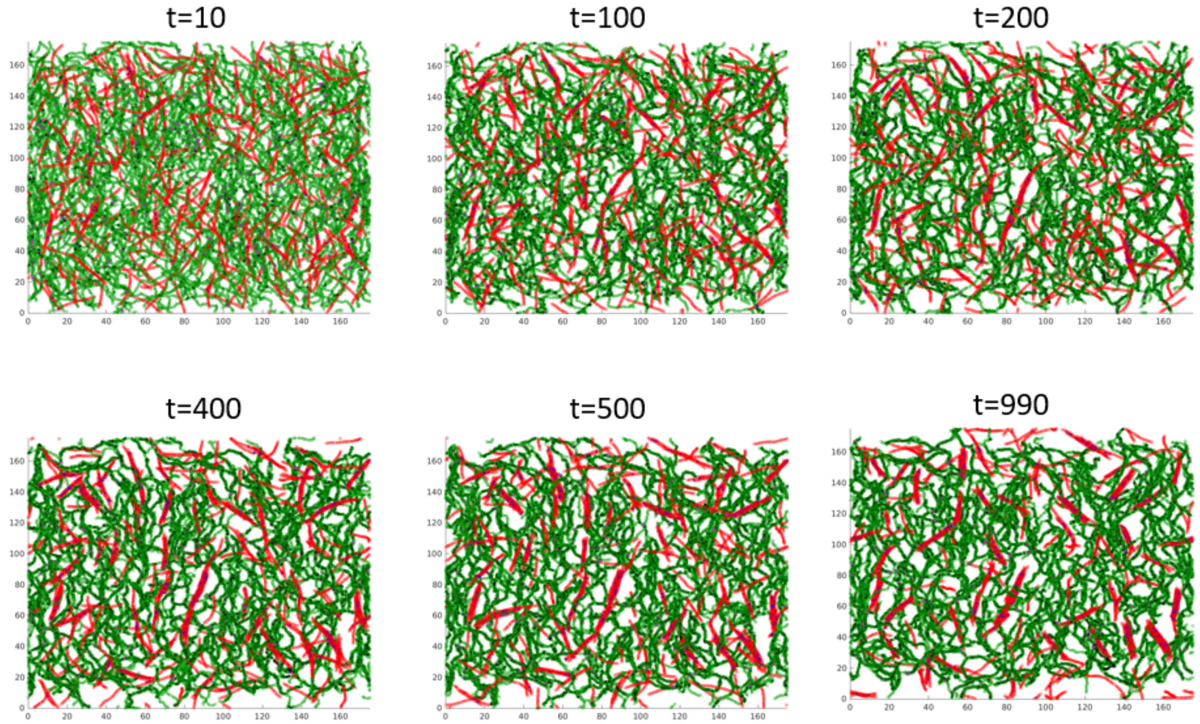

Figure 4.1: Preliminary system configurations of the model actin-microtubule network sampled at 6 time frames: $t = 10, 100, 200, 400, 500, 990$. Within this system, kinesin (blue) is binding microtubules (red strands), myosin (purple) binding actin (green strands) filaments and passive crosslinking proteins (black) have been encoded for additional actin-actin interactions.

like activity that results from myosin binding to actin, experimental studies by Gardel et al. show that once a critical density of myosin is reached, the composite network experiences large-scale contraction [118]. Modeling efforts by MacKintosh et al. have also demonstrated how the myosin binding activity leads to an increase in bulk elastic moduli of the filamentous network and that the unbinding dynamics of the myosin governs the timescale of force fluctuations in the system [119]. The microtubule channel is also capable of exhibiting contractile dynamics with the help of kinesin motors. Kinesin has a high-duty ratio compared to myosin II, the specific myosin motors used in our collaborators' experiments. This means the kinesin motors stay attached to the microtubules for significantly longer [120, 121]. Kinesin have the ability to walk along microtubule filaments. Microtubules have polarized (+/-) ends and kinesin have a tendency to walk towards the polymerized (+) ends of the filaments [122]. Then, the microtubules will begin to form aster or spindle-like structures due to kinesin binding the microtubules together and clustering towards the (+) ends of the strands [55, 123]. The formation of these asters also generates contractile forces in the network. A model study conducted by Kruse et al. demonstrated that a system of polar filaments undergoing bundling via molecular motors can still contract regardless of the degree of spatial organization [124].

Extensile behavior can also be generated in the cytoskeletal network. In systems where there is either a sufficient concentration of static crosslinkers or depletants like PEG that aid in the bundling of microtubules, extensile behavior can arise if microtubule bundles in close proximity are oriented in such a way that their adjacent ends have opposite polarity [55, 125]. The kinesin motors will still walk towards the respective (+) ends of the pair of bundles, which causes the microtubule bundles to slide apart in opposing directions, resulting in bundle extension [55]. Najma et al. present a joint experiment/theory investigation of microtubules, depletants, and kinesin motors to determine how the kinesin binding kinetics, the different component concentrations, and polar alignment interactions drive the extensile and contractile behavior [126]. Experimental systems with depletants and crosslinkers are able to produce extensile forces and by varying the concentration ratios of the different model components, they can generate systems that transition from bundle-like structures that can experience extension to asters with contractile behavior [126].

With our current simulations, we have cytoskeletal composites with filaments, motors, and crosslinkers. A goal with the simulations is to be able to produce a self-assembled structure that can have a network of filaments, bundles, networks of bundles, and asters. With these dynamic structures, we aim to explore how we can generate contractile and extensile behavior. Two avenues of this research question have to be addressed: how to develop a simulation that can exhibit these kinds of properties and how to use the data from simulations to study large scale contraction and aster formation.

The strategy of using simplified models with fewer parameter combinations to describe dynamic properties and emergent mechanisms has been successfully implemented in areas of active matter and materials research [127–129]. In a computational study of motor activity in a cell nucleus, Saintillan et al. implement a coarse-grained model by modeling chromatin as a polymer chain and use force dipoles to characterize molecular motor interactions in the system [128]. Ronceray et al. also use force dipoles to mimic the molecular motor proteins in fiber networks in order to study the force propagation in cytoskeletal composites [129].

We implement a similar approach for our 6-component model of actin, microtubules, myosin, kinesin, and 2 types of crosslinkers. Our goal is to downselect from this large parameter space to a set of 150 filaments that have a uniform length of 40σ and passive crosslinkers. Each system will have only one kind of filaments as well, rather than the actin-microtubule composite network we have previously explored. We alter the box depth dimension to be $z = 40\sigma$, so its equivalent to the length of the filament. With this toy-model approach we implement nucleation or pinning sites to generate local contractions (asters) in the system. At the beginning of the simulation, filaments are allowed to diffuse and equilibrate for a set amount of time ($1000t$). Then, we implement crosslinking kinetics to allow the filaments to form a network. After a network had formed, then the nucleation site switches on at $1000t$, and this attractive site is characterized by an inverse potential,

$$U(r) = \frac{C(r^2 + 2R^2)}{2R^3} - \frac{C}{r} \tag{4.6}$$

where C is a term to scale the attractive strength and is set to 200, r is the distance between each endpoint of a filament and R is the radial distance of 10σ. The force from this inverse potential is only applied to the endpoints of the filaments and is represented by be the following piece-wise function:

$$|\overrightarrow{F}| = \begin{cases} \frac{C}{R^3} r, & r < R \\ \frac{C}{R}, & r \geq R \end{cases} \tag{4.7}$$

This function allows for the filament endpoints to be attracted to the nucleation sites but also appropriately scales the magnitude of the attractive force once the filaments are sufficiently close to the nucleation site (within a distance of 10σ).

We explore 2 cases of simulations for the semi-flexible actin filaments and the stiffer microtubule filaments. In one system, we have one nucleation site in the center of the simulation box to generate global contraction in the network and in a second case, we have 4 equidistant nucleation sites to produce local contraction and local aster formation. Within each of the 2 nucleation site arrangements, we implement a case with crosslinking, where every filament bead can have 1 crosslink bond and a case where there's no crosslinking occurring.

We use openGL programming to develop 2D projected system configurations. Recently, Dr. Jonathan Michel has developed a post-processing C++ program that produces pseudo-micrographs that mimic the experimental images that are obtained from a confocal microscope. We choose a z-stack height of 20 for the pseudo micrographs; the nucleation sites are all located at $z = 20$, so the global contraction and formation of asters can be clearly seen when sampling images at that height. We chose to look at the simulation after the filaments had the chance to diffuse and equilibrate. So for the times at which the snapshots were sampled, time $t = 0$ refers to time immediately after the equilibration step.

Central nucleation site with crosslinking

In Figure 4.2(a), the actin channel has formed a crosslinked network and you can see the crosslinks drawn in black. In the successive simulation snapshots, we see more instances of crosslinking and a global contraction towards the central nucleation site. In the final frame for $t = 4000$, it appears that a few filaments are winding around the box or being pulled from opposite ends; this is the effect of the reflective periodic boundary conditions in our simulation. In the psuedo micrographs (Figure 4.2(b)), the ball of actin filaments in the center is visible and the filaments located further from the nucleation site are not as bright, indicating they are in a different z-stack slice.

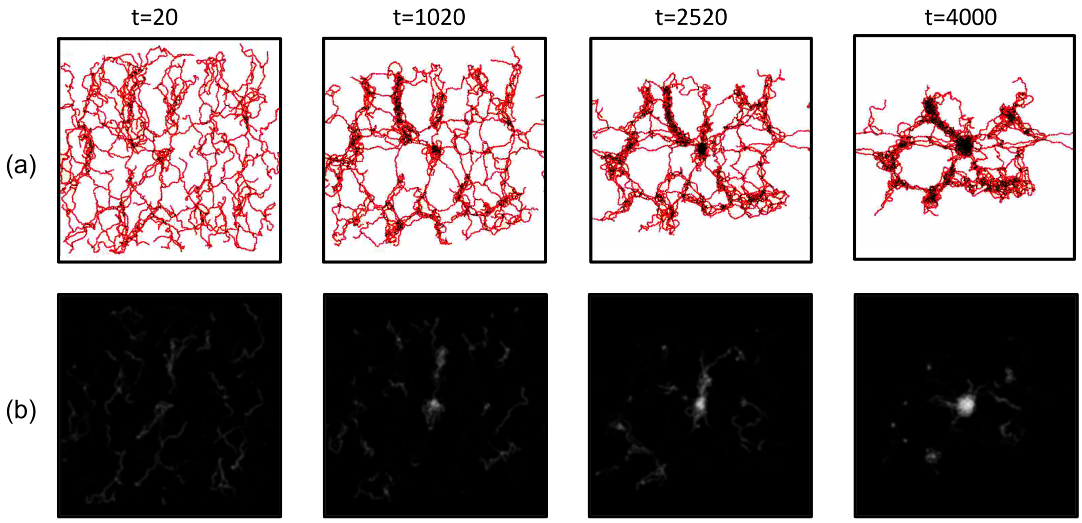

Figure 4.2: Simulation images of the actin channel sampled at 4 time frames: t = 20, 1050, 2520, 4000. (a), the system configurations of the actin network. (b), pseudo micrographs of the simulation snapshots.

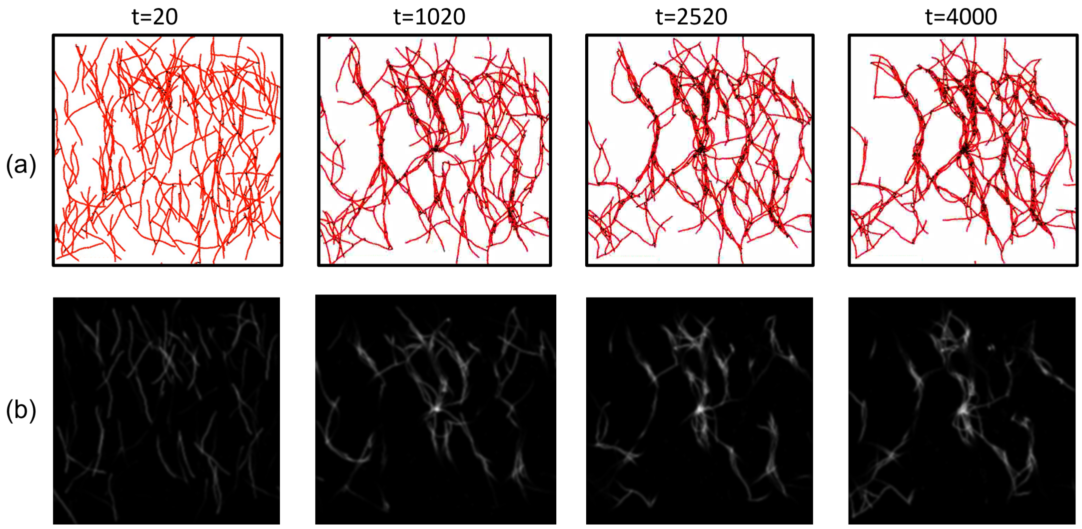

Figure 4.3: Simulation images of the microtubule channel sampled at 4 time frames: t = 20, 1050, 2520, 4000. (a), the system configurations of the microtubule network. (b), pseudo micrographs of the simulation snapshots.

We run a similar simulation but instead of actin filaments, we have a channel of stiffer filaments to mimic microtubules. In the first frame of Figure 4.3(a) and (b), crosslinking is occurring in the network but things look fairly disordered and no contraction is present since the nucleation site has not been switched on yet. Then at $t = 1020$, we start to see crosslinked bundles of microtubules and a bundled network formation emerging in the system and this is visible in both the system configuration and the corresponding micrograph. However, the system doesn't appear to change much in the later time frames $t = 2520$ and 4000; there is no global contraction present in the network and the orientation of the microtubules remains the same. The lack of contraction and aster formation in this system is likely due to the rigidity of the microtubule strands and the crosslinking. Crosslinks that bind at a fixed location will place constraints on the positions, orientations, and topology of microtubules. This in turn impairs aster formation and the flexibility of the network as crosslinked bundles form.

Central nucleation site without crosslinking

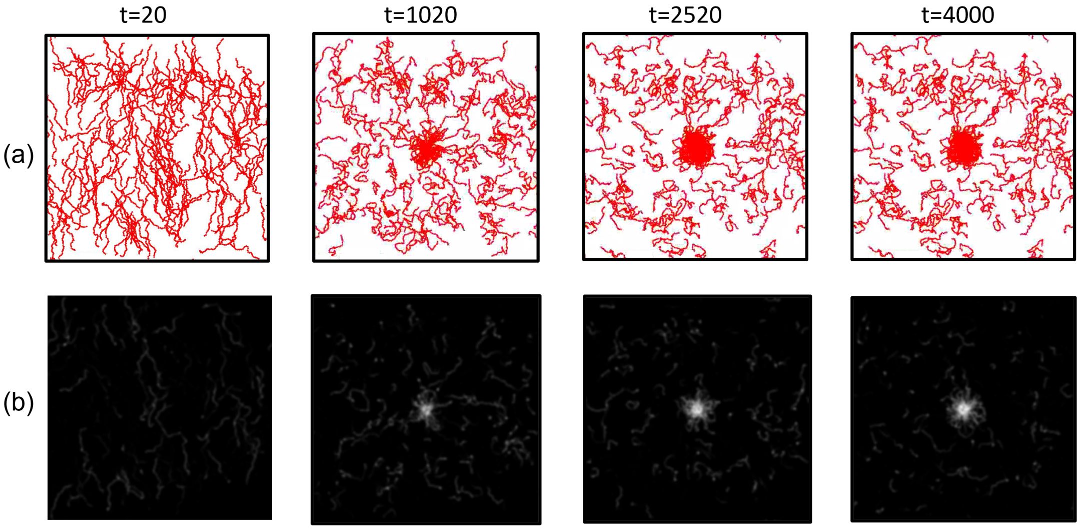

Figure 4.4: Simulation images of the actin channel with a central nucleation site sampled at 4 time frames: t = 20, 1050, 2520, 4000. (a), system configurations of the actin network. (b), pseudo micrographs of the simulation snapshots.

Next, we explore a system with a central nucleation site with the absence of crosslinkers. Figure 4.4 shows the case with actin filaments. Over time, actin strands accumulate as the endpoints experience attractive interactions with the centralized nucleation site and over time, this accumulation begins to resemble a yarn ball-like structure. This a natural effect of a low persistence length, lack of crosslinkers, and imposition of a constraint only at the central point of the box.

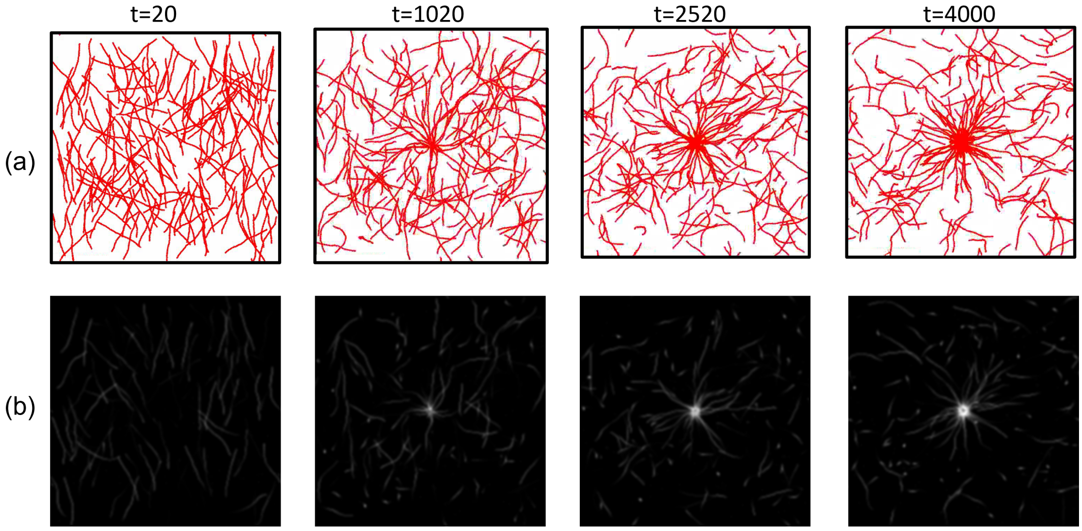

Figure 4.5: Simulation images of the microtubule channel with a central nucleation site sampled at 4 time frames: t = 20, 1050, 2520, 4000. (a), system configurations of the microtubule network. (b), pseudo micrographs of the simulation snapshots.

In Figure 4.5, we also observe the effects of a central nucleation site in a system with the absence of crosslinking for the stiffer microtubule filaments. We see a gradual aster formation at the center point of the box, which is expected since the endpoint beads of the microtubules are the only beads experiencing the attractive forces from the nucleation site and without crosslinking, the microtubules do not form bundles or networks and are able to move towards the center more easily. The aster is also clearly visualized in the micrographs as well, with the brightest point located at the nucleation site.

Multiple nucleation site with crosslinking

We then explore systems where we have 4 equidistant nucleation sites with equal attractive interaction strengths. For the actin channel with crosslinkers in Figure 4.6, we see that each of the 4 nucleation site accumulates clumps of actin over time. The strands experience a large amount of crosslinking at each of the 4 sites as well, and the balls of actin are connected by filaments that stretch diagonally, vertically and horizontally across. So by $t = 4000$, we have a square-shaped structure with the majority of the actin strands clumping at each of the nucleation sites. It also appears that there are 1-3 filaments

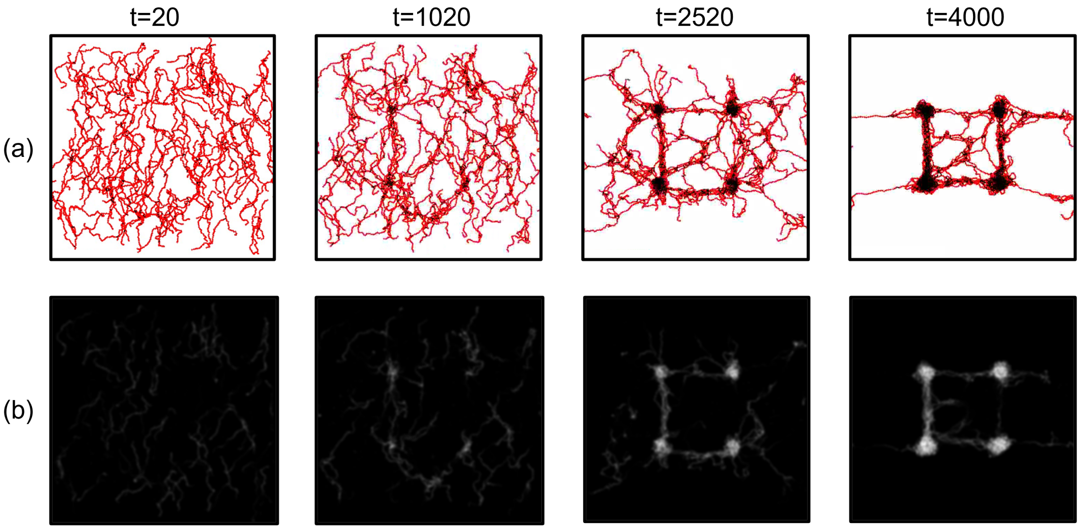

Figure 4.6: Simulation images of the actin channel sampled at 4 time frames: t = 20, 1050, 2520, 4000. (a), system configurations of the actin network. (b), pseudo micrographs of the simulation snapshots.

stretching out from each of the attractive sites and wrap around the edges of the box; again, similar to the corresponding configuration in Figure 4.2, this is due to the periodic boundary conditions of our model. For the corresponding case with microtubules (Figure 4.7) instead of actin, we see that over time, microtubules form bundles by the crosslinkers. Then, these bundles then form a network of microtubules. At each of the nucleation sites,

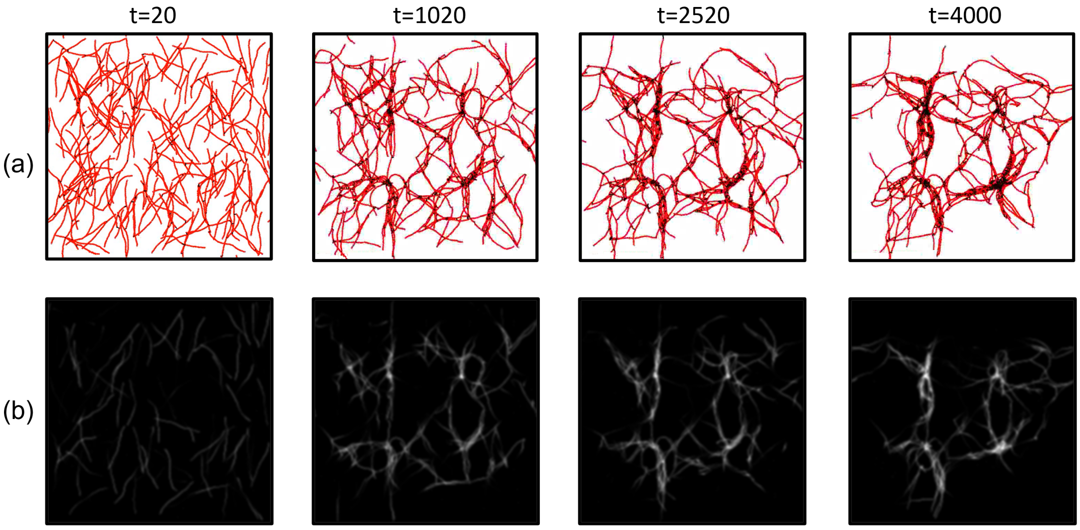

Figure 4.7: Simulation images of the microtubule channel sampled at 4 time frames: t = 20, 1050, 2520, 4000. (a), system configurations of the MT network. (b), pseudo micrographs of the simulation snapshots.

we see that the microtubule bundles become more tightly compacted but it seems that this compaction occurs in the localized regions of the nucleation site. The areas of the network that are further away from the nucleation sites do seem to experience a degree of contraction, but do not form tight bundles. Again, this is expected as the microtubules have a larger persistence length and coupling that with the static crosslinkers leads to a network that is less flexible and responsive to the nucleation sites.

Multiple nucleation site without crosslinking

We then examine systems where systems have the 4 nucleation sites but no crosslinking component. Figure 4.8 shows the time-course of a system with actin filaments with no crosslinkers. Over time, most of the actin filaments go from being in a disordered state to forming clumps at each of the nucleation sites. The ball-like structures look roughly the same size and only a few actin filaments remain free from the nucleation sites which indicates that if this simulation is run for longer times than $4000t$, all of the actin filaments would eventually be part of a clump at a nucleation site. The microtubule filaments begin in a disordered state in Figure 4.9(a) and (b), but form well-defined aster-like structures

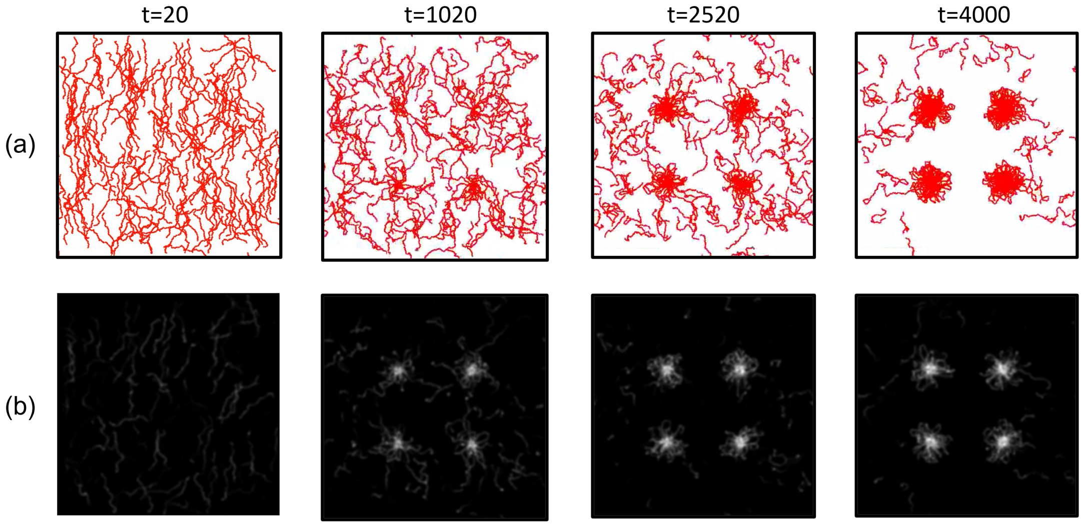

Figure 4.8: Simulation images of the actin channel with 4 nucleation sites sampled at 4 time frames: t = 20, 1050, 2520, 4000. (a), the system configurations of the actin network. (b), pseudo micrographs of the simulation snapshots.

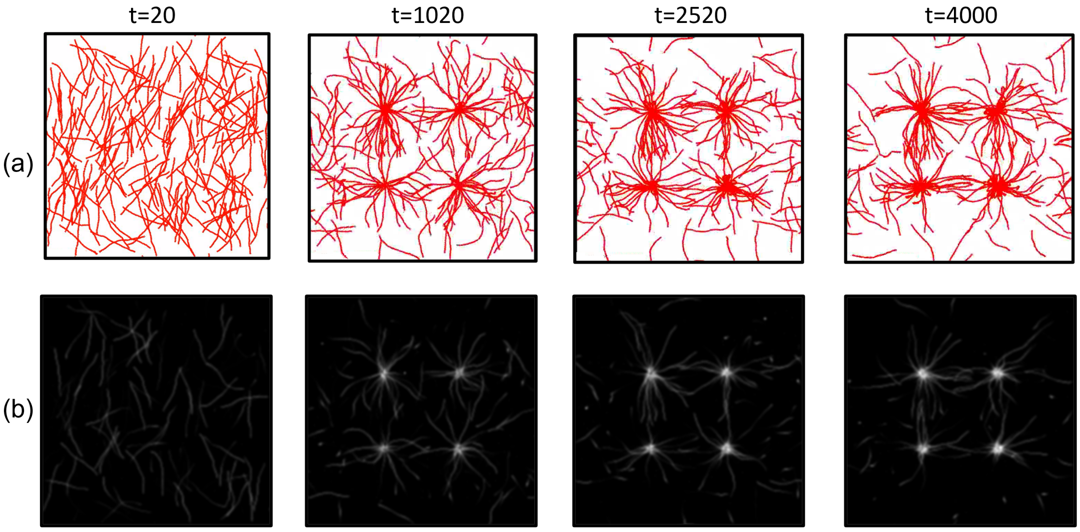

Figure 4.9: Simulation images of the MT channel with 4 nucleation sites sampled at 4 time frames: t = 20, 1050, 2520, 4000. (a), the system configurations of the MT network. (b), pseudo micrographs of the simulation snapshots.

at each of the nucleation sites. And like the actin network in Figure 4.8, a large majority of the microtubules belong to an aster which suggests that for longer simulation runs, nearly all of the filaments are likely to be part of an aster formation.

4.1.4 Conclusion

We explore the qualitative properties of 2 kinds of models: one with in-vitro cytoskeletal composites with filaments, motors, and crosslinkers. While we are able to develop a computational model based on experiments and experimentally-observed kinetics, the simulated systems did not produce the large-scale contractile behavior observed in experiments. Part of this is due to the smaller system size limiting the macroscopic properties.

A way of mitigating this was to constrain some of the model parameters and components. We constructed a second model where we limit the simulation to one set of filaments and passive crosslinkers. With this simplified model, we are able to explore the large-scale stress by implementing nucleation sites in the system space. Our system configurations show that aster formation occurs for microtubule-like filaments with no crosslinking and global contraction is present in the systems with actin filaments and static crosslinkers. With these new simulations, we can produce psuedo micrographs that mimic confocal microscopy images used for experiments.

This technique can be used to determine whether analysis of the pseudo micrograph images using digital image processing tools meant for experimental data yields results consistent with experimental findings. Metrics like particle image velicometry (PIV) can be measured from these psuedo micrographs and compared against experimental images to determine stress propagation properties. A method for measuring contraction in a network is being developed in this collaboration; measuring the pixel intensity distribution over time has been proposed and the pseudo micrographs could serve as optimal data from the simulations.

4.1.5 Future Work

The next steps for this research involve running the simplified models for larger systems sizes and longer run-times to capture a clearer picture of the system evolution. From there, we would aim to start using the psuedo micrographs and start using metrics like PIV to gain clearer insight on the stress propagation in the networks.

Another future goal involves enhancing the kinesin and myosin motors in our model, as this could help bridge the gap between the simplified model with the nucleation site and the 6-component model. For example, aster formation is common in microtubules, due to their high persistence lengths, and the high duty ratio of kinesin. Kinesin also have the ability to walk along the microtubule lengths and will eventually accumulate on the ends of the filaments [130]. If we can effectively model the processivity of these motor proteins, that would eliminate the need for the artificial nucleation sites that currently induce contraction and aster formation in the systems.

Chapter 5

Conclusion

In all 4 projects, we have created mathematical models, based in experiments and current theory, of bio and bio-inspired materials to help us understand and predict the roles of living systems and self-assembly of network-based materials. Our model studies focus on two types of substrates-colloids and biopolymers. And, the assembly drivers that produce the network-like behaviors in our various model systems are physical crosslinking proteins and depletants. We study the Langevin Dynamics of these systems and implement Lennard Jones or modified Lennard Jones potentials to model the interactions between the different components.

We first begin with a 2D model of colloidal beads undergoing dynamic network formation via bacterial proteins that are functionalized as timing circuits for the connectivity behavior. With protein crosslinker interactions effectively modeled as spring forces between attached colloids, we demonstrate that we can construct model colloidal systems that experience sustained self-assembly, oscillations between connected and disconnected states, or minimal connectivity or cluster formation.

From this, we extend our bead model to a 3D bead-spring/bead chain model to explore other systems with network-like properties with filament-like components. This includes microtubules, actin—the main components of the cytoskeleton and lambda DNA from bacterial cells. These polymers are made up of sub-units—microtubules are made up of these proteins called tubulin, actin strands consist of monomers, and DNA of course, consist of nucleotide pairs. To explore these polymer dynamics and reduce the computational expense, we're taking a coarse-grained approach by modeling these different polymers as bead chains. With this bead chain model, we can simulate many types of polymer chains or networks by tuning the bending rigidity and extensional stiffness parameters. We continue to implement similar inter-bead/strand interactions by using modified forms of the Lennard Jones potential to explicitly model mechanisms like depletion interactions and adhesive protein interactions.

In the dilute actin system undergoing depletion interactions with the help of PEG polymers, we are still able to maintain the interparticle interactions with a Lennard Jones potential and by tuning the repulsive and attractive force magnitudes, we effectively capture depletant interactions implicitly by the Lennard Jones interactions. We continue to use a piecewise Lennard Jones potential to mimic the adhesive interactions between the DPS and the DNA strands to show how these components form condensates when the number density and strength of heterotypic interactions are sufficiently large enough. For both the PEG and DPS structures, we model these as 3D colloidal spheres, analogous to the 2D colloid particles in the first and second chapters, since the radii of gyration are sufficiently small for both.

For the final research project, we examine a system with a 6-dimensional phase space to broaden our understanding of the cytoskeletal network and actin-microtubule interplay. 2 kinds of filaments, microtubules and actin, with their associated passive crosslinker proteins, and molecular motors make up the components of this model system. Similar to the KaiABC proteins in the colloid project, we also use spring forces to characterize the passive actin and microtubule crosslinkers and motors and tune the binding rates and probabilities of detachment. While we are currently enhancing the active motors, we develop another set of simulations exhibit the contractile dynamics that is present in the experiments but not in the 6-component model. This is achieved by using nucleation sites to explicitly generate the contractile and extensile behavior in the different networks.

With all of these different projects, there's been active feedback between the models and current experiments being done. Models help us understand the mechanisms and experiments help us make better models. In particular, for complex structures like the cytoskeletal composites, the biophysics is not as easily understood, and it can be difficult to obtain analytical solutions. So the simulations help us go beyond the limitations of the analytical scaling arguments and characterize their emergent collective and structural properties in areas of the phase space that can't be validated by theory. From our simulations, we gain a better understanding of the experimental design of network-like soft materials that yield robust and resilient properties. In the model space, we can explore multi-dimensional parameter spaces by tuning the concentrations of components like biopolymers, crosslinkers, motors, depletants, and biological timers like clock proteins. All our simulations are coded in C++ and run on the RIT cluster computing resources. Post-processing softwares include MATLAB, openGL, Python, and Origin.

Bibliography

[1] J. Alvarado, M. Sheinman, A. Sharma, F. C. MacKintosh, and G. H. Koenderink, *Molecular motors robustly drive active gels to a critically connected state*, Nature Physics **9**, 591–597 (2013).

[2] A. Murugan, K. Husain, M. J. Rust, C. Hepler, J. Bass, J. M. Pietsch, P. S. Swain, S. G. Jena, J. E. Toettcher, A. K. Chakraborty, et al., *Roadmap on biology in time varying environments*, Physical biology **18**, 041502 (2021).

[3] C. H. Johnson and M. J. Rust, *Circadian Rhythms in Bacteria and Microbiomes*, Springer (2021).

[4] M. Mofatteh, F. Echegaray-Iturra, A. Alamban, F. Dalla Ricca, A. Bakshi, and M. G. Aydogan, *Autonomous clocks that regulate organelle biogenesis, cytoskeletal organization, and intracellular dynamics*, Elife **10**, e72104 (2021).

[5] D. Needleman and Z. Dogic, *Active matter at the interface between materials science and cell biology*, Nature Reviews Materials **2**, 1–14 (2017).

[6] I. Buttinoni, J. Bialké, F. Kümmel, H. Löwen, C. Bechinger, and T. Speck, *Dynamical clustering and phase separation in suspensions of self-propelled colloidal particles*, Physical review letters **110**, 238301 (2013).

[7] J. Bialké, T. Speck, and H. Löwen, *Active colloidal suspensions: Clustering and phase behavior*, Journal of Non-Crystalline Solids **407**, 367–375 (2015).

[8] A. F. Taylor, M. R. Tinsley, and K. Showalter, *Insights into collective cell behaviour from populations of coupled chemical oscillators*, Physical Chemistry Chemical Physics **17**, 20047–20055 (2015).

[9] I. R. Epstein and J. A. Pojman, *An introduction to nonlinear chemical dynamics: oscillations, waves, patterns, and chaos*, Oxford university press (1998).

[10] M. J. Rust, S. S. Golden, and E. K. O'Shea, *Light-driven changes in energy metabolism directly entrain the cyanobacterial circadian oscillator*, science **331**, 220–223 (2011).

[11] G. Leech, L. Melcher, M. Chiu, M. Nugent, L. Burton, J. Kang, S. J. Kim, S. Roy, L. Farhadi, J. L. Ross, et al., *Timed material self-assembly controlled by circadian clock proteins*, arXiv preprint arXiv:2303.00779 (2023).

[12] M. Nakajima, K. Imai, H. Ito, T. Nishiwaki, Y. Murayama, H. Iwasaki, T. Oyama, and T. Kondo, *Reconstitution of circadian oscillation of cyanobacterial KaiC phosphorylation in vitro*, science **308**, 414–415 (2005).

[13] W. Zhang, X. Yu, Y. Li, Z. Su, K. D. Jandt, and G. Wei, *Protein-mimetic peptide nanofibers: Motif design, self-assembly synthesis, and sequence-specific biomedical applications*, Progress in Polymer Science **80**, 94–124 (2018).

[14] Y. Chi, Y. Zhao, Y. Hong, Y. Li, and J. Yin, *A Perspective on Miniature Soft Robotics: Actuation, Fabrication, Control, and Applications*, Advanced Intelligent Systems , 2300063 (2023).

[15] E. Roels, S. Terryn, F. Iida, A. W. Bosman, S. Norvez, F. Clemens, G. Van Assche, B. Vanderborght, and J. Brancart, *Processing of self-healing polymers for soft robotics*, Advanced Materials **34**, 2104798 (2022).

[16] A. H. Marcus and S. A. Rice, *Observations of first-order liquid-to-hexatic and*

hexatic-to-solid phase transitions in a confined colloid suspension, Physical review letters **77**, 2577 (1996).

[17] Q. Chen, S. C. Bae, and S. Granick, *Directed self-assembly of a colloidal kagome lattice*, Nature **469**, 381–384 (2011).

[18] S. Ebbens, *Active colloids: Progress and challenges towards realising autonomous applications*, Current opinion in colloid & interface science **21**, 14–23 (2016).

[19] E. Zaccarelli, I. Saika-Voivod, S. V. Buldyrev, A. J. Moreno, P. Tartaglia, and F. Sciortino, *Gel to glass transition in simulation of a valence-limited colloidal system*, The Journal of chemical physics **124**, 124908 (2006).

[20] T. P. de Souza and J. Perez-Mercader, *Entrapment in giant polymersomes of an inorganic oscillatory chemical reaction and resulting chemo-mechanical coupling*, Chemical Communications **50**, 8970–8973 (2014).

[21] S. Jamali, R. C. Armstrong, and G. H. McKinley, *Time-rate-transformation framework for targeted assembly of short-range attractive colloidal suspensions*, Materials Today Advances **5**, 100026 (2020).

[22] S. A. Mallory and A. Cacciuto, *Activity-enhanced self-assembly of a colloidal kagome lattice*, Journal of the American Chemical Society **141**, 2500–2507 (2019).

[23] Y. Wang, Y. Wang, X. Zheng, É. Ducrot, J. S. Yodh, M. Weck, and D. J. Pine, *Crystallization of DNA-coated colloids*, Nature communications **6**, 7253 (2015).

[24] F. Cui, S. Marbach, J. A. Zheng, M. Holmes-Cerfon, and D. J. Pine, *Comprehensive view of microscopic interactions between DNA-coated colloids*, Nature communications **13**, 2304 (2022).

[25] J. A. Pojman, D. C. Leard, and W. West, *Periodic polymerization of acrylonitrile in the cerium-catalyzed Belousov-Zhabotinskii reaction*, Journal of the American Chemical Society **114**, 8298–8299 (1992).

[26] R. P. Washington, W. W. West, G. P. Misra, and J. A. Pojman, *Polymerization coupled to oscillating reactions:(1) A mechanistic investigation of acrylonitrile polymerization in the Belousov- Zhabotinsky reaction in a batch reactor*, Journal of the American Chemical Society **121**, 7373–7380 (1999).

[27] B. J. Gurmessa, N. Bitten, D. T. Nguyen, O. A. Saleh, J. L. Ross, M. Das, and R. M. Robertson-Anderson, *Triggered disassembly and reassembly of actin networks induces rigidity phase transitions*, Soft matter **15**, 1335–1344 (2019).

[28] J. Berner, B. Müller, J. R. Gomez-Solano, M. Krüger, and C. Bechinger, *Oscillating modes of driven colloids in overdamped systems*, Nature communications **9**, 1–8 (2018).

[29] C. D. Abernethy, G. M. Codd, M. D. Spicer, and M. K. Taylor, *A highly stable N-heterocyclic carbene complex of trichloro-oxo-vanadium(V) displaying novel Cl—C(carbene) bonding interactions*, J. Am. Chem. Soc. **125**, 1128–1129 (2003).

[30] A. H. Chen, D. Lubkowicz, V. Yeong, R. L. Chang, and P. A. Silver, *Transplantability of a circadian clock to a noncircadian organism*, Science advances **1**, e1500358 (2015).

[31] X. Wang, S. Ramírez-Hinestrosa, J. Dobnikar, and D. Frenkel, *The Lennard-Jones potential: when (not) to use it*, Physical Chemistry Chemical Physics (2020).

[32] R. Ma and J. Berro, *Structural organization and energy storage in crosslinked actin assemblies*, PLoS computational biology **14**, e1006150 (2018).

[33] W. Wu, J. Owino, A. Al-Ostaz, and L. Cai. *Applying periodic boundary conditions in finite element analysis.* In *SIMULIA Community Conference, Providence*, pages 707–719, (2014).

[34] A. Goldbeter, *Computational approaches to cellular rhythms*, Nature **420**, 238–245 (2002).

[35] T. Ashuri, A. Armani, R. Jalilzadeh Hamidi, T. Reasnor, S. Ahmadi, and K. Iqbal, *Biomedical soft robots: current status and perspective*, Biomedical Engineering Letters **10**, 369–385 (2020).

[36] L. Melcher, E. Rennert, J. Ross, M. Rust, R. Robertson-Anderson, and M. Das, *Sustained order–disorder transitions in a model colloidal system driven by rhythmic crosslinking*, Soft Matter **18**, 2920–2927 (2022).

[37] G. Foffano, N. Levernier, and M. Lenz, *The dynamics of filament assembly define cytoskeletal network morphology*, Nature communications **7**, 1–8 (2016).

[38] G. M. K. K. B. CP and L. J. W. DA, *Chapter 19: Mechanical response of cytoskeletal networks*, Methods Cell Biol **89**, 487519 (2008).

[39] G. Cooper, *The Cell: A Molecular Approach 2nd edition Boston University*, Sunderland (MA): Sinauer Associates.[Google Scholar] (2000).

[40] P. Matsudalra, *Modular organization of actin crosslinking proteins*, Trends in biochemical sciences **16**, 87–92 (1991).

[41] S. Nagy, B. L. Ricca, M. F. Norstrom, D. S. Courson, C. M. Brawley, P. A. Smithback, and R. S. Rock, *A myosin motor that selects bundled actin for motility*, Proceedings of the National Academy of Sciences **105**, 9616–9620 (2008).

[42] Y. Tseng, T. P. Kole, J. S. Lee, E. Fedorov, S. C. Almo, B. W. Schafer, and D. Wirtz, *How actin crosslinking and bundling proteins cooperate to generate an enhanced cell mechanical response*, Biochemical and biophysical research communications **334**, 183–192 (2005).

[43] N. Elkhatib, M. B. Neu, C. Zensen, K. M. Schmoller, D. Louvard, A. R. Bausch, T. Betz, and D. M. Vignjevic, *Fascin plays a role in stress fiber organization and focal adhesion disassembly*, Current Biology **24**, 1492–1499 (2014).

[44] D. S. Courson and R. S. Rock, *Actin cross-link assembly and disassembly mechanics for α-actinin and fascin*, Journal of Biological Chemistry **285**, 26350–26357 (2010).

[45] T. P. Stossel, J. Condeelis, L. Cooley, J. H. Hartwig, A. Noegel, M. Schleicher, and S. S. Shapiro, *Filamins as integrators of cell mechanics and signalling*, Nature reviews Molecular cell biology **2**, 138–145 (2001).

[46] K. Schmoller, O. Lieleg, and A. Bausch, *Structural and viscoelastic properties of actin/filamin networks: cross-linked versus bundled networks*, Biophysical journal **97**, 83–89 (2009).

[47] J. Clarke, F. Cavanna, A. D. Crowell, J. R. Houser, K. Graham, A. Green, L. Melcher, J. C. Stachowiak, T. M. Truskett, D. J. Milliron, A. M. Rosales, M. Das, and J. Alvarado, *Depletion-Driven Morphological Control of Bundled Actin Networks*, arXiv preprint arXiv:2205.01864 (2022).

[48] T. Schilling, S. Jungblut, and M. A. Miller, *Depletion-induced percolation in networks of nanorods*, Physical review letters **98**, 108303 (2007).

[49] C. Kim, Y. Liu, A. Kühnle, S. Hess, S. Viereck, T. Danner, L. Mahadevan, and D. A. Weitz, *Gravitational stability of suspensions of attractive colloidal particles*, Physical review letters **99**, 028303 (2007).

[50] R. Tharmann, M. Claessens, and A. Bausch, *Micro-and macrorheological properties of actin networks effectively cross-linked by depletion forces*, Biophysical journal **90**, 2622–2627 (2006).

[51] M. Hosek and J. Tang, *Polymer-induced bundling of F actin and the depletion force*, Physical Review E **69**, 051907 (2004).

[52] A. Lau, A. Prasad, and Z. Dogic, *Condensation of isolated semi-flexible filaments driven by depletion interactions*, EPL (Europhysics Letters) **87**, 48006 (2009).

[53] H. N. Lekkerkerker, R. Tuinier, H. N. Lekkerkerker, and R. Tuinier, *Phase Transitions of Hard Spheres Plus Colloids*, Colloids and the Depletion Interaction , 177–195 (2011).

[54] C. Zhang, P. G. Shao, J. A. van Kan, and J. R. van der Maarel, *Macromolecular crowding induced elongation and compaction of single DNA molecules confined in a nanochannel*, Proceedings of the National Academy of Sciences **106**, 16651–16656 (2009).

[55] T. Sanchez, D. T. Chen, S. J. DeCamp, M. Heymann, and Z. Dogic, *Spontaneous motion in hierarchically assembled active matter*, Nature **491**, 431–434 (2012).

[56] G. E. Neurohr and A. Amon, *Relevance and regulation of cell density*, Trends in cell biology **30**, 213–225 (2020).

[57] S. Asakura and F. Oosawa, *Interaction between particles suspended in solutions of macromolecules*, Journal of polymer science **33**, 183–192 (1958).

[58] A. Z. Akcasu and C. C. Han, *Molecular weight and temperature dependence of polymer dimensions in solution*, Macromolecules **12**, 276–280 (1979).

[59] M. Dijkstra, J. M. Brader, and R. Evans, *Phase behaviour and structure of model colloid-polymer mixtures*, Journal of Physics: Condensed Matter **11**, 10079 (1999).

[60] M. Wahab, P. Schiller, R. Schmidt, and H.-J. Mogel, *Monte Carlo study of the self-assembly of achiral bolaform amphiphiles into helical nanofibers*, Langmuir **26**, 2979–2982 (2010).

[61] K. Guo, J. Shillcock, and R. Lipowsky, *Self-assembly of actin monomers into long filaments: Brownian dynamics simulations*, The Journal of chemical physics **131**, 07B602 (2009).

[62] R. J. Ellis, *Macromolecular crowding: obvious but underappreciated*, Trends in biochemical sciences **26**, 597–604 (2001).

[63] Y. Shin and C. P. Brangwynne, *Liquid phase condensation in cell physiology and disease*, Science **357**, eaaf4382 (2017).

[64] B. Alberts, *Molecular biology of the cell*, Garland science (2017).

[65] C. F. Fox, *The structure of cell membranes*, Scientific American **226**, 30–39 (1972).

[66] T. Svitkina, *The actin cytoskeleton and actin-based motility*, Cold Spring Harbor perspectives in biology **10**, a018267 (2018).

[67] H. Jing, Q. Bai, Y. Lin, H. Chang, D. Yin, and D. Liang, *Fission and Internal Fusion of Protocell with Membraneless "Organelles" Formed by Liquid–Liquid Phase Separation*, Langmuir **36**, 8017–8026 (2020).

[68] X. Jin, J.-E. Lee, C. Schaefer, X. Luo, A. J. Wollman, A. L. Payne-Dwyer, T. Tian, X. Zhang, X. Chen, Y. Li, et al., *Membraneless organelles formed by liquid-liquid phase separation increase bacterial fitness*, Science Advances **7**, eabh2929 (2021).

[69] H. Zhang, X. Ji, P. Li, C. Liu, J. Lou, Z. Wang, W. Wen, Y. Xiao, M. Zhang, and X. Zhu, *Liquid-liquid phase separation in biology: mechanisms, physiological functions and human diseases*, Science China Life Sciences **63**, 953–985 (2020).

[70] E. A. Abbondanzieri and A. S. Meyer, *More than just a phase: the search for membraneless organelles in the bacterial cytoplasm*, Current genetics **65**, 691–694 (2019).

[71] J. Valkenburg and C. Woldringh, *Phase separation between nucleoid and cytoplasm in Escherichia coli as defined by immersive refractometry*, Journal of bacteriology **160**, 1151–1157 (1984).

[72] E. Gomes and J. Shorter, *The molecular language of membraneless organelles*, Journal of Biological Chemistry **294**, 7115–7127 (2019).

[73] V. O. Karas, I. Westerlaken, and A. S. Meyer, *The DNA-binding protein from starved cells (Dps) utilizes dual functions to defend cells against multiple stresses*, Journal of bacteriology **197**, 3206–3215 (2015).

[74] E. V. Dubrovin, L. A. Dadinova, M. V. Petoukhov, E. Y. Soshinskaya, A. A. Mozhaev, D. V. Klinov, T. E. Schäffer, E. V. Shtykova, and O. V. Batishchev, *Spatial organization of Dps and DNA–Dps complexes*, Journal of Molecular Biology **433**, 166930 (2021).

[75] R. L. Ohniwa, K. Morikawa, J. Kim, T. Ohta, A. Ishihama, C. Wada, and K. Takeyasu, *Dynamic state of DNA topology is essential for genome condensation in bacteria*, The EMBO journal **25**, 5591–5602 (2006).

[76] K. Zeth, *Dps biomineralizing proteins: multifunctional architects of nature*, Biochemical Journal **445**, 297–311 (2012).

[77] E. Chiancone and P. Ceci, *The multifaceted capacity of Dps proteins to combat bacterial stress conditions: detoxification of iron and hydrogen peroxide and DNA binding*, Biochimica et Biophysica Acta (BBA)-General Subjects **1800**, 798–805 (2010).

[78] R. Janissen, M. M. Arens, N. N. Vtyurina, Z. Rivai, N. D. Sunday, B. Eslami-Mossallam, A. A. Gritsenko, L. Laan, D. de Ridder, I. Artsimovitch, et al., *Global DNA compaction in stationary-phase bacteria does not affect transcription*, Cell **174**, 1188–1199 (2018).

[79] E. Cabiscol Català, J. Tamarit Sumalla, and J. Ros Salvador, *Oxidative stress in bacteria and protein damage by reactive oxygen species*, International Microbiology, 2000, vol. 3, núm. 1, p. 3-8 (2000).

[80] M. Almiron, A. J. Link, D. Furlong, and R. Kolter, *A novel DNA-binding protein*

with regulatory and protective roles in starved Escherichia coli., Genes & development **6**, 2646–2654 (1992).

[81] L. N. Calhoun and Y. M. Kwon, *The ferritin-like protein Dps protects Salmonella enterica serotype Enteritidis from the Fenton-mediated killing mechanism of bactericidal antibiotics*, International journal of antimicrobial agents **37**, 261–265 (2011).

[82] M. El Khoury, J. Swain, G. Sautrey, L. Zimmermann, P. Van Der Smissen, J.-L. Décout, and M.-P. Mingeot-Leclercq, *Targeting bacterial cardiolipin enriched microdomains: an antimicrobial strategy used by amphiphilic aminoglycoside antibiotics*, Scientific reports **7**, 1–12 (2017).

[83] N. N. Vtyurina, D. Dulin, M. W. Docter, A. S. Meyer, N. H. Dekker, and E. A. Abbondanzieri, *Hysteresis in DNA compaction by Dps is described by an Ising model*, Proceedings of the National Academy of Sciences **113**, 4982–4987 (2016).

[84] A. Moiseenko, N. Loiko, K. Tereshkina, Y. Danilova, V. Kovalenko, O. Chertkov, A. V. Feofanov, Y. F. Krupyanskii, and O. S. Sokolova, *Projection structures reveal the position of the DNA within DNA-Dps Co-crystals*, Biochemical and Biophysical Research Communications **517**, 463–469 (2019).

[85] G. Le Treut, F. Képès, and H. Orland, *Phase behavior of DNA in the presence of DNA-binding proteins*, Biophysical Journal **110**, 51–62 (2016).

[86] M. B. Elowitz, M. G. Surette, P.-E. Wolf, J. B. Stock, and S. Leibler, *Protein mobility in the cytoplasm of Escherichia coli*, Journal of bacteriology **181**, 197–203 (1999).

[87] J. V. Small, K. Rottner, and I. Kaverina, *Functional design in the actin cytoskeleton*, Current opinion in cell biology **11**, 54–60 (1999).

[88] A. F. Pegoraro, P. Janmey, and D. A. Weitz, *Mechanical properties of the cytoskeleton and cells*, Cold Spring Harbor perspectives in biology **9**, a022038 (2017).

[89] K. Wang and D. Sun, *Influence of semiflexible structural features of actin cytoskeleton on cell stiffness based on actin microstructural modeling*, Journal of biomechanics **45**, 1900–1908 (2012).

[90] Q. Wen and P. A. Janmey, *Polymer physics of the cytoskeleton*, Current Opinion in Solid State and Materials Science **15**, 177–182 (2011).

[91] I. Rayment, *Kinesin and myosin: molecular motors with similar engines*, Structure **4**, 501–504 (1996).

[92] C. A. Wilson, M. A. Tsuchida, G. M. Allen, E. L. Barnhart, K. T. Applegate, P. T. Yam, L. Ji, K. Keren, G. Danuser, and J. A. Theriot, *Myosin II contributes to cell-scale actin network treadmilling through network disassembly*, Nature **465**, 373–377 (2010).

[93] K. E. Kasza and J. A. Zallen, *Dynamics and regulation of contractile actin–myosin networks in morphogenesis*, Current opinion in cell biology **23**, 30–38 (2011).

[94] I. Ali and W.-C. Yang, *The functions of kinesin and kinesin-related proteins in eukaryotes*, Cell Adhesion & Migration **14**, 139–152 (2020).

[95] C. E. Walczak, S. Gayek, and R. Ohi, *Microtubule-depolymerizing kinesins*, Annual review of cell and developmental biology **29**, 417–441 (2013).

[96] J. C. Meiring, B. I. Shneyer, and A. Akhmanova, *Generation and regulation of microtubule network asymmetry to drive cell polarity*, Current Opinion in Cell Biology **62**, 86–95 (2020).

[97] G. Apodaca, *Endocytic traffic in polarized epithelial cells: role of the actin and microtubule cytoskeleton*, Traffic **2**, 149–159 (2001).

[98] J.-D. Huang, S. T. Brady, B. W. Richards, D. Stenoien, J. H. Resau, N. G. Copeland, and N. A. Jenkins, *Direct interaction of microtubule-and actin-based transport motors*, Nature **397**, 267–270 (1999).

[99] G. H. Koenderink and E. K. Paluch, *Architecture shapes contractility in actomyosin networks*, Current opinion in cell biology **50**, 79–85 (2018).

[100] S. Wang and P. G. Wolynes, *Active contractility in actomyosin networks*, Proceedings of the National Academy of Sciences **109**, 6446–6451 (2012).

[101] M. Malik-Garbi, N. Ierushalmi, S. Jansen, E. Abu-Shah, B. L. Goode, A. Mogilner, and K. Keren, *Scaling behaviour in steady-state contracting actomyosin networks*, Nature physics **15**, 509–516 (2019).

[102] S. L. Freedman, G. M. Hocky, S. Banerjee, and A. R. Dinner, *Nonequilibrium phase diagrams for actomyosin networks*, Soft matter **14**, 7740–7747 (2018).

[103] J. Pringle, A. Muthukumar, A. Tan, L. Crankshaw, L. Conway, and J. L. Ross, *Microtubule organization by kinesin motors and microtubule crosslinking protein MAP65*, Journal of Physics: Condensed Matter **25**, 374103 (2013).

[104] T. S. Randall, Y. Y. Yip, D. J. Wallock-Richards, K. Pfisterer, A. Sanger, W. Ficek, R. A. Steiner, A. J. Beavil, M. Parsons, and M. P. Dodding, *A small-molecule activator of kinesin-1 drives remodeling of the microtubule network*, Proceedings of the National Academy of Sciences **114**, 13738–13743 (2017).

[105] A. Enomoto, M. J. Moore, T. Suda, and K. Oiwa, *Design of self-organizing microtubule networks for molecular communication*, Nano Communication Networks **2**, 16–24 (2011).

[106] B. L. Goode, D. G. Drubin, and G. Barnes, *Functional cooperation between the microtubule and actin cytoskeletons*, Current opinion in cell biology **12**, 63–71 (2000).

[107] A. Colin, P. Singaravelu, M. Théry, L. Blanchoin, and Z. Gueroui, *Actin-network architecture regulates microtubule dynamics*, Current Biology **28**, 2647–2656 (2018).

[108] M. L. Pimm and J. L. Henty-Ridilla, *New twists in actin–microtubule interactions*, Molecular Biology of the Cell **32**, 211–217 (2021).

[109] R. M. Robertson-Anderson, *Active dynamics and tunable mechanics of actin-microtubule composites*, Biophysical Journal **121**, 143a (2022).

[110] M. Sasanpour, D. H. Achiriloaie, G. Lee, G. Leech, C. Currie, K. A. Lindsay, J. L. Ross, R. J. McGorty, and R. M. Robertson-Anderson, *Reconstituting and Characterizing Actin-Microtubule Composites with Tunable Motor-Driven Dynamics and Mechanics*, JoVE (Journal of Visualized Experiments) , e64228 (2022).

[111] E. Frey, *Physics in cell biology: on the physics of biopolymers and molecular motors*, ChemPhysChem **3**, 270–275 (2002).

[112] T. Vignaud, L. Blanchoin, and M. Théry, *Directed cytoskeleton self-organization*, Trends in cell biology **22**, 671–682 (2012).

[113] D. Trivedi, C. D. Rahn, W. M. Kier, and I. D. Walker, *Soft robotics: Biological inspiration, state of the art, and future research*, Applied bionics and biomechanics **5**, 99–117 (2008).

[114] Z. Dai, Y. Wang, L. Liu, X. Liu, P. Tan, Z. Xu, J. Kuang, Q. Liu, J. Lou, and Z. Zhang, *Hierarchical Graphene-Based Films with Dynamic Self-Stiffening for Biomimetic Artificial Muscle*, Advanced Functional Materials **26**, 7003–7010 (2016).

[115] T. Patino, R. Mestre, and S. Sanchez, *Miniaturized soft bio-hybrid robotics: a step forward into healthcare applications*, Lab on a Chip **16**, 3626–3630 (2016).

[116] B. Guo and W. H. Guilford, *Mechanics of actomyosin bonds in different nucleotide states are tuned to muscle contraction*, Proceedings of the National Academy of Sciences **103**, 9844–9849 (2006).

[117] J. Berezney, B. L. Goode, S. Fraden, and Z. Dogic, *Extensile to contractile transition in active microtubule–actin composites generates layered asters with programmable lifetimes*, Proceedings of the National Academy of Sciences **119**, e2115895119 (2022).

[118] T. Thoresen, M. Lenz, and M. L. Gardel, *Reconstitution of contractile actomyosin bundles*, Biophysical journal **100**, 2698–2705 (2011).

[119] F. C. MacKintosh and A. J. Levine, *Nonequilibrium mechanics and dynamics of motor-activated gels*, Physical review letters **100**, 018104 (2008).

[120] R. Subramanian and J. Gelles, *Two distinct modes of processive kinesin movement in mixtures of ATP and AMP-PNP*, The Journal of general physiology **130**, 445–455 (2007).

[121] A. Nayak, T. Wang, P. Franz, W. Steffen, I. Chizhov, G. Tsiavaliaris, and M. Amrute-Nayak, *Single-molecule analysis reveals that regulatory light chains fine-tune skeletal myosin II function*, Journal of Biological Chemistry **295**, 7046–7059 (2020).

[122] J. Y. Sheung, D. H. Achiriloaie, C. Currie, K. Peddireddy, A. Xie, J. Simon-Parker, G. Lee, M. J. Rust, M. Das, J. L. Ross, et al., *Motor-driven restructuring of cytoskeleton composites leads to tunable time-varying elasticity*, ACS macro letters **10**, 1151–1158 (2021).

[123] R. A. Banks, V. Galstyan, H. J. Lee, S. Hirokawa, A. Ierokomos, T. D. Ross, Z. Bryant, M. Thomson, and R. Phillips, *Motor processivity and speed determine structure and dynamics of microtubule-motor assemblies*, Elife **12**, e79402 (2023).

[124] K. Kruse and F. Jülicher, *Actively contracting bundles of polar filaments*, Physical review letters **85**, 1778 (2000).

[125] V. Nasirimarekani, S. Subramani, S. Herzog, A. Vilfan, and I. Guido, *Active Bending of Disordered Microtubule Bundles by Kinesin Motors*, ACS omega **7**, 43820–43828 (2022).

[126] B. Najma, A. Baskaran, P. J. Foster, and G. Duclos, *Microscopic interactions control*

a structural transition in active mixtures of microtubules and molecular motors, bioRxiv , 2023–01 (2023).

[127] H. H. Mattingly, M. K. Transtrum, M. C. Abbott, and B. B. Machta, *Maximizing the information learned from finite data selects a simple model*, Proceedings of the National Academy of Sciences **115**, 1760–1765 (2018).

[128] D. Saintillan, M. J. Shelley, and A. Zidovska, *Extensile motor activity drives coherent motions in a model of interphase chromatin*, Proceedings of the National Academy of Sciences **115**, 11442–11447 (2018).

[129] P. Ronceray, C. P. Broedersz, and M. Lenz, *Fiber networks amplify active stress*, Proceedings of the national academy of sciences **113**, 2827–2832 (2016).

[130] J. O. Andreasson, B. Milic, G.-Y. Chen, N. R. Guydosh, W. O. Hancock, and S. M. Block, *Examining kinesin processivity within a general gating framework*, Elife **4**, e07403 (2015).

Publications

“Depletion-Driven Morphological Control of Bundled Actin Networks", James Clarke, Francis Cavanna, Anne D. Crowell, Justin R. Houser, Kristin Graham, Allison Green, **Lauren Melcher**, Jeanne C. Stachowiak, Thomas M. Truskett, Delia J. Milliron, Adrianne M. Rosales, Moumita Das, and José Alvarado, *Soft Matter*, in preparation.

“Sustained order-disorder transitions in a model colloidal system driven by rhythmic crosslinking", **Lauren Melcher**, Elisabeth Rennert, Jennifer L. Ross, Michael Rust, Rae M. Robertson-Anderson, Moumita Das, *Soft Matter*,Volume 18, Issue 15, pp 2920-2927, Mar. 16 2022.

Conference Talks

“Sustained order-disorder transitions in a model colloidal network crosslinked via oscillator proteins", **Lauren Melcher**, Elisabeth Rennert, Jennifer L. Ross, Michael Rust, Rae M. Robertson-Anderson, Moumita Das, *American Physics Society*: March Meeting, March 2022.

“A computational investigation of a colloidal network that can dynamically stiffen when crosslinked by KaiABC proteins", **Lauren Melcher**, Elisabeth Rennert, Jennifer L. Ross, Michael Rust, Rae M. Robertson-Anderson, Moumita Das, *Multiscale Mechanochemistry & Mechanobiology*: MechanoChemBio2021, August 2021.

“Modelling a colloidal network that can dynamically stiffen via bacterial circadian proteins, KaiABC", **Lauren Melcher**, Elisabeth Rennert, Jennifer L. Ross, Michael Rust, Rae M. Robertson-Anderson, Moumita Das, *American Physics Society*: March Meeting, March 2021.

“Autonomous oscillations in the structure-function properties of dynamically regulated active colloidal networks", **Lauren Melcher**, Elisabeth Rennert, Jennifer L. Ross, Michael Rust, Rae M. Robertson-Anderson, Moumita Das, *American Physics Society*: Virtual March Meeting, March 2021.

“Computational study of autonomous mechanical oscillations in a colloidal network crosslinked via clock proteins", **Lauren Melcher**, Elisabeth Rennert, Jennifer L. Ross, Michael Rust, Rae M. Robertson-Anderson, Moumita Das, *American Physics Society*: Virtual March Meeting, March 2020.